UNIVERSITÄT BONN
Physikalisches Institut

Two-Particle Correlations and Density Fluctuations in Proton-Antiproton Interactions at c.m. Energies from 200 to 900 GeV

Inaugural-Dissertation
zur
Erlangung des Doktorgrades
der
Hohen Mathematisch-Naturwissenschaftlichen Fakultät
der Rheinischen Friedrich-Wilhelms-Universität
zu Bonn

vorgelegt von
Brigitte Eckart

Post address:
Nussallee 12
D-5300 Bonn 1
W-Germany

BONN-IR-88-21
Bonn University
May 1988
ISSN 0172-8741

UNIVERSITÄT BONN
Physikalisches Institut

Two-Particle Correlations and Density Fluctuations in Proton-Antiproton Interactions at c.m. Energies from 200 to 900 GeV

Inaugural-Dissertation
zur
Erlangung des Doktorgrades
der
Hohen Mathematisch-Naturwissenschaftlichen Fakultät
der Rheinischen Friedrich-Wilhelms-Universität
zu Bonn

vorgelegt von
Brigitte Eckart

Post address:
Nussallee 12
D-5300 Bonn 1
W-Germany

BONN-IR-88-21
Bonn University
May 1988
ISSN 0172-8741

Angefertigt mit Genehmigung der
Mathematisch-Naturwissenschaftlichen Fakultät
der Universität Bonn

Referent:	Prof. Dr. G. Knop
Koreferent:	Prof. Dr. K. Heinloth

Contents

Introduction

The dynamics of strong interactions between hadrons have, over the last two decades, been studied in a wide range of collision energy. Each new energy domain has revealed unexpected discoveries and brought new insights into the features of hadronic interactions. The construction of the CERN $p\bar{p}$-Collider, where protons and antiprotons with a c.m. energy between 200 GeV and 900 GeV interact, has increased the previously available energy of the CERN ISR by about one order of magnitude.

Two large experiments, UA1 [UA1 78] and UA2 [UA2 78], installed at this facility are primarily dedicated to the discovery of the intermediate vector bosons predicted by the Salam-Weinberg theory of electro-weak interactions [RUB 84]. They were also equipped to study special high transverse momentum features of $p\bar{p}$-collisions, such as jet phenomena, new flavors, etc. Among the several smaller experiments, UA4 and UA5 have the purpose to study the general features of $p\bar{p}$-interactions. UA4 aims to extract the total cross section and measure elastic scattering and diffraction dissociation [UA4 78].

The UA5 experiment [UA5 78] is designed to give a fast overview on the main features of low transverse momentum $p\bar{p}$-interactions and to look for indications of exotic phenomena predicted in cosmic ray experiments. It is therefore conceived as a simple visual detector consisting of two large streamer chambers. One of its main advantages is the nearly 4π overall geometrical acceptance and good tracking resolution which allows a reliable measurement of charged particle multiplicities and production angles. The visual recording of the events aids the recognition of special event features (e.g. strange particle decays) and allows great flexibility in the search for exotic and unexpected event configurations.

Various results pertaining to the properties of low transverse momentum collisions at c.m. energies from 200 GeV to 900 GeV have been published by the UA5-Collaboration[1], such as :

- The properties and scaling behavior of the charged particle multiplicity distribution and its moments, for the full phase space [UA5 81c,UA5 83a,UA5 84,UA5 85d,UA5 86a] and for limited regions [UA5 85c].
- The pseudorapidity[2] distribution and its scaling behavior [UA5 81b,UA5 86d].
- Strange particle production [UA5 82c,UA5 85a,UA5 85b,UA5 87d,UA5 88a].

[1] Data were also taken with the same detector at the CERN ISR at 53 GeV, the results are published in [UA582b].

[2] Pseudorapidity is related to rapidity and defined as $\eta = -\log\tan\Theta/2$, where Θ is the c.m. polar production angle.

- Photon production [UA5 82d,UA5 88b].
- Overall cross-sections for particle production and the study of diffractive processes [UA5 86b,UA5 86e].
- Multiplicity correlations between forward and backward hemispheres [UA5 83b,UA5 87b].

These have provided insights into the production processes at Collider energies. In particular, the study of correlations among the final state particles produced in the same event gives information on the dynamics of the underlying production mechanism. Studies of this type try to answer the following question : If one observes a particle in a given region of phase space, where does one expect other particles in the same event to be found. Correlation studies necessitate a large number of particles produced and a sufficiently broad rapidity range available for study. They have been undertaken from c.m. energies of 5 GeV [KO 72] on, but only since the operation of the CERN ISR [BEL 72,DIB 73] and the proton synchrotron at FNAL [COH 73] has abundant evidence for correlations among final state particles become available. Since then correlations have also been studied in e^+e^--interactions [KOC 82,DER 86], and even in light ion collisions [BEL 84].

There are various possibilities for studying particle correlations, for example :

- Multiplicity correlations between different pseudorapidity regions; these are sensitive to long-range phenomena.
- Rapidity correlations between two or more particles that measure short-range effects.
- Correlations in rapidity <u>and</u> azimuth give information on resonance production.
- Correlations between different charge states, flavor and baryon number.
- Bose-Einstein correlations between pions.

Only multiplicity and rapidity correlations, though, can be observed in this experiment. Here the analysis of short-range two-body rapidity correlations will be described, complementing the already published results on multiplicity correlations [UA5 82d,UA5 83b,UA5 87b]. In particular, the question whether the interpretation of lower energy data in terms of a "cluster" model is still valid at Collider energies will be discussed.

Another aim of the UA5-experiment was the search for exotic phenomena. Prompted by unusual event structures seen in cosmic ray experiments [LAT 80,CHI 82], a search was made for similar events [UA5 82d,UA5 86c]. In particular, the observation of events with extremely large local particle densities in rapidity space [ALE 62,BUR 83] has suggested a study of fluctuations in the pseudorapidity distribution, in order to search for similar events. Theoretical calculations imply a possible onset of a phase transition in matter at very high energies ("quark gluon plasma"), where one signature could be large fluctuations in the angular distribution of an event. The analysis described here will try to answer the question, to what extent the observed rapidity fluctuations in the UA5 data can be expected from conventional low transverse momentum processes, and to what degree they are connected with particle correlations.

The subsequent chapters are organized as follows; chapter II describes the components of the UA5-detector and the experimental setup. Next, chapter III outlines the data taking and primary analysis techniques to clean the data sample. The methods to calculate and correct charged particle densities are given in chapter IV. Here the distributions needed for the discussion of rapidity correlations are given. The following chapter gives results of the analysis of short-range rapidity correlations and interprets them in the light of certain theoretical models. Chapter VI will treat local fluctuations in pseudorapidity density with detailed comparisons with the UA5-Monte Carlo program. Finally, chapter VII briefly summarizes the conclusions.

The UA5 Experiment

II.1 The $p\bar{p}$-Collider

The idea to convert the CERN SPS fixed target machine into a proton-antiproton Collider was first suggested by C.Rubbia in 1976 [RUB 76]. The major problem of achieving a sufficiently intense $\bar{p}$ beam was solved by using the method of stochastic cooling first proposed by S.van der Meer [MEE 72].

Antiprotons are produced by collisions of protons on a target. Therefore, they have a wide spread of longitudinal momenta and angles, i.e. their longitudinal and transverse phase space density is very low. Rather than filtering out particles with too large a deviation from the nominal momentum values, thus further decreasing the number of available antiprotons, one compresses the phase space volume by stochastic cooling [MOE 80].

This method acts on the statistical fluctuations in a small region of the beam phase space. For transverse (betatron) cooling the average transverse position of the beam is detected by a pickup. This signal is amplified and fed into a transverse kicker-magnet which then applies the correct pulse to the same set of particles measured. Longitudinal cooling is achieved by the "filter method" : Information on a particle's momentum is obtained through its relationship with its revolution frequency. A filter introduced in the feedback chain causes a longitudinal kicker magnet to accelerate particles with momentum less than the nominal momentum and to decelerate faster ones.

Because this cooling method averages over particles picked up in a small sample, only a small amount of cooling can be achieved for each observation. It is, therefore, only applicable to circulating beams which are cooled for a long time interval.

A layout of the CERN $p\bar{p}$-project [HOF 81] is shown in fig. II.1. Every 2.4 seconds a high intensity (10^{13} protons) pulse of 26 GeV/c protons is ejected from the PS and focussed on a tungsten target. Here they produce up to 2.5×10^7 antiprotons with a maximum yield at 3.5 GeV/c. These are injected into the AA (Antiproton Accumulator) where the cooling and accumulation of the antiprotons takes place [KOZ 79].

The momentum spread of each injected pulse is reduced rapidly to 0.17% by a precooling system using the filter method. The precooled pulse is then decelerated and deposited on top of the antiproton stack. The stack itself is cooled continuously both longitudinally and transversely. After 24 hours of stacking and cooling about 10^{11} antiprotons have been accumulated. Up to 6 bunches of 10^{10} antiprotons are then collected and ejected to the PS, there they are accelerated to 26 GeV/c and transferred to the SPS. Here, proton bunches have already been stored as "coasting protons" and are now accelerated together with the

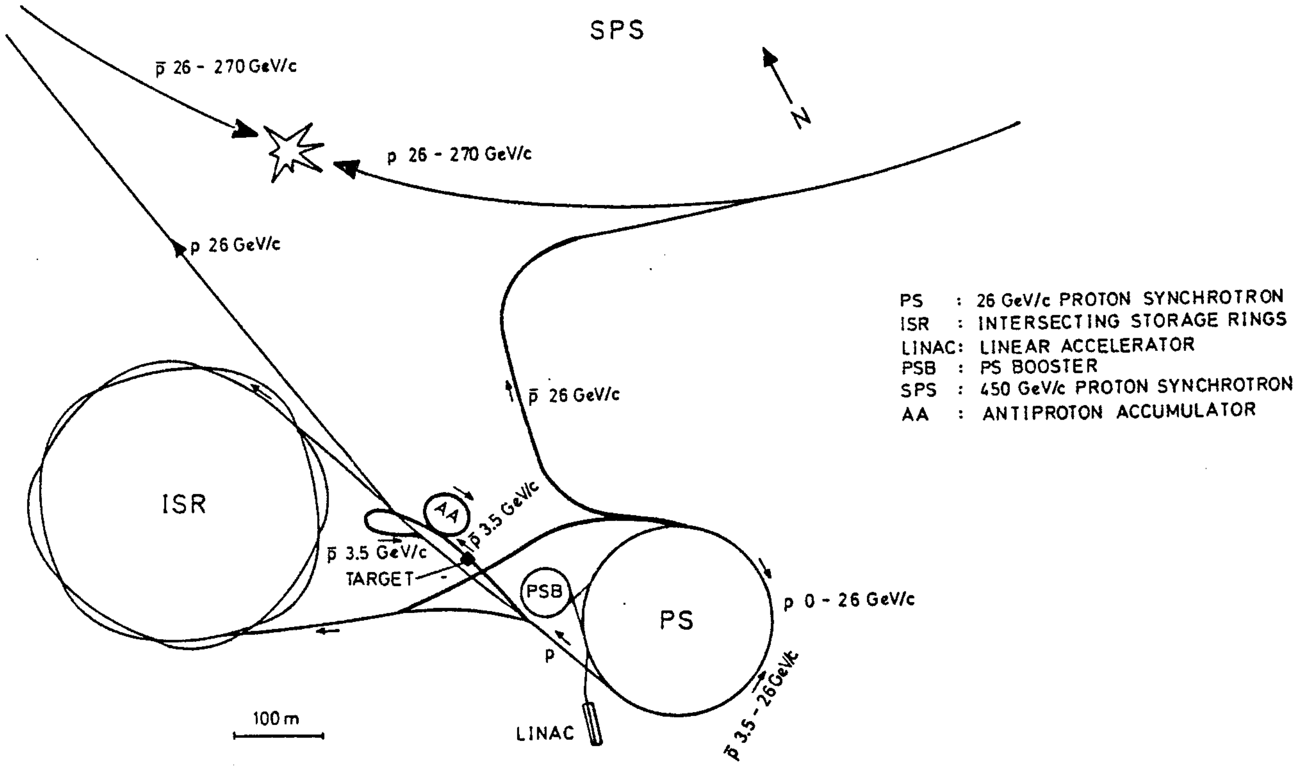

Figure II.1: Layout of the CERN pp̄-project.

antiprotons.

The maximum beam momentum to be reached is restricted by the level of power dissipation, that can be tolerated by the ring magnets, to about 273 GeV/c (equivalent to $\sqrt{s} = 546$ GeV)[1]. In 1982 a scheme ("Pulsed Collider") was proposed to reach even higher energies [RUS 82]. The energy of the stored beams should be cycled between 450 GeV and 100 GeV, such that the average power dissipation is reduced to an acceptable level (provided the time constant for heating of the magnets is long compared to the cycle length). The cycle used is illustrated in fig. II.2, consisting of a 4 second flat top at 450 GeV beam energy and a total length of 21.6 s. Details of the Pulsed Collider performance can be found in [LAU 85,RUS 85].

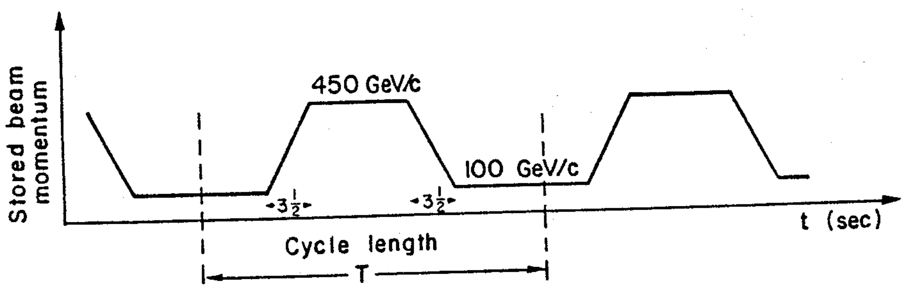

Figure II.2: Cyclic variation of the beam momentum.

[1] In 1984 a top beam energy of 315 GeV was reached after improvements in the magnet cooling system.

II.2 The UA5 Detector

II.2.1 Introduction

The UA5 detector [UA5 81a] is designed to give a fast survey of the main features of $p\bar{p}$-interactions at $\sqrt{s} = 546$ GeV and to investigate unexpected or exotic topologies. Therefore, the detector has to meet the following requirements :

- Because many hours are needed to acquire a sufficiently intense beam of antiprotons only a very limited access to the detector is available during run periods. Good reliability of the system was therefore a basic requirement.
- To record an event as complete as possible the geometrical acceptance should cover essentially the whole solid angle.
- In order to cope with very high multiplicities of tracks (up to 100 primary and 100 secondary tracks) the two-track resolution has to be excellent.
- The detection of neutral particles as well as strange particles should be possible.

As a detector best suited for these demands a large streamer chamber system (fig. II.3) was chosen, which possesses a nearly 100% track detection efficiency and a good two-

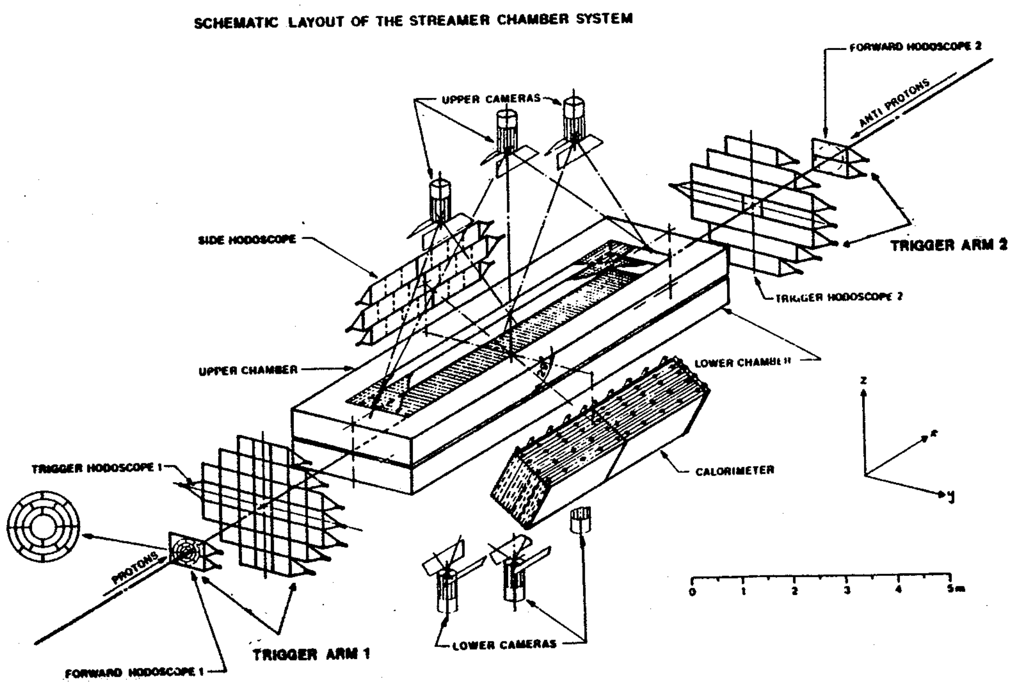

Figure II.3: The UA5 detector.

track resolution of about 2 mm. The events are photographed on film. This allows a fast evaluation of the data with well understood scanning, measuring, and reconstruction procedures developed for bubble chamber analysis. The advantage of an optical detector made it easier to cope with bad beam conditions (high background, asymmetric vertex position, cf. sections II.2.5 and III.6).

The experiment took its first data in the summer of 1980 at the CERN ISR with pp- and p$\bar{p}$-collisions of $\sqrt{s} = 53$ GeV [UA5 80]. This served mainly as a test for the apparatus under run conditions. Once installed in the Collider not much time was available for tests before the actual data-taking. The first data at the SPS Collider at $\sqrt{s} = 546$ GeV were taken in two periods in October and November 1981 [MEI 81]. With several modifications to the detector another run took place in 1982 [WAR 83b]. In March 1985 a third run was concluded [UA5 82a,RUS 85], where the Collider was operated in a pulsed mode varying the c.m. energy between 200 GeV and 900 GeV [RUS 82]. The emphasis here will be put on the data taken in 1982 and 1985 and reference made to earlier runs only for the sake of comparison.

The following sections are devoted to detailed descriptions of the various detector components.

II.2.2 Beam Pipe

The beam pipe has to meet two rather conflicting requirements. To hold the vacuum ($\approx 1 \times 10^{-9}$ Torr) it has to be mechanically stable enough. On the other hand, it should be as thin as possible so that particles produced in an interaction see as little material as possible when traversing it. In the 1981 run a 0.4 mm thick corrugated stainless steel beam pipe was used[2]. The corrugation increases the effective path length of particles traversing the steel, whose conversion probability for photons is relatively high. Abundant electromagnetic showers are seen in the streamer chambers obscuring parts of the event. Though they impair the analysis of charged primary[3] particles, especially in events of high multiplicity, electromagnetic showers provide a means of detecting and analyzing primary photons [MUE 83,UA5 82d].

For the 1982 run it was decided to concentrate on the analysis of primary charged particles and strange particle decays and to reduce the secondary interactions originating in the beam pipe. The old vacuum chamber was replaced by an uncorrugated 2 mm beryllium beam pipe of nearly elliptical diameter (55 mm $\times$ 147 mm). The beam pipe consists of 3 straight sections of beryllium joined together by 20 cm long sections of aluminium 4.8 mm thick. Although aluminium is just as unfavorable in producing electromagnetic secondaries as steel is, the overall electromagnetic background was reduced by a factor of about 5. This results in much clearer events in the chambers and simplifies the analysis significantly.

In order to repeat the analysis of photon production at 200 GeV and 900 GeV, a "Photon Converter" consisting of an aluminium box containing thin lead sheets with known conversion probability was introduced for part of the 1985 run between the beryllium beam pipe and the upper streamer chamber. A detailed description of the converter is found in [PEL 85].

[2] the corrugation enhances the mechanical stability

[3] particles produced in the p$\bar{p}$-collision as opposed to secondary particles produced in interactions in the detector material

II.2.3 The Streamer Chamber System

The principle of streamer formation is described in [RIC 74]. Charged particles traversing a medium in the presence of a strong electric field produce secondary ionization which results in the formation of avalanches. If the external field is applied only for a short time interval (a few nsec), the development will be arrested before discharge occurs. During the process of streamer formation light is also emitted in the visible spectrum and small luminous streamers elongated in field direction are visible along the particle trajectory.

To achieve a good resolution the streamer length should be as short as possible. Longer streamers, on the other hand, are more luminous and, therefore, easier to record on film. Hence one has to compromise between two conflicting requirements. The UA5 streamer chambers are operated with a streamer length of about 1.5 cm which guaranties a two-track resolution of 3 mm [GAU 84]. The streamer density is 1.5 streamers/cm.

The system consists of 2 identical streamer chambers, each with a sensitive volume of $6 \times 1.25 \times 0.5\ \mathrm{m}^3$, 9 cm apart[4] above and below the beam pipe (fig. II.4). Each chamber

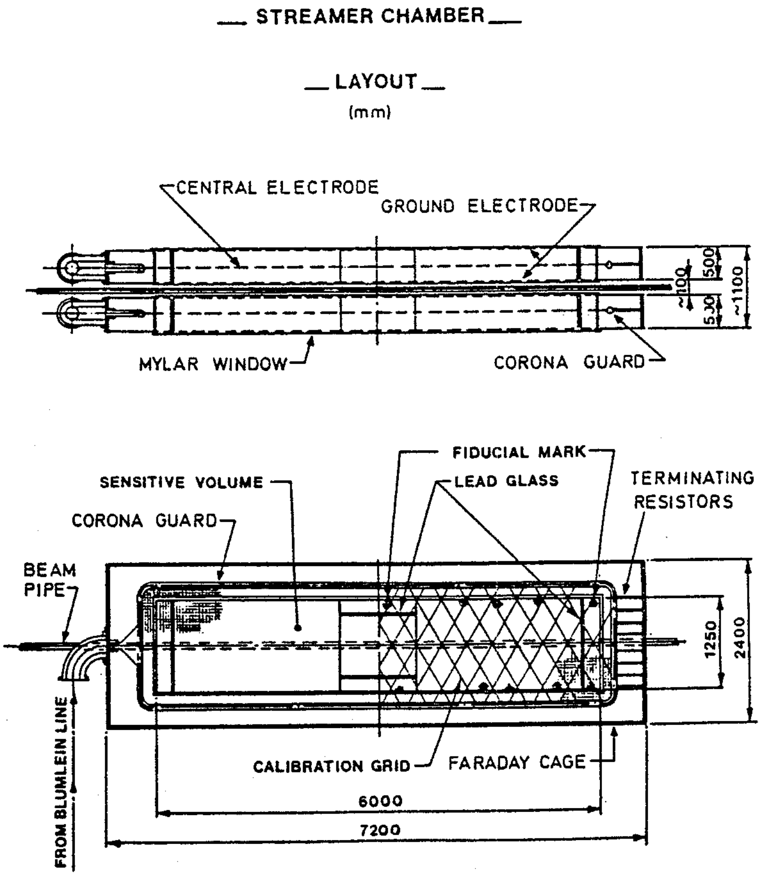

Figure II.4: The streamer chamber layout.

has 3 parallel electrodes 25 cm apart. They are made from a $0.5 \times 5\ \mathrm{mm}^2$ stainless wire mesh which has a transparency of 90% and is 50 μm thick (equivalent to 1% of a radiation length).

[4] The introduction of the photon converter plate made it necessary to raise the upper streamer chamber by about 1.5 cm for part of the 1985 run.

Originally the streamer chambers were equipped with 4 lead glass converter plates 16 mm thick (≈ one radiation length) to enable the detection of photon conversions. Of these all but one placed transversely 50 cm away from the end of the upper chamber, had been taken out in 1982. For the 1985 run the remaining one was removed as well.

The chambers are flushed with a mixture of 90% Neon, 9.5% Helium and 0.5% Isobutane continuously with a flow of 6 l/min. The Isobutane is added to lower the voltage necessary for a given streamer density [EGG 75a].

The streamer density falls exponentially with the delay time between the moment a charged particle traverses the chamber and the actual application of the high voltage pulse. The time constant of this curve is called "memory time". If a new event occurs faster than the streamers have decayed, old tracks from the previous event will still be visible in the chamber. A small admixture of SF_6 (≈ 0.2 ppm) reduces the memory time to 1.5 μs. SF_6 is an electronegative gas that rapidly absorbs photons. The amount of SF_6 in the chamber is monitored with special ionization chambers.

A detailed description of the high voltage generation and measurement is found in [GAU 84]. For each chamber a high voltage pulse of about 375 kV is supplied by a 16-step Marx Generator. The length of this pulse is shortened by interference in a Blumlein line to about 15 ns. The system is operated at about 1 Hz, though this repetition rate can be increased up to 2.5 Hz. The peak voltage, which determines the length and brightness of the streamers, can be controlled by the gap width and gas pressure in the Blumlein line. The actual voltage on the chamber is measured with 3 capacitive probes distributed along the chamber and recorded for each event. Events with a pulse height less than 3% from the optimal voltage are too faint to be analyzed and, therefore, rejected.

II.2.4 Optics

The entire sensitive volume of each chamber is photographed by two main and one supplementary camera (fig. II.3). The main cameras each view 2 overlapping halves of a chamber with a demagnification of 1/50. This configuration gives a good two-track resolution of about 2 mm and allows an adequate reconstruction of tracks transverse to the beam. The supplementary camera views the whole chamber with a demagnification of 1/80 at a poorer resolution. It is used for fast scans and as back up in case a main camera malfunctions. Each camera is equipped with a system of 4 mirrors that produce two stereo images of the chamber. These are necessary for a 3-dimensional reconstruction of the events.

The depth of field[5], determined by the chamber size and the inclination of the mirror system, limits the aperture of the cameras. On the other hand short streamers of low luminosity yield a good two-track resolution. It was, therefore, necessary to use image intensifier tubes to enhance the luminosity. Each camera is equipped with a 90 mm diameter two-stage image intensifier of the type ITT F-4093. Its overall gain is about ≈ 2000 and its resolution 55 line pairs/mm. Optical fiber plates transfer the image onto film. The maximum rate at which pictures can be taken with this system is 2.3 Hz.

Each chamber is supplied with two sets of 10 fiducial marks. These are electroluminescent plates placed above and below the chambers just outside the fiducial volume. Their exact position in space is known to 0.5 mm. They serve as reference points for the geomet-

[5] 610 mm

rical reconstruction (cf. section III.4). A calibration grid is used to determine the optical distortions caused mainly by the image intensifiers.

II.2.5 Trigger

Hodoscopes

The trigger supplies the streamer chamber system with the information whether an event of the desired type has taken place. Because of the short memory time of the chambers interactions have to be recognized and distinguished from background fast enough, before the ionization in the chambers has died away. In order to give a high as possible trigger efficiency for varying event types (cf. section III.1), the system has to be flexible. A high background rejection requires a good timing resolution. This is achieved by using a system of 6 scintillator hodoscopes in modular arrays shown in fig. II.3 :

- two arrays of $2.5 \times 2.5\ \mathrm{m}^2$ at each end of the streamer chambers containing 36 hodoscope modules (H1 and H2) and two arrays of $1.5 \times 1.0\ \mathrm{m}^2$ size placed at 90^0 containing 10 modules (H3 and H4). In 1981 H3 and H4 were situated on opposite sides of the chambers. From 1982 on H4 was replaced by a calorimeter (section II.2.6) and moved next to H3.

- two smaller hodoscopes consisting of 18 modules arranged in 3 concentric rings (F1 and F2). The inner ring fits closely around the beam pipe. They are placed behind H1 and H2 to get a better coverage of small angles (cf. section IV.2).

Each module is a light-tight box where a photomultiplier tube views a $35 \times 35 \times 2\ \mathrm{cm}^3$ sheet of scintillator directly. The time jitter is about 1 ns, the variation of the amplitude across the box is less than 30%. The forward hodoscopes F1 and F2 consist of a 1.9 mm thick scintillator and show a similar performance [ASM 81].

In order to reduce accidental hits and background noise strip counters[6] are placed in front of each hodoscope.

The $p\bar{p}$-Beam

The circulating proton and antiproton beams are confined by the radio frequency system of the SPS to buckets of 35 cm length. They are separated by at least 1/3 of the machine circumference. Therefore, the $p\bar{p}$-interactions occur in a well defined region within a time interval of 2 ns.

The number of interactions taking place is characterized by the luminosity of the beams. The luminosity $\mathcal{L}$ is defined as $\mathcal{L} = \mathrm{R}/\sigma$ where R is the interaction rate and σ the cross-section. It can also be expressed as a function of beam parameters :

$$\mathcal{L} = f \frac{N_p N_{\bar{p}}}{A_{\mathrm{eff}}},$$

[6] long scintillation counters

run period	21-22 Oct'81	4-10 Nov'81	16-21 Sept'82	16 Mar-4 Apr'85
beam momentum	273 GeV	273 GeV	273 GeV	100 to 450 GeV
initial luminosity $/\mathrm{cm}^{-2}\mathrm{s}^{-1}$	1×10^{25}	2×10^{25}	1×10^{27}	3×10^{26}
initial # p's in bunch	3×10^{10}	5×10^{10}	5×10^{10}	6×10^{10}
initial # $\bar{\mathrm{p}}$'s in bunch	8×10^{8}	5×10^{9}	4×10^{9}	7×10^{9}

Table II.1: Characteristics of the Collider beam during UA5 data-taking runs from 1981 to 1985.

where f is the bunch crossing frequency, N_p ($N_{\bar{p}}$) the number of protons (antiprotons) per bunch, and A_{eff} the effective beam crossing area [RUS 80]. The luminosity and other run conditions are summarized in table II.1.

The luminosity declines rapidly due to interactions of the beam particles with the rest gas molecules and beam-beam interactions. New fills are necessary every few hours. For different fills the bunches might occupy various radio frequency buckets. This causes a displacement of the bunch crossing point; two adjacent RF buckets are separated by 0.75 m, corresponding to a time difference between the two buckets of 5 ns.

Apart from genuine proton antiproton interactions, background interactions are also present. The predominant source of background are "halo" particles which have escaped from the bunches. They can produce showers when interacting with the beam pipe or other upstream material. Beam particles interacting with the molecules of the residual gas in the beam pipe produce background as well.

Trigger Logic

The signals coming from the trigger hodoscopes are processed and stored in CAMAC units. They supply information on hit patterns and hit multiplicities [MUE 83,SCH 86].

A bunch crossing signal is provided by two upstream directional couplers at either side of the interaction region that detect a passing particle bunch. A signal derived from the beam crossing signal defines the average time at which interaction products should arrive at the hodoscopes. A coincidence with hodoscope signals defines an "in-time" hit.

Halo particles are produced by beam particles interacting with material outside the detector. They accompany the beam and reach the downstream hodoscopes at the same time as the products of beam-beam interactions. They also cross the upstream hodoscopes, however, and produce an early out-of-time hit. Any hit occurring in a 50 ns period before the bunch crossing signal causes the trigger to be vetoed.

The trigger hodoscopes are combined to define a two-arm trigger (H1 and F1 form arm 1 on the incoming proton side, H2 and F2 form arm 2 on the incoming antiproton side, denoted A1 and A2, respectively, fig. II.3). Background particles caused by beam-gas interactions or halo interacting with the beam pipe tend to be strongly collimated in the forward direction with most particles going in one direction and none in the other, hitting only one hodoscope. These background events are suppressed by requiring at least one hit in both arms ($A1 \times A2$)[7]. This condition defines the least restrictive trigger, therefore, called "minimum bias" trigger.

Single arm triggers of the type $A1 \times \overline{A2}$ and $\overline{A1} \times A2$ (at least one hit in one arm and none in the other) were also introduced to study special "non-minimum-bias" event types, these will be described in section III.1.[8]

Background events still passing the trigger requirements and exposed onto film were rejected by scanning the film (cf. section III.2) or by applying offline cuts to the data (cf. section III.6).

II.2.6 Calorimeter

In addition to the detector components described in the previous chapters a calorimetry device was added as new equipment in 1982. Its task is to detect neutral hadrons and to allow a rough energy measurement of both charged and neutral hadrons and photons and to aid the detection of "Centauro" events [RUS 79].

The calorimeter is shown in fig. II.5. It was placed about 2 m away from the inter-

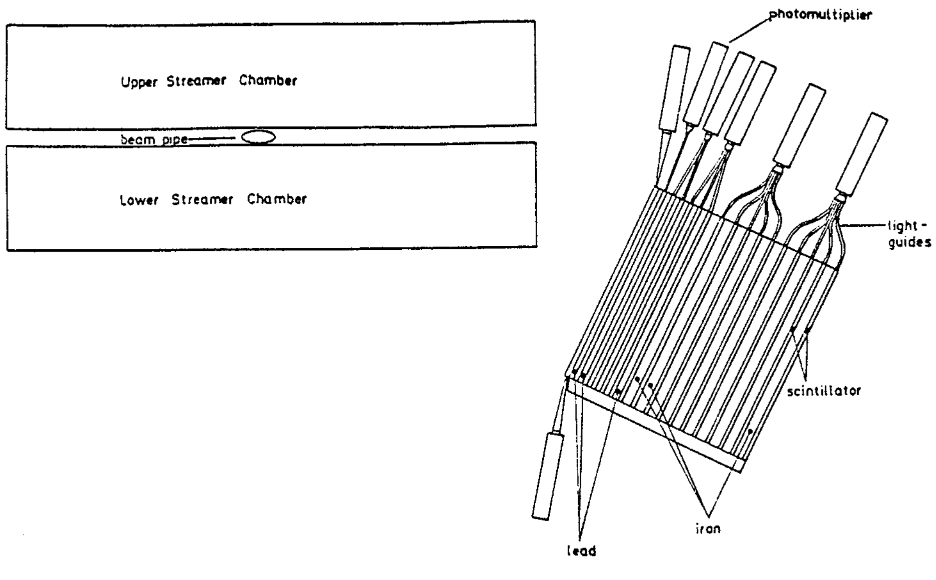

Figure II.5: The UA5 calorimeter.

section point (fig. II.3) and covered 8% of the azimuth and the range between +1 and -1

[7] In 1981 the luminosity was low and background dominated. The number of protons exceeded the number of antiprotons by a factor of 50, so that background triggers were mainly due to proton halo or proton-gas interactions producing particles in direction of arm 2. Therefore, the number of hits required in arm 1 was two.

[8] In fact, in 1985 most of the running was performed with a trigger requiring only one hit in A1, which includes both $A1 \times A2$ and $A1 \times \overline{A2}$. The trigger $\overline{A1} \times A2$ was heavily contaminated by background and, therefore, not used.

of pseudorapidity. It is divided into 10 identical modules 1 m high and 40 cm wide each. This reduces the masking in the case of several particles hitting the calorimeter at the same time. Each module contains a lead-scintillator sandwich section to detect photons and an iron-scintillator sandwich section to detect and give a rough energy measurement of hadrons. The first section contains 6 lead sheets alternating with 6 scintillator plates. Each lead plate is 2.5 cm thick corresponding to over 25 radiation lengths. Essentially all photons convert in this section. The second section consists of 10 iron sheets alternating with scintillator plates, each iron plate being 5 cm thick.

As readout system BBQ wavelength shifter bars are used in order to have a uniform photomultiplier response of particles passing any point in the scintillator. The scintillators in the sandwich sections are grouped for read-out. In the lead section the first scintillator is read out alone, and the two following ones, as well as the last three, are read out together. In the iron section each half is read out as one unit.

The calorimeter was calibrated in test beams, where it was exposed to various particle beams ($e, \bar{p}, p, \mu$) of momentum between 0.7 to 15 GeV/c [AND 84,FRO 85]. A detailed description of the apparatus and data taking during the 1985 run can be found in [BUR 87].

Chapter III

Data Acquisition and Analysis

III.1 Introduction

The total $p\bar{p}$-cross-section consists of the following contributions :

- The elastic cross-section, that makes up about 23% of the total [UA4 84,UA4 87].
- The inelastic cross-section, which is again made up of the following components :
  - "Single-diffractive" (SD) events, where only one of the colliding beam particles is excited into a state of higher mass M and subsequently decays into final state particles. The cross-section $d\sigma/dM^2$ for this process is seen to decrease as $1/M^2$, and has a small 4-momentum transfer, implying that the decay products are very close together in momentum space in the initial direction of the excited beam particle. Therefore, these events are characterized by a very asymmetric topology.
  - "Double-diffractive" (DD) events, where both beam particles are excited and decay as in single-diffractive events.
  - "Non-diffractive" (ND) events, which make up the bulk of the inelastic cross-section.

  The double diffractive component has a similar topology as the non-diffractive one. Since they cannot easily be distinguished in this experiment, they are grouped together into one class of events, denoted as "non- single-diffractive" (NSD).

The data taken during the runs in 1982 and 1985[1] for different trigger conditions (cf. section II.2.5) are summarized in table III.1. Apart from the so-called "minimum bias" trigger, a certain number of pictures were also taken with a "diffractive" trigger that enhances the amount of single-diffractive events (either diffractive dissociation of the proton or the antiproton), depending on which trigger arm is vetoed. Fig. III.1 illustrates the relationship between different trigger types and physical processes as derived from Monte Carlo simulations (cf. section III.7).

The basic 2-arm trigger is highly efficient for all non- single-diffractive events ($\approx 95\%$), only about 5% give a single-arm trigger. Single diffractive events, on the other hand, tend to be asymmetric, and, therefore, most of these give 1-arm triggers ($\approx 70\%$). The

[1] No detailed description of the 1981 data [MUE 83] is given here. A total of 16 K good events was obtained in 1981, though with a significantly lower beam luminosity and worse background conditions (cf. table II.1).

trigger type	trigger setup	# pictures	$\sqrt{s}$/GeV	fraction of $p\bar{p}$-events in the data
		1982[a]		
minimum bias	A1 × A2	28.6 K	546	91%
$\bar{p}$-diffractive	A1 × $\overline{\text{A2}}$	7.6 K	546	16%
p-diffractive	$\overline{\text{A1}}$ × A2	7.4 K	546	2.5%
		1985[b]		
minimum bias	A1 × A2	46.6 K 15.7 K 22.2 K	900 800,540[c] 200	97% 94%
$\bar{p}$-diffractive	A1 × $\overline{\text{A2}}$	7.8 K 3 K 16.9 K	900 800,540[c] 200	27% 8%

[a] 60% of the events were recorded only with the two supplementary cameras, 40% with both main and supplementary cameras (cf. section II.2.4).

[b] 47% of the data was taken with the chambers "closed", 17% with the chambers "open" and the photon converter in place, and 36% "open" but without the converter (cf. section II.2.3).

[c] The numbers represent averages of a range of energies.

Table III.1: Data and trigger conditions taken during the 1982 [MAG 82b] and 1985 [SCH 86] runs.

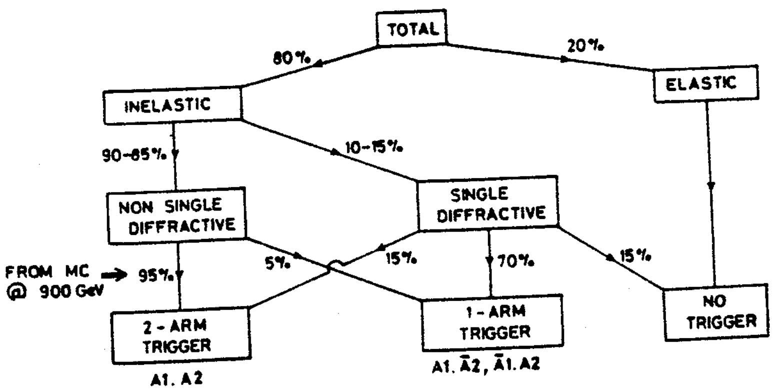

Figure III.1: Relationship between physics processes and triggers at 900 GeV [WAR 85a].

remainder either fails to trigger or give a 2-arm trigger. However, since single-diffractive events constitute only 15% of the inelastic cross-section, almost all two-arm triggers (> 98%) are, therefore, NSD events.

Small events sample were recorded under very special conditions :

- In the 1982 run :
  - A small data sample ($\approx$ 3 K events) was taken using the energy deposition in the calorimeter as additional trigger requirement, i.e. a coincidence of a 2-arm trigger and a transverse energy of more than 3 GeV. The energy is defined as the maximum energy deposition from combinations of 3 adjacent NHD modules.
  - Furthermore, a sample of 3 K events was taken with an extra 2 ms delay between the occurance of a trigger and the firing of the streamer chambers, giving a reduced streamer density. A Monte Carlo study had indicated that particle identification on the basis of ionization measurements could be possible in that case.
- In the 1985 run :
  - Another 4 K events were taken with a shifted interaction vertex position (in an adjacent RF bucket) to study asymmetric single-diffractive events.

Both the events on film and the electronic data are processed, their relevant information extracted according to procedures that will be described in this chapter. A detailed description of how the electronic data coming from the calorimeter (about 500 K events were recorded with only the trigger information and the calorimeter data) are analysed is given in [BUR 87].

III.2 Event Scan

The remaining fraction of background events, especially in the one-arm trigger data, required a preselection to measure only good events. The events were scanned; those satisfying the following criteria were rejected as background :

- No tracks pointing to the expected vertex region.
- Tracks traversing the whole chamber. This indicates halo background.
- An upstream interaction outside the vertex region having 3 or more tracks pointing towards the primary vertex in question and less away from it. Either the "primary" interaction is produced by upstream interaction products, or it is a true primary interaction contaminated by tracks coming from the secondary interaction.
- In 1982 the timing of the trigger was not as good as in the later run, highly asymmetric events with at least 15 tracks more in one hemisphere than in the other, resulting from beam-gas or halo-beam pipe interactions, had to be rejected.

Rejecting good events that by chance fulfill these criteria because they were accompanied by beam-gas interaction products would not introduce any bias, since the primary interaction and background events are uncorrelated.

Due to fluctuations in the high voltage pulse applied to the streamer chamber, some events showed very faint tracks that cannot be measured reliably. Events that had a high voltage amplitude of less than 97% of the average were, therefore, rejected.

Special scans were also carried out to find strange particle decays (V^0-decays and "kinks" from K, Λ, Ξ). These are described in detail in [UA5 82c,UA5 85a,UA5 85b,HOS 86].

III.3 Event Measurement

All tracks on the accepted events were measured, even those coming from obvious secondary interactions. Excluded were only the following special cases:

- Delta rays (electrons of a few MeV) undergo several changes of direction due to multiple Coulomb scattering and do not form straight tracks.
- Secondary interactions, usually due to showers in the beam pipe, create regions densely populated with tracks and, therefore, very difficult to measure. These regions were marked (Q-labels) and omitted in measurement.
- Tracks emerging behind the lead glass plate could be partially masked due to shadowing of the plate.[2]

The events were measured by the collaborating laboratories on several different devises: in CERN and Bonn the Erasme-system was used, as well as Sweepniks and a Spiral Reader in other laboratories. Only the measuring procedure for the Erasme will be outlined shortly, more detailed information is found in [HOS 82,MEI 78].

The Erasme system is an interactive computer supported measuring system allowing operator intervention. Both streamer chambers are measured independently and are recombined after the geometrical reconstruction (cf. section III.4). For each chamber 4 stereo views are measured if the two main cameras are used. The start and end points of each track are first digitized manually, then intermediate points are interpolated automatically. An online geometry program can be used to predict start and end points of the same track on other views. These are then measured precisely. It also provides a check for badly measured tracks, that are then remeasured.

III.4 Geometrical Reconstruction

In order to reconstruct a track in space it is necessary to remove the distortions in the optics system, in particular those introduced by the image intensifiers. Various parameters are used to describe the distortion effects of the optics system, these are called optical "titles". A detailed description of the optics titles and the geometrical reconstruction is found in [BUR 82], [FIS 83]. The titles are determined independently for each camera from a survey,

[2] only for the 1982 run.

giving the actual space positions of the grid intersections and fiducial marks, and a careful measurement of these on film by means of a fitting program.

Due to the fact that most surveyed marks are near the top plane of the chamber the predicted optical titles give poor reconstructions of points away from this plane. Therefore, a set of corresponding points[3] was included as a further constraint on the titles. The bulk of these points were chosen as start points of tracks. These are known to be close to the entry plane of the chamber and, therefore, compensate for the lack of surveyed points on this plane.

III.5 Vertex Reconstruction and Particle Identification

III.5.1 Introduction

A typical streamer chamber event at 546 GeV has about 40 charged particles visible in the chambers, of these 23 originate in the primary interaction, 17 are secondary particles. These can be distinguished according to their origin as electromagnetic showers (5 particles), hadronic showers (7), weak decays (2), and δ-rays (3). An example of an event, as seen on film, is shown in fig. III.2.

For an analysis of events the location of the primary vertex has to be found, and particles pointing to it to be distinguished from those pointing to secondary interactions. The following possibilities for tracks visible in the chambers have to be considered (fig. III.3):

- Primaries (a) point to the primary vertex if they have not interacted in the detector material before entering the chamber. Those entering beyond the lead glass plate (b) are not considered.[4]
- A clearly visible kink (c) in a primary track can come from a π, K-decay, or Coulomb-scattering on the middle electrode or chamber gas.
- "V^0-decays" of K^0, Λ in the chamber (d).
- Hadronic and electromagnetic showers or photon conversions in the beam pipe or chamber bottom (e).
- Strange particle decays outside the chamber (f).
- Very close primaries in the forward regions (g).
- δ-electrons (h).
- Tracks not pointing near any vertex (i).

III.5.2 Reconstruction Algorithm

The primary interaction vertex is, of course, located inside the beam pipe and is, therefore, not visible in the chambers. But one can determine the exact position of the primary

[3] The image from a unique point in space is identified and measured on two views.

[4] only for the 1982 run.

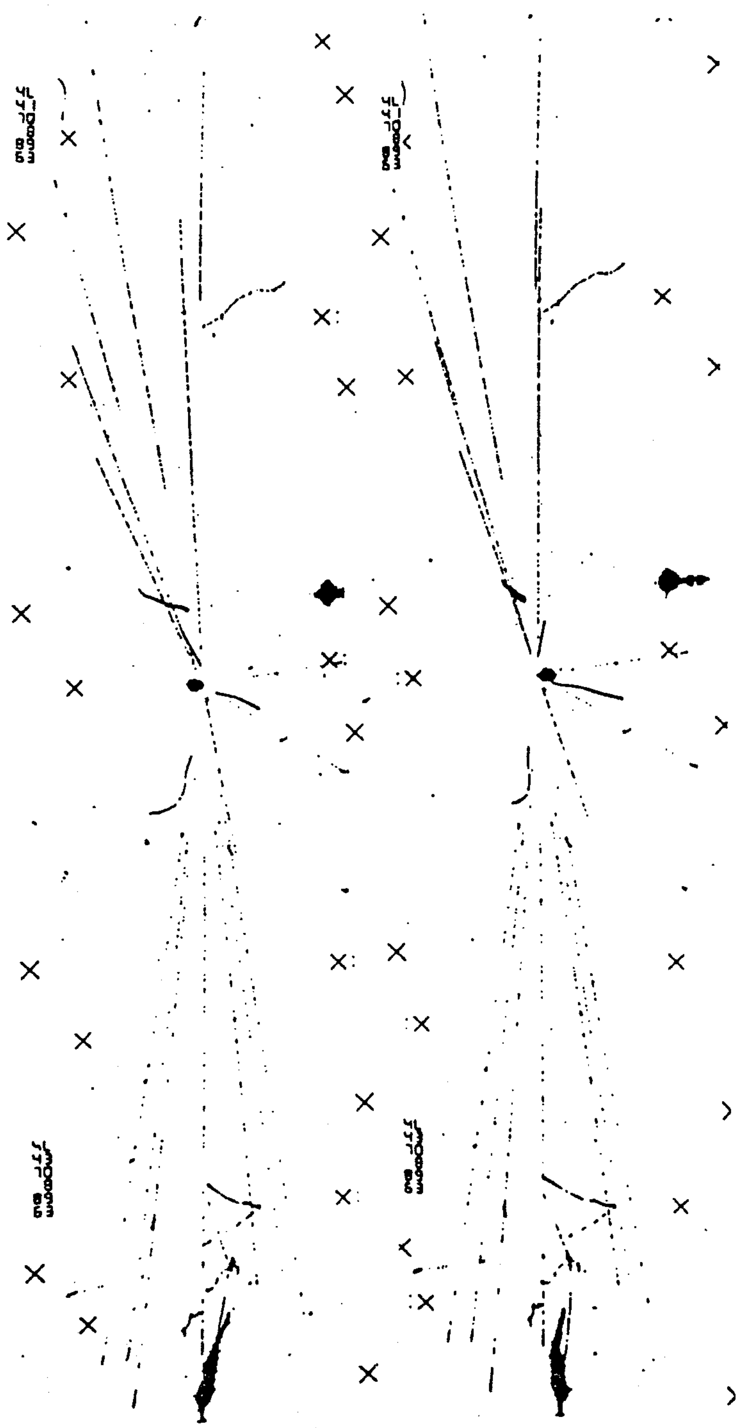

Figure III.2: Streamer chamber event at 900 GeV.

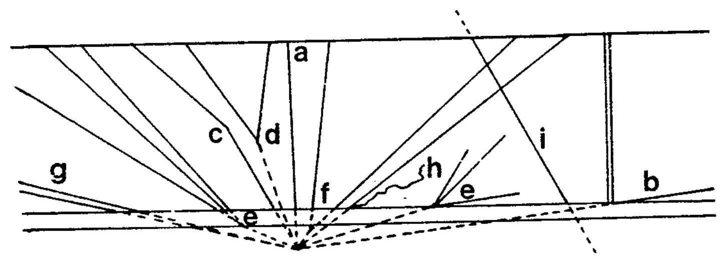

Figure III.3: Tracks visible in the chambers (cf. text for explanation).

vertex from the beam dimensions and extrapolation of visible tracks backwards into the beam pipe.

Knowledge of the vertex position can then be used to separate so-called "primary" particles, i.e. those originating in the primary vertex, from "secondary" particles coming from secondary interactions in the beam pipe and chamber bottom.

The primary vertex is found by the following algorithm (VFIND) [WAR 80]:

The transverse dimensions of the proton and antiproton bunches are known quite accurately to within 1 – 2 mm. This defines a beam axis on which the collision point must lie. Because the colliding particles are confined to RF buckets of length of about 35 cm and separation of about 75 cm, the longitudinal coordinate cannot be deduced from the bunch crossing point.

Therefore, the measured tracks in the chambers are extrapolated backwards toward the beam axis to find the point of closest approach. The average of these points (called the pointing distance d_{pt}) is used as a first approximation for the coordinates of the primary vertex. Only tracks whose length traversed in the chamber is at least 10 cm are used. Very short tracks cannot be measured accurately enough and, therefore, do not point very well to the vertex. Tracks with frequent changes of direction that have an RMS[5] of greater than 30 μm are disregarded.

In the next step secondary tracks are separated from those coming from the primary interaction. Since most secondaries are produced in electromagnetic or hadronic showers, or photon conversions, each will have neighbors close by, i.e. the distance to the nearest neighbor d_{ij} will be small; and they do not point very well to the primary vertex. For primary tracks the opposite holds, they tend to be produced well separated and of course point very well to the primary vertex.

A scatterplot of the distance to the nearest neighbor d_{ij} verses the pointing distance d_{pt} (fig. III.4) illustrates the cut that is used in the data to separate primaries and secondaries. The actual location of the cut is chosen to minimize the losses of primaries assigned wrongly as secondaries and balance those against the number of secondaries assigned as primaries. The cut parameters, therefore, change slightly for different regions of pseudorapidity. With a first separation of primaries from secondaries one finds a better estimate of the primary vertex by using primary tracks only. The procedure is iterated until the position of the primary vertex changes by less than 2 mm. After this is done, the secondary tracks are

[5]The RMS measures the deviation of the measured points on a track from the straight line fit through thses points.

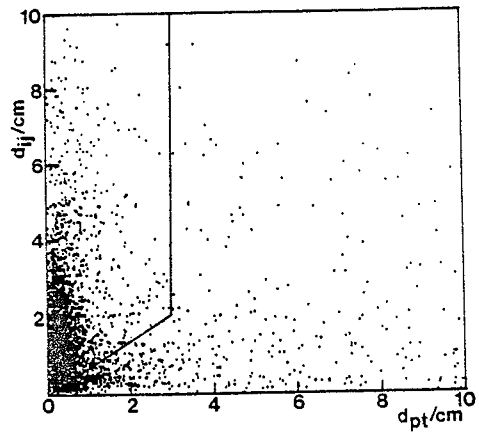

Figure III.4: Separation of primaries and secondaries in the data for a pseudorapidity interval $2 < \eta < 3$.

linked together to secondary vertices by associating groups of tracks with small values of d_{ij}.

III.5.3 Reconstruction Efficiencies

The efficiency of the algorithm and the cuts used can be judged by applying these to Monte Carlo simulated data (cf. section III.7). Fig. III.5 shows the deviation of the VFIND-primary vertex from its true location. The average deviation is 2.2 mm, for 85% of the

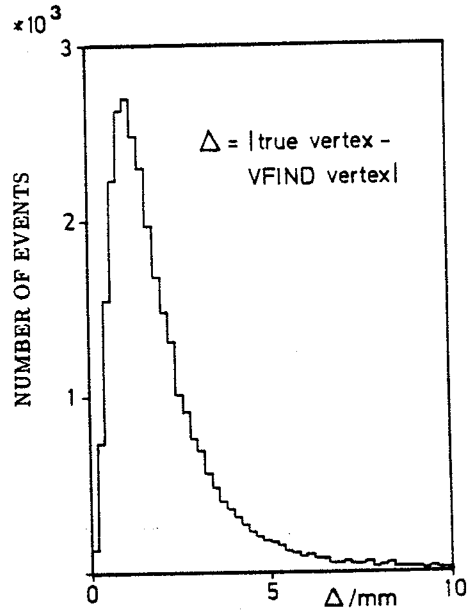

Figure III.5: Deviation of VFIND-primary vertex from true vertex.

events the vertex position is determined to better than 5mm. Very low multiplicity events give a less accurate estimate of the primary vertex, for events with an observed multiplicity less than 5, the average deviation is about 5 mm.

Fig. III.6 illustrates the efficiency of the cuts on Monte Carlo data for primaries and secondaries. The cuts work well for primaries, excluding secondary showers, though many

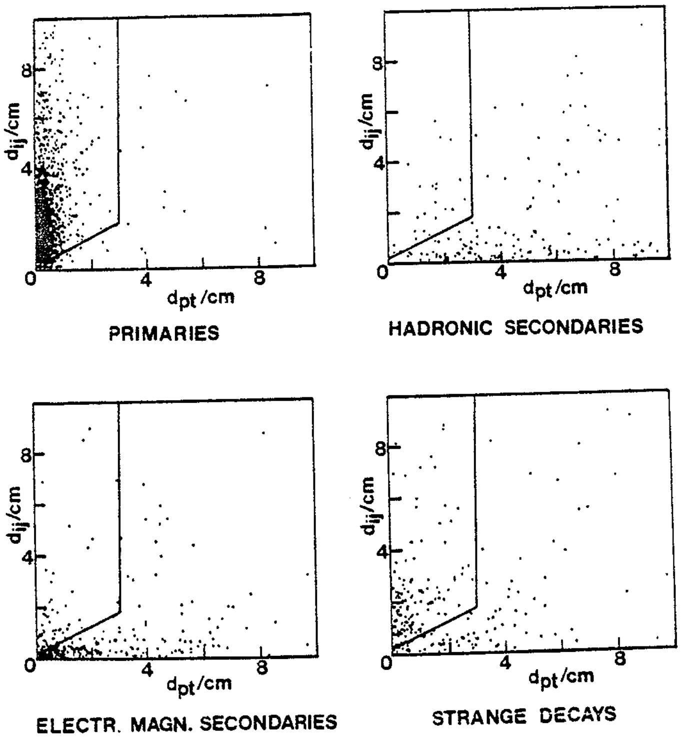

Figure III.6: VFIND cuts on Monte Carlo data.

secondaries coming from weak decays are accepted as primaries if the decay vertex lies inside the beam pipe. The composition of VFIND-primaries and VFIND-secondaries is shown in fig. III.7 as a function of pseudorapidity η. In the forward regions more particles originating in secondary showers are assigned as primaries. This is because the solid angle decreases for large rapidity values, tracks tend to be closer, and the nearest neighbor cut is less effective. It should be stressed that the algorithm is tuned to find as large and clean as possible a sample of primary particles, with the effect that the identification of secondaries is less good. In order to analyze strange particle decays or photon conversions other techniques have to be used [MUE 83,HOS 86]. The overall composition of VFIND-primaries is shown in table III.2 for all events, and for high multiplicities separately. The absolute number of secondaries confused as primaries increases with multiplicity. Therefore, the percentage of "true" primaries in the VFIND-primary sample is fairly independent of multiplicity.

III.6 Reduction of the Data Sample

After reconstruction the relevant data for each event obtained from the film analysis and the electronic information recorded during the run is collected on a DST (Data Summary Tape). Because the analysis described in the following chapters requires very clean data with a good detector acceptance, the following refers only to the data samples taken under the best conditions, i.e. for 546 GeV the events recorded on all main cameras[6], and for

[6] Having only one camera per chamber, i.e. only two views available, decreases the accuracy of the geometrical reconstruction.

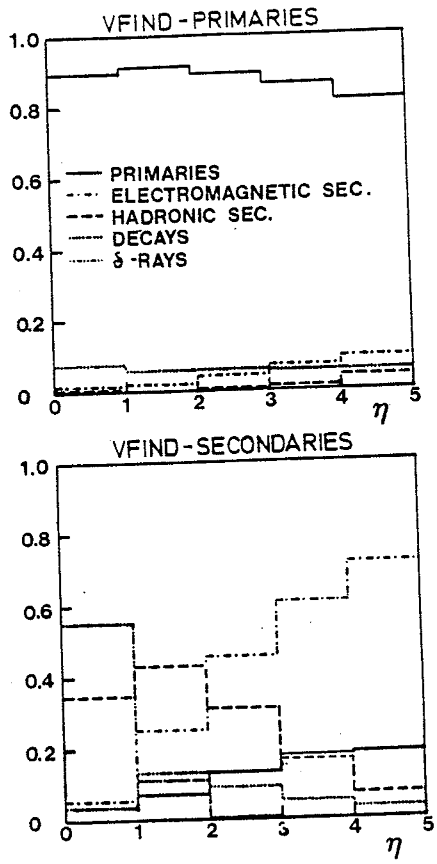

Figure III.7: Composition of VFIND-primaries and VFIND-secondaries.

particle	all n	n > 54
true primaries	20.77	57.13
hadronic secondaries	0.19	0.36
electromagnetic secondaries	0.79	1.79
weak decays	1.44	4.14
δ-electrons	0.01	0.01
Dalitz-electrons	0.17	0.53

Table III.2: Composition of VFIND-primaries for all events and those with observed multiplicity n>54 (illustrated for 546 GeV).

200/900 GeV only data without the photon converter and the best geometrical acceptance was taken.

The final minimum bias DST of the 1982 run at 546 GeV contained 7904 events; the 1985 DST contained 3944 events at 200 GeV and 6595 events at 900 GeV.

The raw data collected on the DST has to be reduced further for the following reasons:

- On a few events no primary vertex could be found by the vertex finding algorithm.
- Background events can be missed in the scan, when only the 2-dimensional projections on film are available and the position of the interaction vertex unknown.
- Some events have a primary vertex that is not centered in the chambers.

The cuts applied are the following:

- Events with no primary tracks found are rejected.
- For most events the longitudinal position of the interaction vertex lies in the center between the two chambers (for the 546 GeV data it is shifted about 35 cm longitudinally from the chamber center), corresponding to the beam crossing point. Some events, though, originate from beam particles in other radio frequency buckets; the interaction is then not centered with respect to the chambers and a great percentage of particles are lost outside the chamber acceptance. Such events have to be rejected, even though they are good $p\bar{p}$-events, because corrections for the losses would become too large. Therefore, only events deviating less than 35 cm from the average longitudinal vertex position are accepted.
- Events whose transverse deviation from the nominal beam axis is more than 2 cm are rejected.
- One-prong events (only one primary track was found) have to be treated separately. Here of course the position of the primary vertex is unknown. It is assumed to be the point of closest approach when extrapolating the track back to the beam axis. Then the same longitudinal and radial cuts described above are applied. Furthermore, if more than 3 upstream secondary tracks are present, the event is rejected as well. This cut is illustrated in fig. III.8.

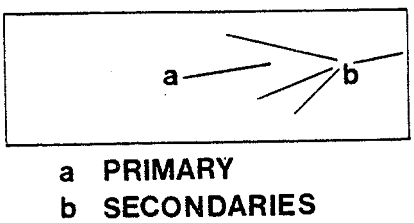

Figure III.8: Upstream vertex cut for one-prong events.

In table III.3 the influence of the various cuts is summarized. A large portion of the events is rejected because of vertex cuts. The comparatively large number of 0-prongs in the 546 GeV data is due to the fact that the trigger timing was less good in the 1982 run.

$\sqrt{s}$/GeV	200	546	900
minimum bias events on DST	3944	7904	6595
0-prongs	15	182	16
1-prongs	39	66	33
1-prongs accepted	21	29	15
events with more than one primary track	3890	7656	6546
passing vertex cuts	3856	7496	6514
total number of events accepted	3877	7525	6529

Table III.3: Number of events passing cuts (cf. text for explanation).

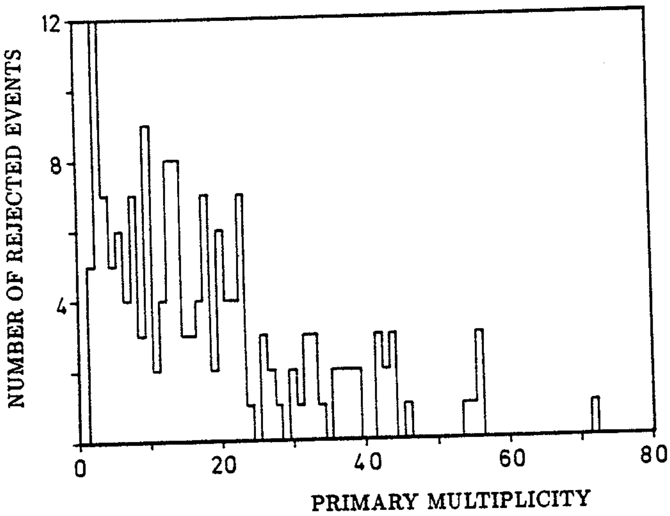

Figure III.9: Primary multiplicity distribution of rejected events excluding 0- and 1-prongs.

Fig. III.9 shows the primary multiplicity distribution of rejected events (excluding 0- and 1-prongs). The high multiplicity events are those whose vertex lies in the wrong RF bucket. The enhancement at low multiplicities indicates the difficulty of determining the primary vertex when few tracks are available for extrapolation.

An example of the longitudinal (x) vertex position for 1982 data is shown in fig. III.10 (the coordinate system is indicated in fig. II.3). The bulk of the events show a nearly

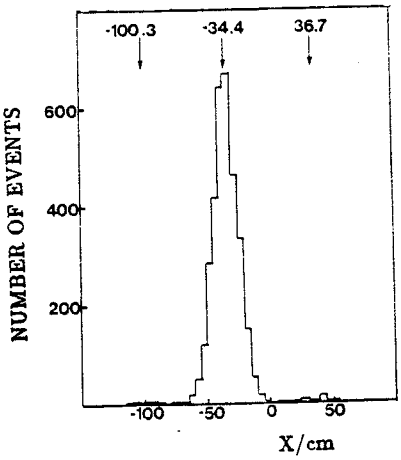

Figure III.10: Longitudinal position of the primary vertices.

gaussian distribution centered around -35 cm. In addition a few events are shifted 75 cm to both sides, corresponding to adjacent RF buckets. These were rejected. In the 1985 data all events were centered around $\langle x \rangle \approx 0$. Fig. III.11 shows the transverse (y,z) vertex positions. The beam pipe diameter is indicated. Only few events lie outside the RMS-cut of 2 cm.

The location of secondary vertices reflects the amount of material tracks have to traverse. The x-distribution of secondary vertices (fig. III.12) peaks in the vicinity of the primary vertex. Secondary interactions produced by clamps holding the beam pipe are identified by VFIND and show up as 4 conspicuous spikes in the figure. As illustrated by the (y-z) distribution in fig. III.13, the bulk of secondaries originates in the beam pipe and chamber bottoms. Vertices found inside the beam pipe are faked either by wrongly assigned primaries or electromagnetic showers (if tracks originating in a shower are very close together, they cannot be extrapolated very accurately to find their common vertex).

The 1982 data was contaminated more with background events than the 1985 data. If there would be any residual background, in particular beam-gas events in the 1982 data, after the cuts have been applied, these would be expected to cause an asymmetry associated with the more intense proton beam; i.e. the number of all tracks n_F to one side of the primary vertex (in x-direction) would on the average not be equal to those n_B on the other side. The asymmetry

$$A = \frac{n_F - n_B}{n_F + n_B} = 0.0008 \pm 0.0030$$

was found to be negligible.

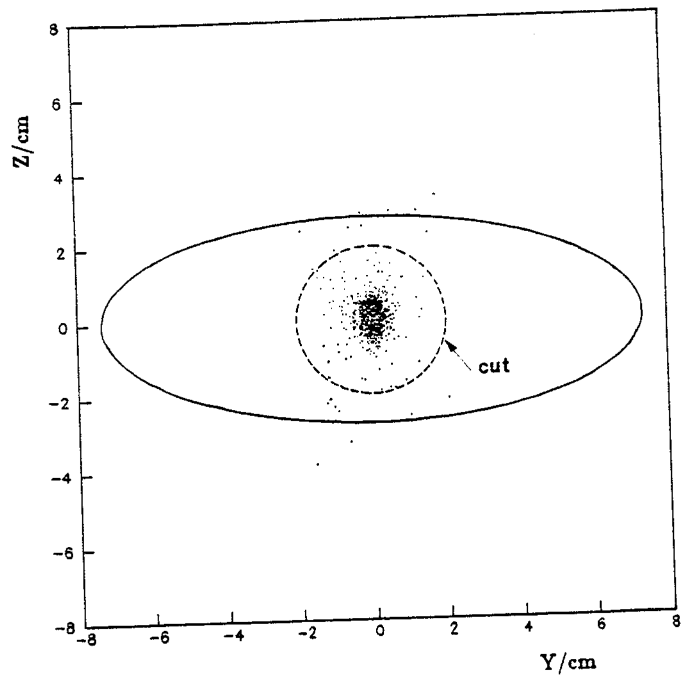

Figure III.11: Transverse position of primary vertices (the diameter of the beam pipe and the cut applied to the data are indicated).

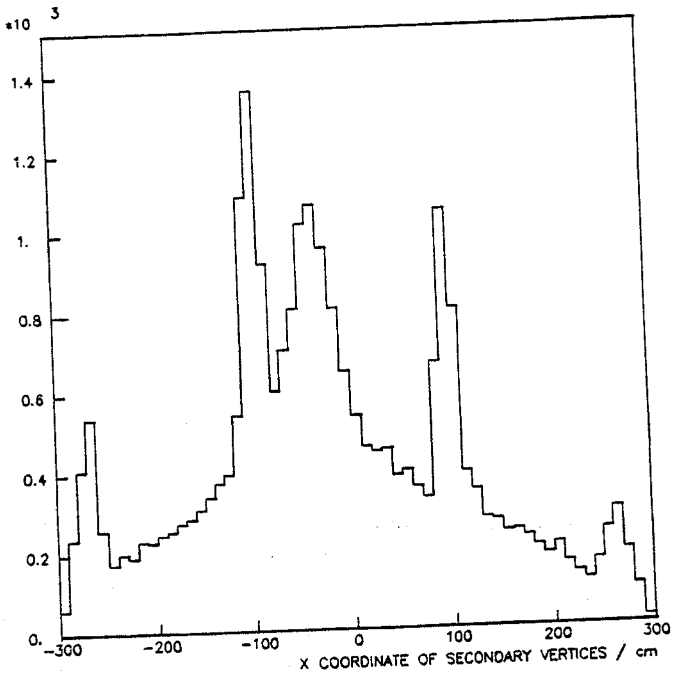

Figure III.12: Longitudinal position of secondary vertices.

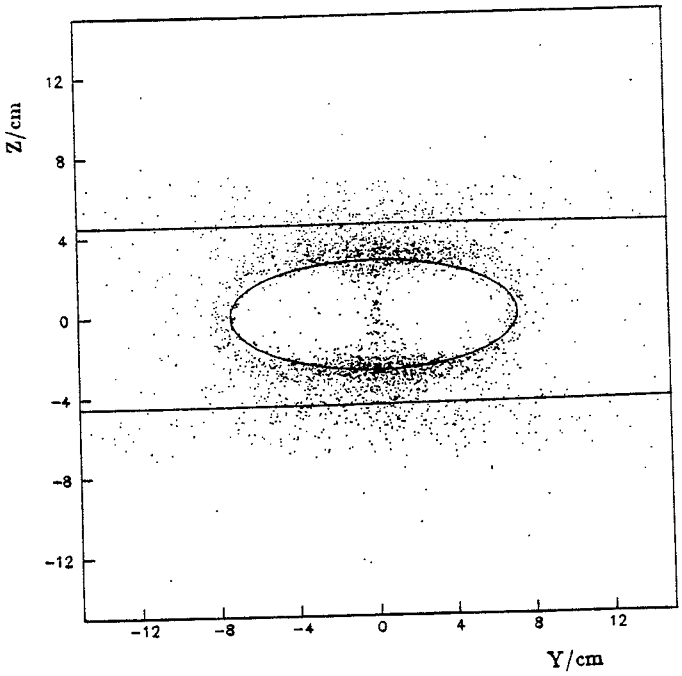

Figure III.13: Transverse position of secondary vertices (the diameter of the beam pipe and the chamber bottoms are indicated).

III.7 UA5-Monte Carlo Program

III.7.1 Introduction

The structure of events seen with the UA5-detector is biased in the sense that the particle distributions are distorted by finite acceptances, measurement errors, cuts on data samples, etc., and have to be either corrected for or, if this is not possible, compared to simulated events subjected to the same distortions. The first method is discussed in the following chapter, whereas the latter method will be used in chapter VI. The complexity of high energy particle collisions and of the experimental setup necessitate the use of Monte Carlo simulation techniques, rather than analytic treatments.

The UA5-Monte Carlo program consists of two parts. The first,which is detector independent, produces the final state particles of the $p\bar{p}$-collision at a given c.m. energy. It is tuned to reproduce the properties of low transverse momentum $p\bar{p}$-interactions at Collider energies. This event generator will be described in the following subsection.

The second part simulates how the detector and the analysis system would respond to a given event. This involves tracking each particle through the detector material (beam pipe, streamer chambers, trigger hodoscopes, calorimeter, and interspersed material), where it undergoes secondary interactions, is scattered, or decays. Standard program packages can be used to follow the passage of a particle through material. After the response of the detector, the analysis system has to be simulated. This involves the measuring process, where optical distortions and measurement errors have to be taken into account. The standard geometrical reconstruction program (cf. section III.4) and, finally, the vertex finding procedure (cf. section III.5) are then applied to the simulated data. A more complete description is given in [WEI 82,UA5 87a].

III.7.2 The UA5-Event Generator

The event generator [WEI 82,UA5 87a] can simulate two different classes of $p\bar{p}$-interactions, namely non-diffractive events ("GENCL") and diffractive events ("DIFFR"). The diffractive component is outlined in [SCH 86], only the non-diffractive event simulation is described here :

- First the charged particle multiplicity distribution is generated from a negative binomial distribution [UA5 85d], the parameters of which are taken from energy dependent fits to published data [UA5 86a].
- The particle composition is determined using energy dependent parametrizations of particle ratios [UA5 85a,UA5 85b]. Only nucleons, hyperons, Ξ's, Kaons, and Pions are produced.
- The particles are grouped into clusters of different types :
  - Two leading clusters consisting of a leading particle (nucleons or Δ's) each.
  - Central baryons and strange particles are produced in pairs to locally conserve the baryon and strangeness quantum numbers.
  - Pions, that make up 80-90% of the total, are produced in clusters whose size is determined from a Poisson distribution with an average of 2 charged pions per cluster.
- All clusters that contain more than one particle receive an additional "excitation" energy in terms of extra mass.
- The transverse momenta of these clusters are generated from an exponential or a power-law distribution; the azimuthal direction is distributed uniformly.
- The longitudinal momenta are generated from a "pre-rapidity" distribution with a flat top and Gaussian wings (the leading clusters are assigned the smallest and largest values), such that energy and momentum conservation holds [JAD 72].
- Finally, all clusters and short-lived particles decay isotropically.

Detailed comparisons of the event generator data with physics results have been made [UA5 87a]. The properties pertaining to the cluster formation and decay process will be analyzed in chapters V and VI.

Chapter IV

Charged Particle Pseudorapidity Densities

IV.1 Introduction

In general the interaction of two particles a and b is of the form :

$$a + b \longrightarrow c_1 + c_2 + \cdots + c_n \ ,$$

where $c_1, c_2, \ldots, c_n$ are the n particles produced in the final state. In very high energy experiments the number of particles produced in an inelastic interaction is on the average so large that it is impractical, and in most cases impossible, to determine exclusively all kinematical variables to completely describe the final state. One, therefore, resorts to the study of the inclusive interaction :

$$a + b \longrightarrow c_1 + c_2 + \cdots + c_m + X \ ,$$

where only the m-particle production characteristics are determined, regardless of the remaining (n-m)-particles ("X").

The differential cross-section $d^3\sigma$ of the production of particles $c_1, \ldots, c_m$, where an implicit sum is made over states with various quantum numbers which comprise X, is usually denoted in the Lorentz invariant form as

$$d^3\sigma = f_{ab}^m(\vec{p}_1, \ldots, \vec{p}_m; s) \prod_{i=1}^{m} \frac{dp_i^3}{E_i} \ , \tag{4.1}$$

where $\vec{p}_1, \ldots, \vec{p}_m$ and $(E_1, \ldots, E_m)$ are the particle momenta and energies, respectively, and s the square of the c.m. energy. The function f_{ab}^m contains the integration over the phase space of the (n-m) particles not measured. In general only inclusive one- or two-particle final states are determined.

In the special case of one-particle inclusive reactions $a + b \longrightarrow c + X$, equation 4.1 simplifies to :

$$d^3\sigma = f_{ab}^c(\vec{p}; s) \frac{dp^3}{E_c} \ . \tag{4.2}$$

The UA5 detector can only detect charged particles, and, having no magnetic field, cannot measure particle momenta (apart from special cases, e.g. V^0-decays [UA5 82c]). The properties of charged interaction products are, therefore, described in terms of their angles and multiplicities. Given the good overall chamber acceptance and visual detection

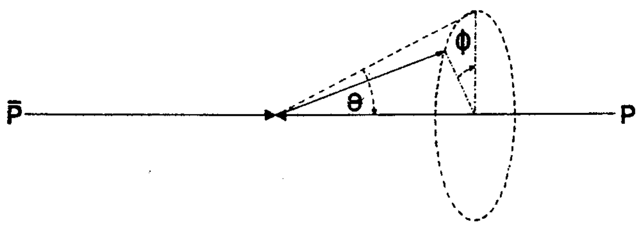

Figure IV.1: Definition of the polar and azimuthal production angles, Φ and Θ, respectively.

technique, these quantities can be determined very reliably. The definition of the c.m. azimuthal and polar production angles (Φ and Θ, respectively) are illustrated in fig. IV.1.

The polar angle Θ is usually given in terms of the pseudorapidity variable

$$\eta = -\log\ \tan(\Theta/2)\ .$$

The pseudorapidity is related to the rapidity variable

$$y = \frac{1}{2}\log\frac{E+p_L}{E-p_L} = \sinh^{-1}\frac{p_L}{\sqrt{p_T^2+m^2}}\ , \tag{4.3}$$

where E is the particle energy, p_L (p_T) its longitudinal (transverse) momentum, and m the particle mass.

When no particle momenta can be measured, the pseudorapidity η is used instead of the rapidity y; the following relation between y and η holds :

$$p_T\ \sinh\eta = \sqrt{p_T^2+m^2}\ \sinh y\ . \tag{4.4}$$

For $m^2/p_T^2 \ll 1$ one obtains $\eta \approx y$; the relation is exact for massless particles. For production at very small angles ($p_T \lesssim m \ll p_L$), i.e. $\Theta \approx 0^0$, and in the central region (small p_L and $p_T \approx m$), i.e. $\Theta \approx 90^0$ the approximation becomes worse.

Expressing the longitudinal momentum of equation 4.2 in terms of the rapidity variable, and integrating over the transverse component, one obtains the rapidity density[1]

$$\rho^{\mathrm{I}}(y) = \text{const.} \times \frac{d\sigma}{dy} \longrightarrow \frac{1}{\sigma}\cdot\frac{d\sigma}{dy}\ ,$$

which is normalized to the total cross-section. The inclusive charged particle pseudorapidity density is defined analogously :

$$\begin{aligned}\rho^{\mathrm{I}}(\eta) = &\ \frac{1}{\sigma}\cdot\frac{d\sigma}{d\eta}\\ = &\ \frac{1}{\mathrm{N}}\cdot\frac{dn(\eta)}{d\eta}\\ = &\ \frac{d\langle n(\eta)\rangle}{d\eta}\ ,\end{aligned} \tag{4.5}$$

[1]The index ($^{\mathrm{I}}$) is introduced in order to distinguish the one-particle density ρ^{I} from the two-particle density ρ^{II}, defined in section IV.3.

where N is the total number of events, and $n(\eta)$ the number of particles observed in $d\eta$ (the brackets denote the average over all events). Hence, the integral

$$\langle \mathrm{n} \rangle = \int_{-\infty}^{+\infty} \rho^{\mathrm{I}}(\eta)\, d\eta$$

is equal to the average charged particle multiplicity.

Fig. IV.2 illustrates the difference between the charged particle distributions as a function of rapidity ($\rho^{\mathrm{I}}(y)$) or pseudorapidity ($\rho^{\mathrm{I}}(\eta)$) obtained from Monte Carlo simulations (cf. section III.7). The pseudorapidity distribution underestimates the rapidity distribution

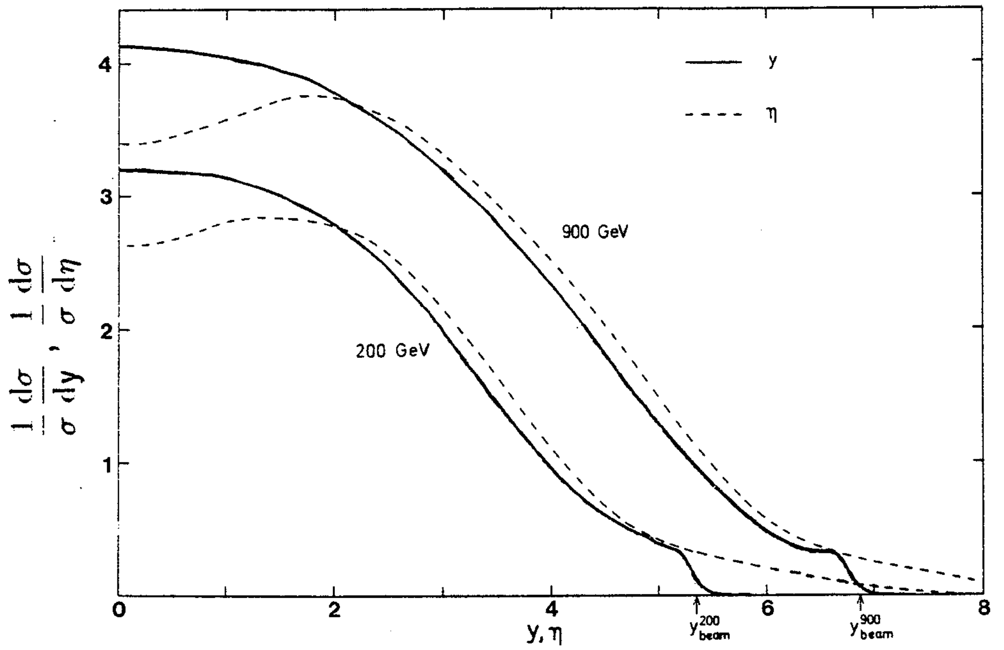

Figure IV.2: Comparison of the rapidity and the pseudorapidity distributions for 200 GeV and 900 GeV obtained with the Monte Carlo [UA5 87a].

at small values of η, y ("dip" in the central region) and overestimates it at large η, y.

For the inclusive two-body final state appropriate two-particle densities can be defined, e.g. the two-particle pseudorapidity density :

$$\rho^{\mathrm{II}}(\eta_1, \eta_2) = \frac{1}{\sigma} \cdot \frac{d^2\sigma}{d\eta_1 d\eta_2} \ . \tag{4.6}$$

It is proportional to the probability of finding a combination of two particles with pseudorapidities η_1 and η_2 in the same event. However,when counting the number of combinations, one has to distinguish between identical and non-identical particles. Here, only the pseudorapidity value (or interval) of a particle is relevant for this distinction, i.e. whether $\eta_1 = \eta_2$ or $\eta_1 \neq \eta_2$:

$$\rho^{\mathrm{II}}(\eta_1, \eta_2) = \begin{cases} \dfrac{d\langle \mathrm{n}(\eta_1)\mathrm{n}(\eta_2)\rangle}{d\eta_1 d\eta_2} & \eta_1 \neq \eta_2 \\ \dfrac{d\langle \mathrm{n}(\eta_1)\,(\mathrm{n}(\eta_1)-1)\rangle}{d\eta_1{}^2} & \eta_1 = \eta_2 \end{cases} , \tag{4.7}$$

where $n(\eta_i)$ is the number of charged particles observed in $d\eta_i$; the brackets denote the average over all events.

The integral of ρ^{II} is related to a moment of the charged particle multiplicity distribution :

$$\int_{-\infty}^{+\infty}\int_{-\infty}^{+\infty} \rho^{II}(\eta_1,\eta_2)\, d\eta_1 d\eta_2 = \langle n(n-1)\rangle \,. \tag{4.8}$$

Similarly, higher dimensional densities can be defined, though their experimental determination is seldom possible. The integral of each of these n-body particle densities determines an n^{th} moment of the multiplicity distribution. Therefore, a complete set of n-body particle densities determines all moments of the multiplicity distribution, i.e. the distribution itself, and vice versa. The integral over a limited kinematical region determines the multiplicity distribution in that region. In other words, the study of n-body particle densities is equivalent to investigations of the multiplicity distribution of those particles.

"Semi-inclusive" particle densities refer to cross-sections for the production of a fixed number n of particles in the final state; they can be correspondingly defined as, e.g.:

$$\rho_n^{I}(\eta) = \frac{1}{\sigma_n}\cdot\frac{d\sigma_n}{d\eta}\,, \tag{4.9}$$

and

$$\rho_n^{II}(\eta_1,\eta_2) = \frac{1}{\sigma_n}\cdot\frac{d^2\sigma_n}{d\eta_1 d\eta_2}\,, \tag{4.10}$$

$\ldots,$

where σ_n is the cross-section for producing n particles. The distributions are normalized as follows :

$$\int_{-\infty}^{+\infty} \rho_n^{I}(\eta)\, d\eta = n\,, \tag{4.11}$$

and

$$\int_{-\infty}^{+\infty}\int_{-\infty}^{+\infty} \rho_n^{II}(\eta_1,\eta_2)\, d\eta_1 d\eta_2 = n(n-1)\,. \tag{4.12}$$

The following sections describe, how the one- and two-particle charged pseudorapidity distributions are derived for the inclusive, as well as the "semi-inclusive" final state. Only non single-diffractive events (cf. section III.1) are taken for the analysis.

IV.2 Corrections

There are various reasons for which particle distributions have to be corrected :

- The detector does not cover the full solid angle. There are losses in the gap between the chambers at $\Phi = 0^0$ and $\Phi = \pm 180^0$. This could be easily corrected, if one assumes that the events are isotropic in azimuth. At very large rapidities ($\eta > 5$) the track angle with respect to the beam axis is so shallow, that none of the tracks enter the chamber. This cannot be corrected for directly, since no information on the forward regions ($\eta > 5$) can be gained from the data. One has to rely on the extrapolation of Monte Carlo models.

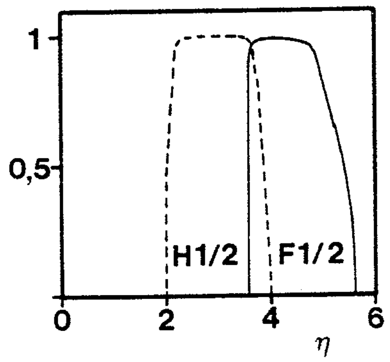

Figure IV.3: Acceptance of the trigger hodoscopes as a function of pseudorapidity.

- The hodoscopes have a limited acceptance in η, shown in fig. IV.3. Hence a few events, in particular low multiplicity ones, fail to produce a trigger.
- The primary tracks found by VFIND are contaminated with secondaries, some primaries are assigned as secondaries. Since the algorithm is tuned to balance both losses, the correction is very small.
- Very steep tracks ($\Phi \approx \pm 90^0$) are difficult to measure precisely, they appear as bright, thick tracks on film. Because of their bad RMS[2] they are usually rejected (cf. section III.4) and have to be corrected for.

All the above mentioned losses can be corrected by utilizing Monte Carlo simulation. The procedure will be discussed in detail below.

A few losses cannot be simulated, but their effect can be estimated :

- In the measuring process some tracks may be missed. One can estimate this loss by remeasuring several events. The measuring efficiency turns out to be $\epsilon_m = 0.98$ [WAR 84], only 2% of the tracks are missed fairly independent of the event multiplicity.
- Tracks inclined at shallow angles to the beam pipe (i.e. having large η) have a high probability of producing a secondary shower in the beam pipe or chamber bottom. The secondaries entering the chamber and are visible on film as very dense showers. In some cases they obscure part of the film, making that region unmeasurable. Two tracks bounding the region are measured and labeled specially (Q-label). One can afterwards estimate the area lost in terms of pseudorapidity and treat it like a loss in geometrical efficiency [MAG 82a]. Fig. IV.4 shows the efficiency loss ϵ_Q as a function of pseudorapidity for three multiplicity regions. Only for multiplicities above 40 and $\eta > 4.5$ are the losses comparable to measurement losses and can in general be neglected.[3]

The data are corrected by using the following algorithm shown in fig. IV.5 :

[2]Deviation of a track from a straight line.

[3]This was not the case for the 1981 data [MUE 83] where corrections tended to be a factor of 7 larger. The steel beam pipe was the source of abundant electromagnetic showers.

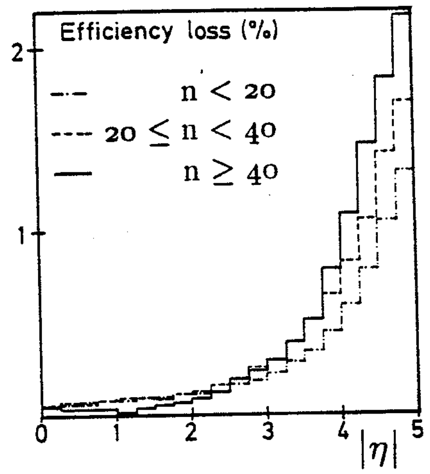

Figure IV.4: Q-lable losses for different multiplicity regions as a function of pseudorapidity.

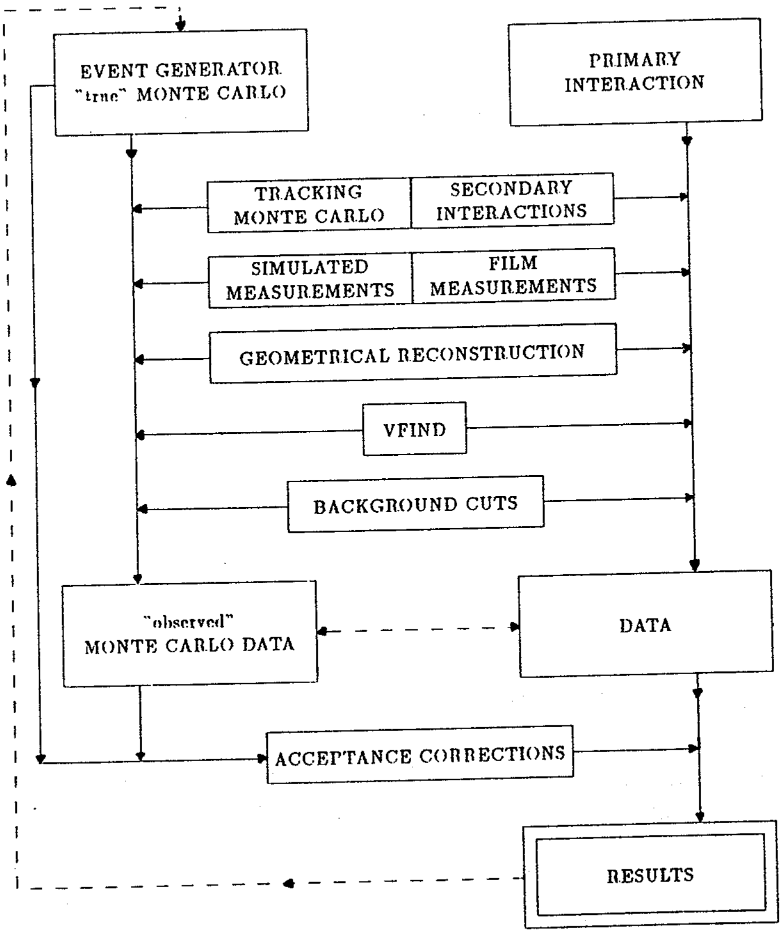

Figure IV.5: Illustration of the correction procedure.

$\sqrt{s}$	ϵ_t
200 GeV	$(91.5 \pm 2.0)\%$
546 GeV	$(96.6 \pm 1.6)\%$
900 GeV	$(97.0 \pm 1.7)\%$

Table IV.1: The trigger efficiency as a function of energy.

The primary interaction is generated by the UA5 event generator [WEI 82,UA5 87a] (described in section III.7). This program is tuned to describe the features of p$\bar{\text{p}}$-interactions at 200, 546, and 900 GeV phenomenologically. Since many of the particles created in the primary interaction undergo secondary interactions (scattering, showers, decays, etc.) in the detector material, the event generator data have to be treated correspondingly. This is done in the UA5 Monte Carlo [WEI 82,UA5 87a] (section III.7), where each primary particle produced is tracked through an appropriate simulation of the detector material. Finally, the distortions introduced by the optics system and the measurement process are generated. In this stage the Monte Carlo data should correspond to real data after the geometrical reconstruction. The vertex finding procedure is then applied to the simulated data, and "background" events are rejected with the same cuts that were applied to the data. At this stage, one can either compare the "observed" Monte Carlo data to the real data, or derive geometrical, vertex-finding, and trigger efficiencies by comparing the "observed" Monte Carlo with the original event generator. These efficiencies are used to correct the data which, in turn, is used to tune the eventgenerator. As long as the corrections are small, the procedure should converge. In total a sample of about 30 000 Monte Carlo events was available at each energy.

In order to correct the observed pseudorapidity distribution, for example, one does the following :

The correction factor is determined by calculating the ratio of the event generator distribution (EV) to the Monte Carlo distribution (MC) :

$$\frac{\rho^{\mathrm{I}}{}_{\mathrm{EV}}(\eta)}{\rho^{\mathrm{I}}{}_{\mathrm{MC}}(\eta)} \times \frac{1}{\epsilon_m} = \underbrace{\frac{\mathrm{N_{MC}}}{\mathrm{N_{EV}}}}_{\epsilon_t} \cdot \underbrace{\frac{dn_{\mathrm{EV}}/d\eta}{dn_{\mathrm{MC}}/d\eta} \times \frac{1}{\epsilon_m}}_{1/\epsilon^{\mathrm{I}}_{\mathrm{acc}}(\eta)},$$

where $\epsilon^{\mathrm{I}}_{\mathrm{acc}}(\eta)$ is dominated by the geometrical efficiency, and also contains effects such as bad angle measurements, losses caused by the primary-secondary assignment, and the measurement efficiency. ϵ_t contains the trigger efficiency, losses due to background cuts, and corrections for events where no primary vertex was found.

The trigger efficiency is given in table IV.1, the errors reflect the statistical uncertainties only. The value derived is sensitive to the average transverse momentum, and to the shape of the x_F-distribution[4] for leading baryons near $x_F \approx 1$. The Monte Carlo assumes a $1 - |x_F|$ distribution near $|x_F| \approx 1$. If, instead, the leading baryon distribution were to be flat in x_F, the overall trigger efficiency would decrease by about 2% [UA5 87c].

[4] $x_F = 2 \cdot p_L/\sqrt{s}$

The rapidity dependent correction ϵ^{I}_{acc} is shown in fig. IV.7(a). For pseudorapidity values $|\eta| < 2.5$ the geometrical efficiency is greater than 90%. The systematic errors are small ($\approx$ 2%), they depend essentially on the quality of the simulation of secondary interactions in the chamber material.

The correction procedure applied to the data is only valid statistically, i.e. for distributions that average over a certain sample of events. It cannot be applied on an event-to-event basis. Distributions of individual events or a very small event sample cannot be corrected for losses. However, they can be compared directly to Monte Carlo distributions (after the vertex finding procedure). This problem arises in the analysis of fluctuations in the pseudorapidity distributions for individual events (cf. chapter VI).

IV.3 Corrected Charged Particle Pseudorapidity Distribution

A definition of the pseudorapidity distribution was already given in equation 4.5. The raw distribution has to be corrected following the procedure described in section IV.2.

$$\rho^{I}(\eta) = \frac{1}{\epsilon^{I}_{acc}(\eta)} \times \epsilon_t \times \rho^{I}{}_{obs}(\eta)\ , \tag{4.13}$$

where the index "*obs*" refers to the raw, uncorrected distribution.

Fig. IV.6 shows the corrected charged particle pseudorapidity distribution. Since η is

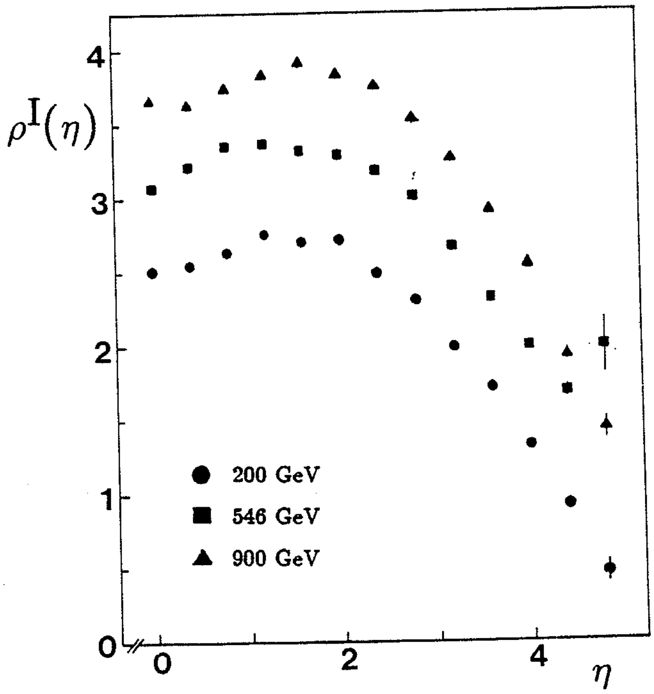

Figure IV.6: Charged particle pseudorapidity distribution.

measured in the c.m. system, the distribution is expected to be symmetric around $\eta = 0$ from the charge conjugation symmetry of the final state. Therefore, the distribution is shown folded around $\eta = 0$. The errors shown are statistical only, the origin of the systematic errors was discussed above and would change the overall normalization by about

$\sqrt{s}$	central density	$\langle n \rangle\|_{\|\eta\|<5}$
200 GeV	2.51 ± 0.04	20.66 ± 0.05
546 GeV	3.08 ± 0.04	28.02 ± 0.04
900 GeV	3.68 ± 0.05	32.20 ± 0.05

Table IV.2: Central density and integral of the charged particle pseudorapidity distribution as a function of c.m. energy.

2-3%. The depletion in the central region ($\eta \lesssim 1$) is of kinematic origin, as explained in section IV.1.

The distribution $\rho^{\mathrm{I}}(\eta)$ increases both in width and in height with increasing energy. The broadening is proportional to log s, since the available rapidity range increases as $y_{beam} = \log \sqrt{s}/m_p$, where m_p is the proton mass. Table IV.2 shows the central density[5]

$$\rho^{\mathrm{I}}(\eta \approx 0) = \int_{-0.2}^{+0.2} \rho^{\mathrm{I}}(\eta)\, d\eta \ ,$$

as well as the integral of the distribution

$$\langle n \rangle|_{|\eta|<5} = \int_{-5}^{+5} \rho^{\mathrm{I}}(\eta)\, d\eta \ ,$$

which gives the average charged multiplicity in that region.

It was found in a comparison with lower energy data [UA5 85c], that the central density rises linearly with log s.[6]

The raw two-particle pseudorapidity distribution is corrected similarly to the one-particle distribution by calculating a geometrical acceptance $\epsilon^{\mathrm{II}}_{acc}(\eta_1, \eta_2)$ from the two-particle distribution obtained from the Monte Carlo data. Often this acceptance is assumed to factorize [EGG 75b] :

$$\frac{\epsilon^{\mathrm{II}}_{acc}(\eta_1, \eta_2)}{\epsilon^{\mathrm{I}}_{acc}(\eta_1) \cdot \epsilon^{\mathrm{I}}_{acc}(\eta_2)} \approx 1 \ . \tag{4.14}$$

This assumption holds reasonably well for $\eta_1 \neq \eta_2$, it is not correct for $\eta_1 = \eta_2$, as shown in fig. IV.7(b); mainly because we cannot directly distinguish primary and secondary tracks in a given event, but have to use an algorithm (VFIND) to separate them (cf. section III.5).

The corrected charged particle pseudorapidity density ρ^{II} at $\sqrt{s} = 900$ GeV is given in fig. IV.8. It shows a similar dip as the one-particle density.

[5] Note, that the value obtained for the central density depends on the integration interval because of the dip of the pseudorapidity distribution in the center. For practical reasons the interval $|\eta| \leq 0.2$ was chosen here; qualitatively this choice does not influence the energy dependence of the central density.

[6] Since most of the low energy data published refers to the total inelastic cross-section (i.e. the combination of single-diffraction and non single-diffraction), one has to compare the inelastic distributions not given here [UA5 85c].

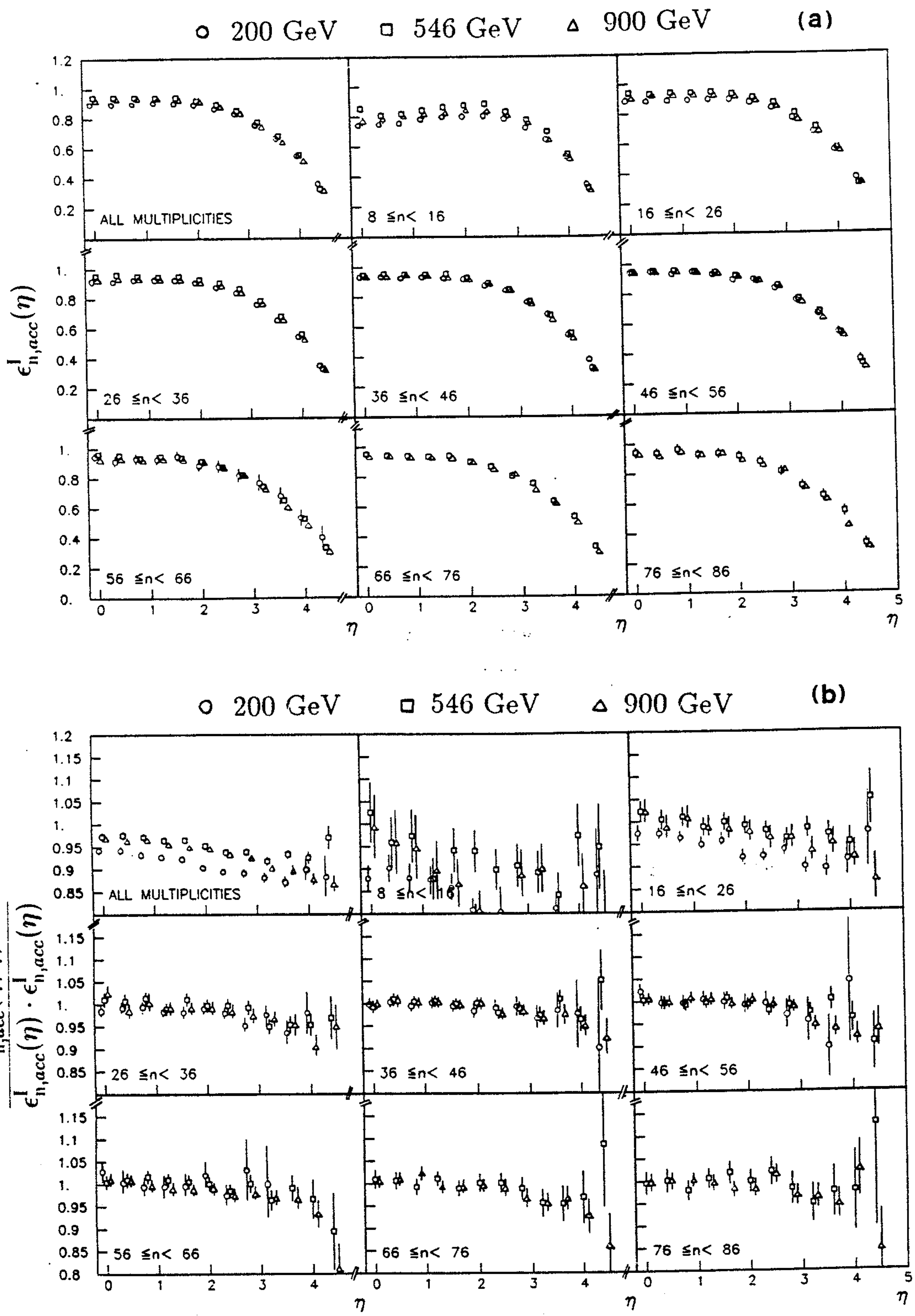

Figure IV.7: (a) One-particle geometrical acceptance, ϵ^{I}_{acc} and $\epsilon^{I}_{n,acc}$, as a function of η for all multiplicities combined and for fixed intervals of multiplicity. (b) Ratio of the two-particle and one-particle geometrical acceptances, ϵ^{II}_{acc} and $\epsilon^{II}_{n,acc}$, for all multiplicities combined and for fixed intervals of multiplicity.

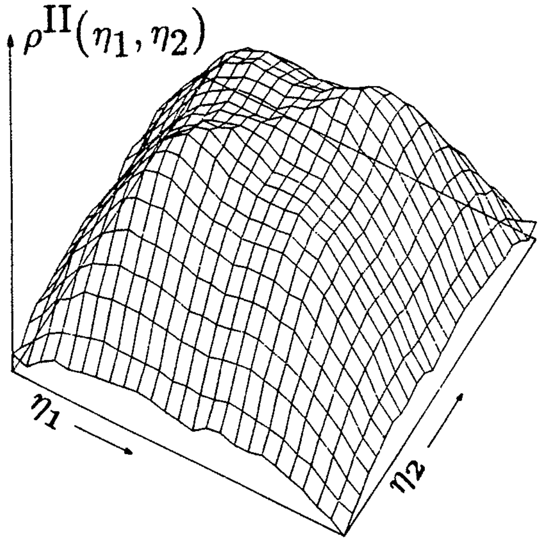

Figure IV.8: Two-particle charged pseudorapidity density at $\sqrt{s} = 900$ GeV.

From ρ^{II} one can extract information about the two-particle correlations; this is done in the following chapter. Information on more than two-body final states [KAF 77,EGG 75b] cannot be obtained in this experiment due to lack of statistics.

IV.4 Semi-Inclusive Charged Particle Pseudorapidity Densities

Corrections of the observed pseudorapidity densities at fixed charged multiplicity n are carried out similarly to those described in the previous section.

The trigger efficiency $\epsilon_{n,t}$, and the geometrical efficiencies $\epsilon^{I}_{n,acc}(\eta)$ and $\epsilon^{II}_{n,acc}(\eta_1, \eta_2)$ are obtained from the ratios of the event generator distributions and the Monte Carlo distributions (cf. equation 4.13) taken at fixed true charged multiplicity n. They are shown in figs. IV.7 and IV.9. The efficiencies are subject to the same systematic uncertainties as discussed in section IV.2.

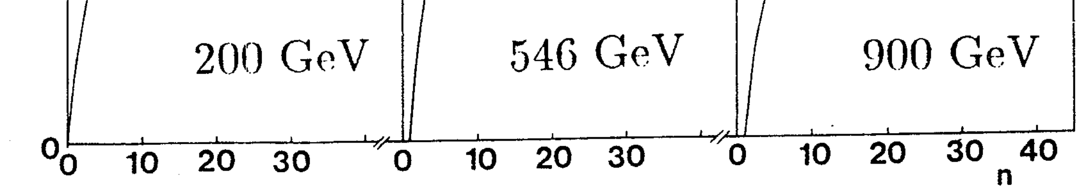

Figure IV.9: Trigger efficiency as a function of charged multiplicity.

For small multiplicities (n$\lesssim$20) the trigger efficiency drops to very low values, since the probability, that a particle hits one of the trigger hodoscopes, depends on the total number of particles produced in that event. Because of the broadening of the rapidity distribution with increasing c.m. energy, the chance of a particle producing a trigger increases with energy at fixed multiplicity.

The significant difference between the calculation of inclusive and semi-inclusive densities lies in the fact that one does not know the true multiplicity n of a given event (not all of the charged particles are determined), but has to infer it from the multiplicity n_{obs} actually observed in the detector. The Monte Carlo data gives access to the information of how, for an event of given true multiplicity n, the multiplicities n_{obs} observed in the detector are distributed; this is shown in fig. IV.10. In principle, one could use this distribution

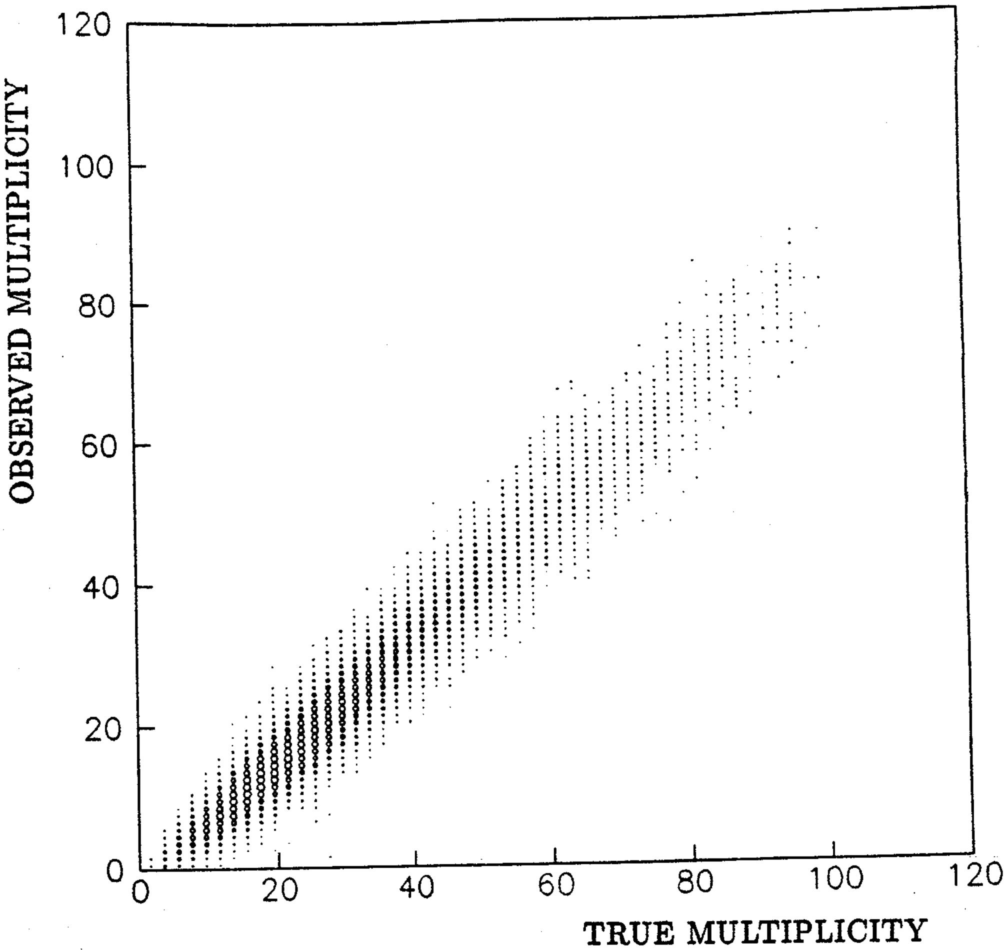

Figure IV.10: Distribution of observed and true multiplicities in the Monte Carlo data at $\sqrt{s} = 546$ GeV.

to determine the true multiplicities for the data; but this requires too large an amount of Monte Carlo data, so one has to rely on additional assumptions on the shape of this distribution. The probability $P(n_{obs}, n)$ for observing n_{obs} particles in the chamber, given a true multiplicity n, can be taken to follow a binomial distribution

$$P(n_{obs}, n) = \binom{n}{n_{obs}} p^{n_{obs}}(1-p)^{n-n_{obs}} ,$$

$\sqrt{s}$	a	b	c
fit to $\langle n_{obs}\rangle\vert_n = a + b\cdot n + c\cdot n^2$			
200	-0.92 ± 0.05	0.816 ± 0.005	$(1.41 \pm 0.10) \times 10^{-3}$
546	-1.33 ± 0.05	0.759 ± 0.004	$(1.19 \pm 0.06) \times 10^{-3}$
900	-1.84 ± 0.06	0.732 ± 0.005	$(0.93 \pm 0.05) \times 10^{-3}$
fit to $\sigma^2(n_{obs})\vert_n = a + b\cdot n^c$			
200	-0.8 ± 0.2	0.9 ± 0.1	0.69 ± 0.03
546	-2.0 ± 0.3	1.4 ± 0.2	0.65 ± 0.02
900	-3.3 ± 0.4	1.8 ± 0.2	0.65 ± 0.02

Table IV.3: Parametrization of the first two moments of the $P(n_{obs}, n)$ distribution.

if the losses are only due to the geometrical efficiency. Since secondary particles can be confused with primaries, the probability distribution can have finite values for $n_{obs} > n$ and has to be slightly modified [GAU 84,HOL 86] :

$$\begin{aligned} P(n_{obs}, n) &= \binom{n+k}{n_{obs}} p^{n_{obs}}(1-p)^{n+k-n_{obs}} \\ \text{with } n+k &= \frac{(\langle n_{obs}\rangle|_n)^2}{\langle n_{obs}\rangle|_n - \sigma^2(n_{obs})|_n} . \end{aligned}$$

The moments $\langle n_{obs}\rangle|_n$ and $\sigma^2(n_{obs})|_n$ are the average and the variance, respectively, of the distribution IV.10 at fixed n; they are shown in fig. IV.11 together with a least squares fit to the following parametrization :

$$\begin{aligned} \langle n_{obs}\rangle\Big|_n &= a_1 + b_1\cdot n + c_1\cdot n^2 \\ \sigma^2(n_{obs})\Big|_n &= a_2 + b_2\cdot n^{c_2} . \end{aligned}$$

Table IV.3 gives the parameter values for 200, 546, and 900 GeV.

One can then use this to determine the probability matrix that an event of observed charged multiplicity n_{obs} comes from a true multiplicity n, and hence the multiplicity distribution. How this probability matrix is determined, is described in [HOL 86,ASM 85]. Instead, for each event of observed multiplicity n_{obs} a "true" multiplicity n is randomly chosen according to the probability distribution $P(n_{obs}, n)$ at fixed values of n_{obs}, and the appropriate particle densities are calculated as a function of this assigned multiplicity n.[7]

The corrected semi-inclusive charged particle pseudorapidity densities are shown for various ranges of charged multiplicity in fig. IV.12. The density increases with multiplicity, this is due, though, to the overall normalization (equation 4.12). If one compares the densities, ρ_n^I/n, normalized to unity (fig. IV.13), it is evident that for higher multiplicities the distributions become narrower and increase in height only in the central region. The central density

$$\rho_n^I(\eta \approx 0) = \int_{-0.2}^{+0.2} \rho_n^I(\eta)\, d\eta ,$$

[7]This simplified procedure is valid for calculating averages over the multiplicity distribution (e.g. rapidity density distributions), and has the advantage of avoiding normalization problems when one determines higher order density distributions.

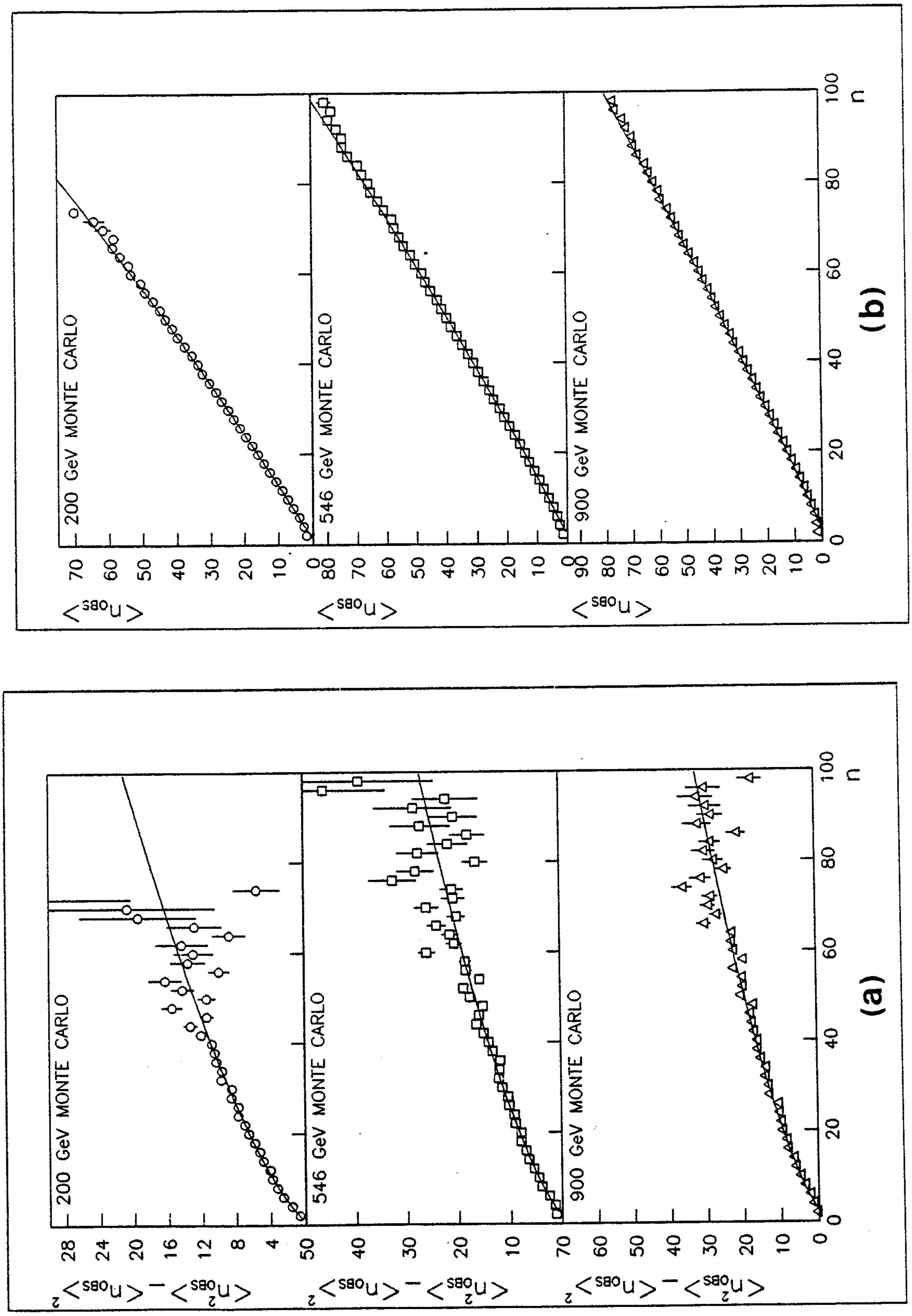

Figure IV.11: The average (a) and the variance (b) of the observed multiplicity as a function of true multiplicity in the Monte Carlo. The curve shows the parametrization given in table IV.3.

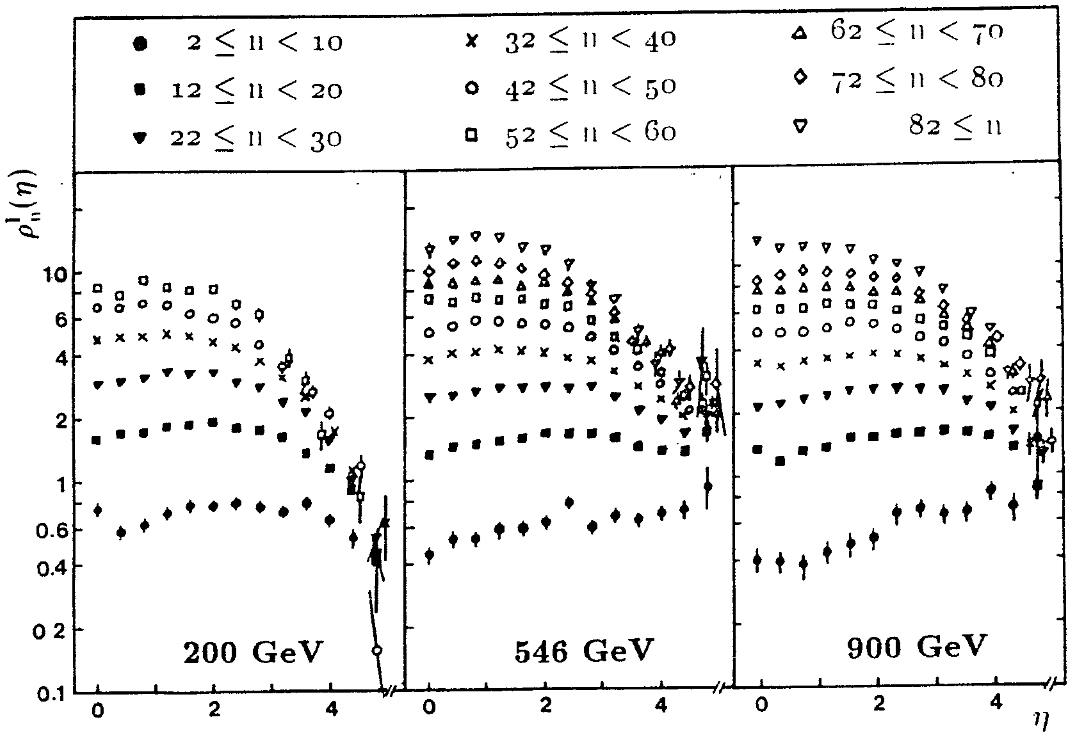

Figure IV.12: Semi-inclusive pseudorapidity density for various ranges of charged multiplicity.

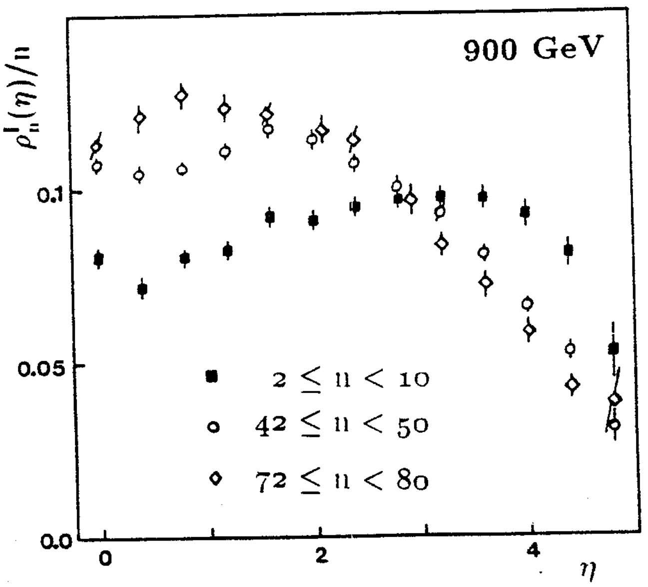

Figure IV.13: Normalized semi-inclusive pseudorapidity density for different ranges of charged multiplicity.

therefore, shows a stronger than linear increase with multiplicity (fig. IV.14). At fixed

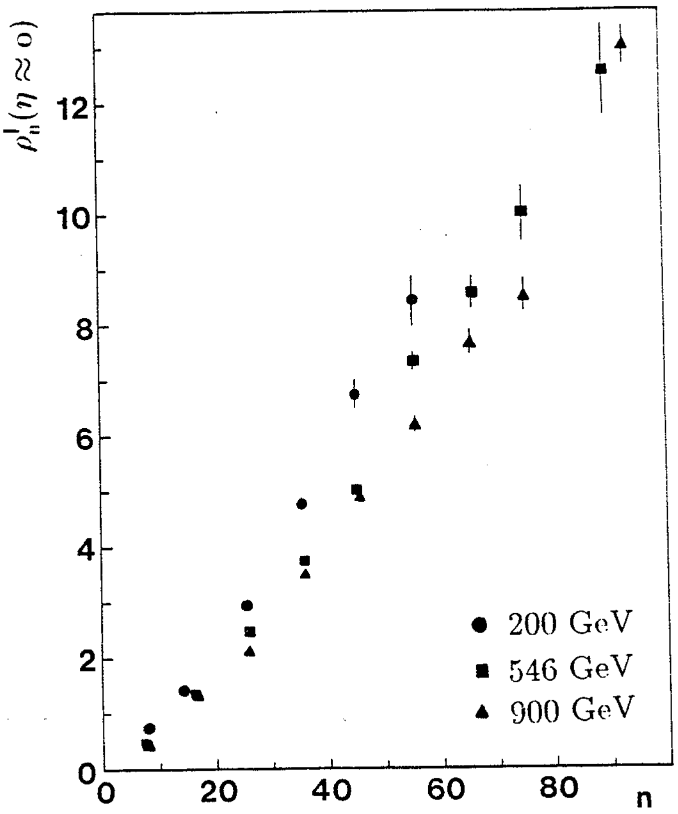

Figure IV.14: Central pseudorapidity density as a function of multiplicity and c.m. energy.

multiplicity n, though, the central density decreases with the c.m. energy and the distributions become broader. Furthermore, it was found [UA5 86d] that the scaled central density $\rho^{I}_{n}(0)/\rho^{I}(0)$ expressed as a function of $z = n/\langle n\rangle$ is independent of s.

Higher order semi-inclusive rapidity densities are not given in this chapter. They are very closely connected to the many-particle correlations in rapidity space, and will be discussed in chapter V.

Chapter V

Two-Particle Pseudorapidity Correlations

V.1 Introduction

In order to understand the dynamics of multi-particle production in high energy collisions, analyses of single-particle distributions alone are insufficient. Investigations of correlations among final state particles are necessary in order to reveal further properties of the underlying production mechanism.

These studies involve the interaction

$$\mathrm{p}\bar{\mathrm{p}} \longrightarrow c_1 + c_2 + \mathrm{X} \ ,$$

where c_1, c_2 are the particles observed, and the rest of the produced particles contained in "X" are either disregarded, or only specific features, such as the number of charged particles, are noted. The correlations between c_1 and c_2 can be investigated in terms of their kinematic variables, e.g. rapidity, azimuth, and transverse momentum; as well as in terms of the types of particles observed, e.g. charge, quantum numbers etc. The conservation of energy and momentum produces trivial correlations among the final state particles; they can be removed, for example, by restricting the analysis to certain regions of phase space.

One of the most accessible sources of information on particle correlations is the study of two-body (pseudo-)rapidity correlations. They can be separated into two types :

- Observing a particle in a certain region of phase space may give information on what can be expected in adjacent regions; these correlations are termed "short-range".
- On the other hand, the observation of a particle can yield information on the particles produced in other regions further away or on the event as a whole. This is a "long-range" effect.

First studies of correlations among final state particles emitted at various positions in rapidity had been undertaken already at c.m. energies of 5 GeV [KO 72]. More extensive analyses were made in pp-collisions at the FNAL ($\sqrt{s}$ up to 27 GeV) [KAF 77], and at the CERN ISR ($\sqrt{s}$ up to 63 GeV) in pp, p$\bar{\mathrm{p}}$, αp, and $\alpha\alpha$ collisions [EGG 75b,AME 76,DRI 79,BEL 84], as well as in e^+e^--collisions [KOC 82].

They have revealed a tendency for particles in the central region to be grouped in clusters over a range of rapidity of about 1 to 2 units. These "short-range" correlations have been interpreted in terms of cluster models [MOD] in which the observed hadrons are products of isotropic cluster decays with an average decay multiplicity of about 2 charged particles per cluster. The increased number of final state particles and the large range of about 6 units of the pseudorapidity plateau available at Collider energies should provide an even better basis for the study of rapidity correlations and the separation of short-range and long-range effects.

V.2 Inclusive Two-Particle Pseudorapidity Correlations

The charged particle pseudorapidity densities ρ^{I} and ρ^{II} were determined in the previous chapter. In terms of these quantities one can define the two-body correlation function [WIL 70,MUE 71] :

$$C(\eta_1, \eta_2) = \rho^{\mathrm{II}}(\eta_1, \eta_2) - \rho^{\mathrm{I}}(\eta_1) \cdot \rho^{\mathrm{I}}(\eta_2) . \tag{5.1}$$

It determines, whether the probability for the joint production of a pair of particles at η_1 and η_2 (in the same event), given by $\rho^{\mathrm{II}}(\eta_1, \eta_2)/\langle n(n-1)\rangle$, differs from the probability for independent production, $\rho^{\mathrm{I}}(\eta_1)\rho^{\mathrm{I}}(\eta_2)/\langle n\rangle^2$, of two particles with the same pair of pseudorapidity values. The integral of the correlation function is given by :

$$\begin{aligned}
\int_{-\infty}^{+\infty}\int_{-\infty}^{+\infty} C(\eta_1, \eta_2)\, d\eta_1 d\eta_2 &= \int_{-\infty}^{+\infty}\int_{-\infty}^{+\infty} (\rho^{\mathrm{II}}(\eta_1, \eta_2) - \rho^{\mathrm{I}}(\eta_1) \cdot \rho^{\mathrm{I}}(\eta_2))\, d\eta_1 d\eta_2 \\
&= \langle n(n-1)\rangle - \langle n\rangle^2 \\
&= f_2 ,
\end{aligned} \tag{5.2}$$

where f_2 is the second Mueller moment of the multiplicity distribution, which is connected to the width of the multiplicity distribution. In the case of independent particle production the f_2-moment and all higher f-moments would vanish [KNO 74]; the multiplicity distribution would become a Poisson distribution. This is clearly not the case, though; the width of the charged particle multiplicity distribution and the f_2-moment show a sharp increase with energy [THO 77,UA5 84](cf. fig. V.1).

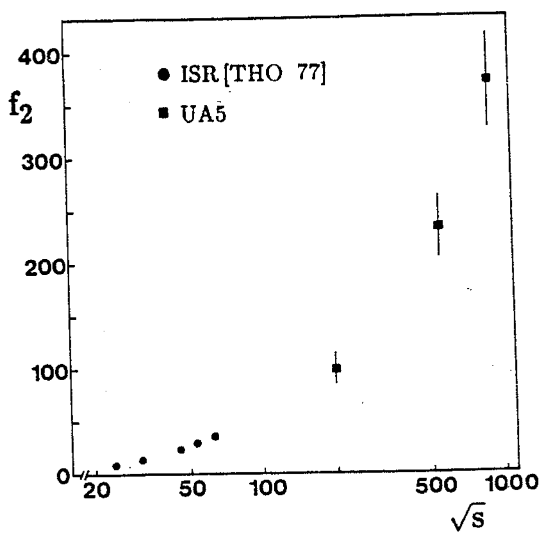

Figure V.1: The f_2-moment for ISR-energies [THO 77] and Collider energies [UA5 84,UA5 86a].

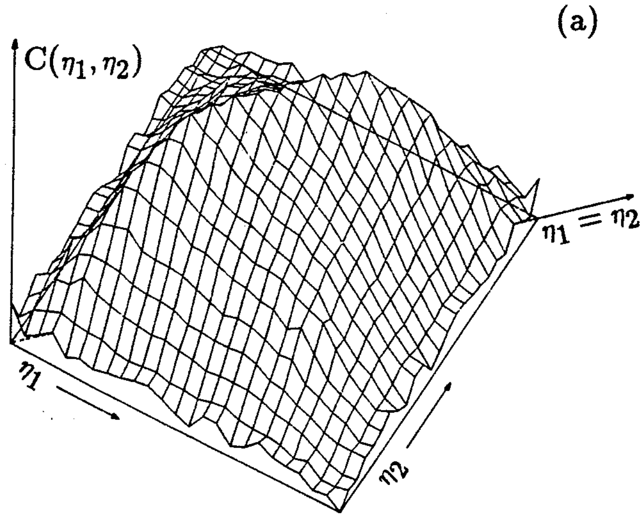

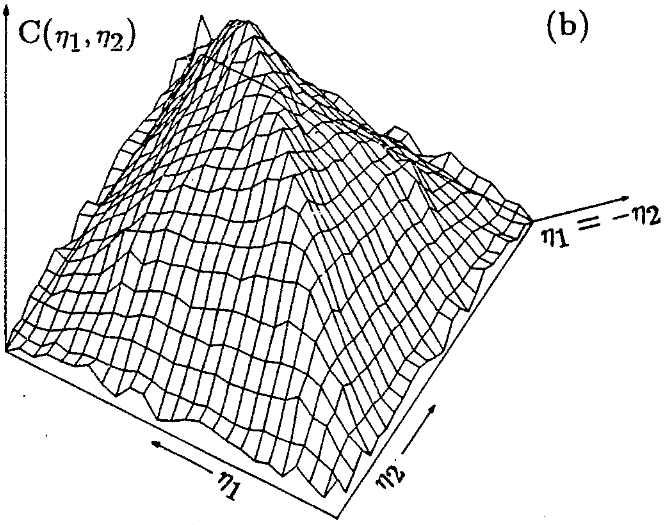

Figure V.2: The inclusive two-particle correlation function $C(\eta_1, \eta_2)$ projected to illustrate the dependence on (a) $\eta_1 + \eta_2$ and (b) $\eta_1 - \eta_2$.

The inclusive correlation function is given in fig. V.2 for $\sqrt{s} = 900$ GeV. Rather than illustrating the η_1, η_2 dependence, the correlation function is projected to give a better view of the dependence on $\eta_1 + \eta_2$ and $\eta_1 - \eta_2$. In (a) the behavior for $\eta_1 - \eta_2 =$ const., e.g. along the diagonal $\eta_1 = \eta_2$ is illustrated. In the central region it is independent of $\eta_1 + \eta_2$. (b) shows the same plot rotated by 90^0 to demonstrate the dependence on $\eta_1 - \eta_2$ (e.g. along the diagonal $\eta_1 = -\eta_2$). A sharp rise in the central region can be made out. In other words, observing a particle in a given region of phase space makes it more likely that a second particle is produced nearby. This confirms the observations made at lower energies [KAF 77], that the shape of the correlation function in the central region depends only on the (pseudo-)rapidity difference $|\eta_1 - \eta_2|$ ("translational invariance"), and has its maximum value at $\eta_1 = \eta_2 \approx 0$.

The normalized correlation function

$$\begin{aligned} R(\eta_1, \eta_2) &= \frac{C(\eta_1, \eta_2)}{\rho^{I}(\eta_1)\rho^{I}(\eta_2)} \\ &= \frac{\rho^{II}(\eta_1, \eta_2)}{\rho^{I}(\eta_1)\rho^{I}(\eta_2)} - 1 \end{aligned} \tag{5.3}$$

is introduced to avoid difficulties with cross-section normalizations and to cancel out uncertainties in the acceptance correction [AME 74]. In section IV.3 the corrections of the geometrical efficiencies ϵ^{I}_{acc} and ϵ^{II}_{acc} were discussed with the result, that the efficiency ratio $\epsilon^{II}_{acc}/(\epsilon^{I}_{acc} \times \epsilon^{I}_{acc})$—this ratio corrects the normalized correlation function R—can not be taken as unity for all regions of pseudorapidity. Therefore, the R-function offers no advantages over the C-function for this experiment. Furthermore, the properties of the C-function stated above are not so well reproduced by the ratio R, as can be seen from fig. V.3. The dependence on $|\eta_1 - \eta_2|$ is less pronounced, and the plateau at $\eta_1 = \eta_2$ is not

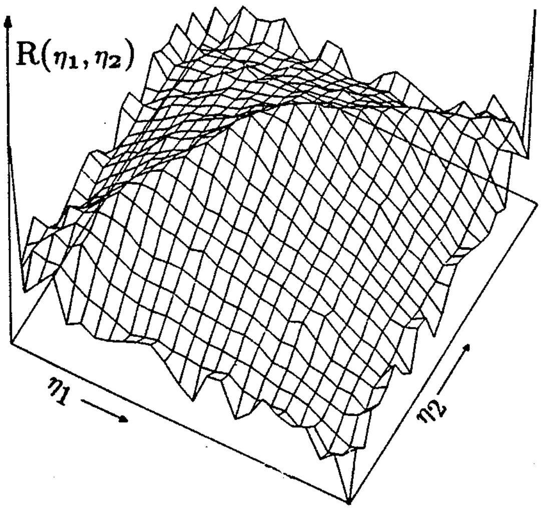

Figure V.3: The normalized inclusive correlation function $R(\eta_1, \eta_2)$.

as flat. For these reasons only the correlation function $C(\eta_1, \eta_2)$ is taken for the following analysis.

The inclusive two-particle correlation function $C(\eta_1, \eta_2)$ at fixed $\eta_2 = 0$ is presented in fig. V.4(a) for 200, 546, and 900 GeV. It shows a striking increase in height and width compared to results obtained at lower energies ($\sqrt{s} = 63$ GeV) [AME 76,FOA 75]. This

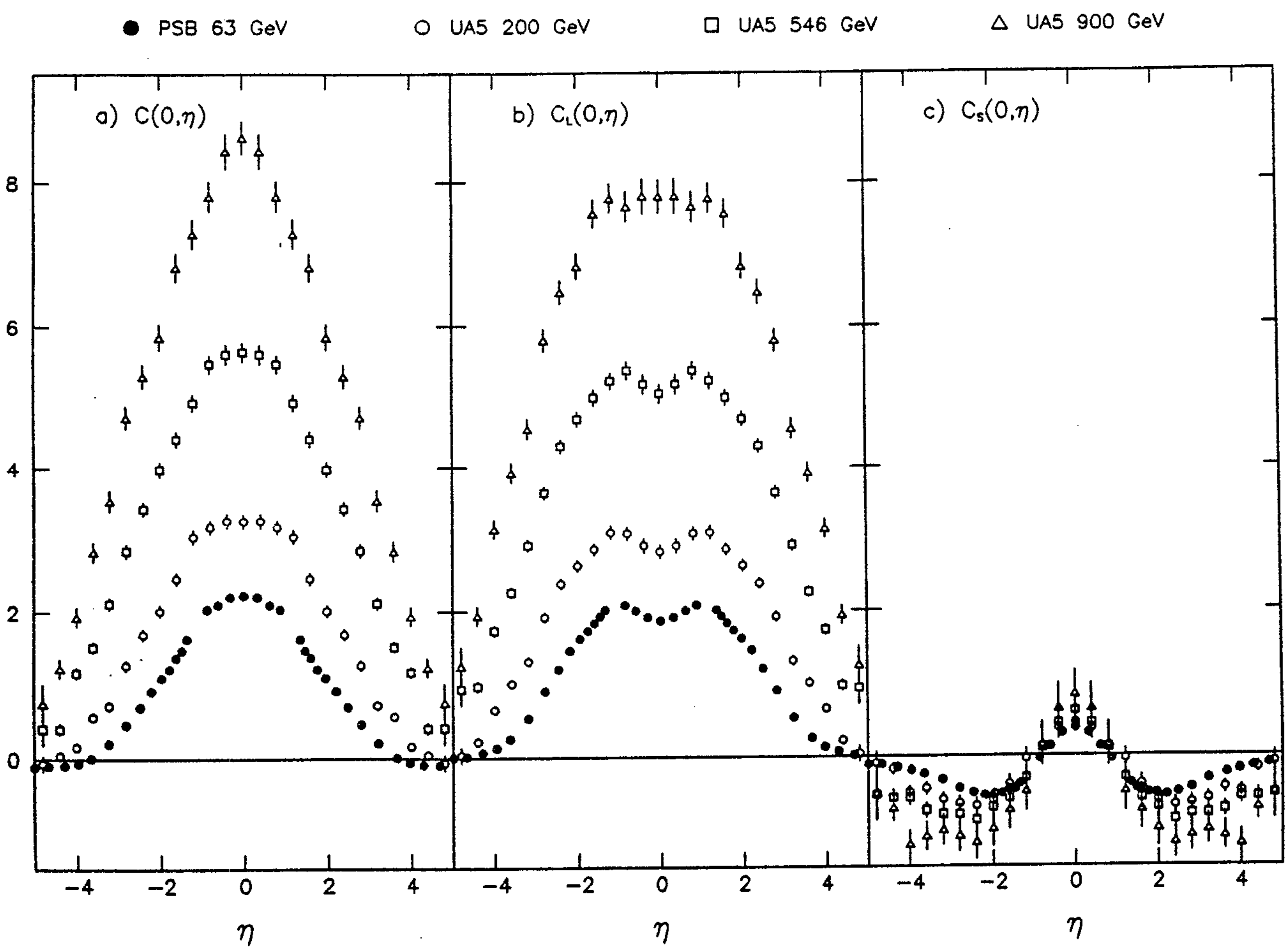

Figure V.4: The inclusive correlation function $C(\eta_1, \eta_2)$ (a) is plotted for fixed $\eta_1 = 0$ versus η_2 at 63 GeV [AME 76,FOA 75], 200, 546, and 900 GeV. (b) shows the long-range and (c) the short-range contribution to $C(\eta_1, \eta_2)$.

is to be expected since the f_2-moment has increased significantly from lower energies [UA5 84,UA5 86a]. The errors shown are only statistical. They take into account the fact that the single and two-particle densities are not statistically independent quantities and can be calculated from higher order densities [KEN 73].

V.3 Semi-Inclusive Two-Particle Pseudorapidity Correlations

Apparent correlations can be generated by adding two uncorrelated mechanisms together. This was first discussed in the framework of two-component models [PIR 73,BER 73b], where the inclusive correlation function is expressed in terms of the intrinsic correlations inside each component, and a cross term arising from the mixing of components. In analogy, mixing events with different charged multiplicities, which have different single particle densities (cf. section IV.4), can cause strong apparent correlations. Therefore, the inclusive correlation function C has to be decomposed into a semi-inclusive component (correlations of events with a given multiplicity n), C_S, and a mixing term (events with different multiplicities n), C_L. Therefore, the inclusive correlation function C is related to the semi-inclusive function C_n at fixed charged multiplicity n as [BIA 73,KAF 77] :

$$C(\eta_1,\eta_2) = C_S(\eta_1,\eta_2) + C_L(\eta_1,\eta_2)\,, \tag{5.4}$$

where

$$C_S(\eta_1,\eta_2) = \sum_n \frac{\sigma_n}{\sigma} C_n(\eta_1,\eta_2) \tag{5.5}$$

and

$$C_L(\eta_1,\eta_2) = \sum_n \frac{\sigma_n}{\sigma} \left(\rho^I(\eta_1) - \rho^I_n(\eta_1)\right) \cdot \left(\rho^I(\eta_2) - \rho^I_n(\eta_2)\right)\,. \tag{5.6}$$

Fig. V.4(b) shows the contribution of $C_L(\eta_1,\eta_2)$ and fig. V.4(c) the contribution of $C_S(\eta_1,\eta_2)$ to the inclusive correlation function for $\eta = 0$.

The first term in equation 5.4 is the semi-inclusive correlation function $C_n(\eta_1,\eta_2)$ averaged over all multiplicities. For fixed charged multiplicity n it is defined in analogy to equation 5.1 as :

$$C_n(\eta_1,\eta_2) = \rho^{II}_n(\eta_1,\eta_2) - \rho^I_n(\eta_1)\cdot\rho^I_n(\eta_2)\,,$$

with the following normalization :

$$\int_{-\infty}^{+\infty}\int_{-\infty}^{+\infty} C_n(\eta_1,\eta_2)\,d\eta_1 d\eta_2 = -n\,.$$

As shown in fig. V.4(c) and also fig. V.5, $C_S(\eta_1,\eta_2)$ is sharply peaked with a full width of about two units in pseudorapidity and is, therefore, called a "short-range" correlation function. This peak structure, again, depends only on the (pseudo-)rapidity difference $|\eta_1 - \eta_2|$; for $\eta_1 = \eta_2$, C_S is nearly constant in the central region. It is almost energy independent, the strong increase with energy seen in the inclusive correlation function C has nearly disappeared.

The second term in equation 5.4 includes such effects as the different normalizations of the semi-inclusive pseudorapidity densities (cf. equation 4.12), and the change in shape of ρ^I_n with multiplicity (fig. IV.13). It is present even in the absence of true dynamical correlations. It broadens the correlation function and is, therefore, somewhat misleadingly called "long-range" correlation. The comparison of different energies shown in fig. V.4(b) demonstrates how this term is responsible for the apparent increase of the inclusive correlation function $C(\eta_1,\eta_2)$ with energy. This illustrates the importance of the decomposition, since a large value for the inclusive correlation function C does not necessarily imply that the intrinsic correlations are strong as well. Fig. V.6 shows the broad plateau of C_L. For $\eta_1 = \eta_2$ one expects C_L to be constant in the central region, as are C and C_S. Trivially,

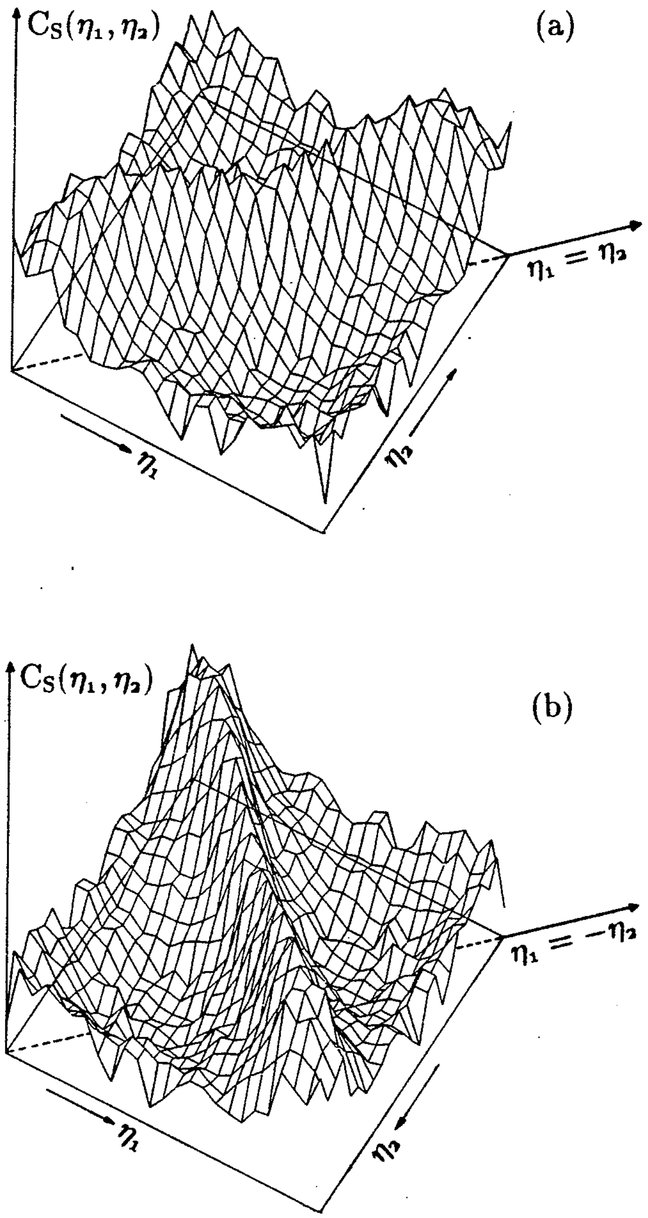

Figure V.5: Short-range contribution to the inclusive two-particle correlation function $C_S(\eta_1, \eta_2)$ projected to show the dependence on (a) $\eta_1 + \eta_2$ and (b) $\eta_1 - \eta_2$.

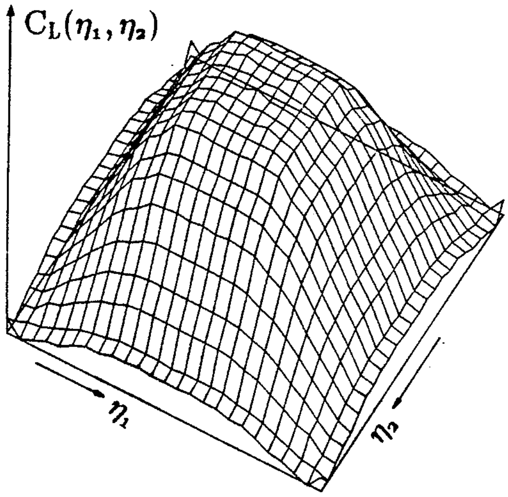

Figure V.6: Long-range contribution to the inclusive two-particle correlation function $C_L(\eta_1, \eta_2)$.

this also holds for $\eta_1 = -\eta_2$ because the symmetry of the pseudorapidity distribution, $\rho^I(\eta) = \rho^I(-\eta)$, implies $C_L(\eta, \eta) = C_L(\eta, -\eta)$.

If a mixture of different event types (e.g. single-diffractive and non-single-diffractive) is present in the data, an additional "long-range" term similar to that in the above relation would appear. A Monte Carlo study has shown that the possible contamination from single-diffractive events is small, e.g. for the 900 GeV data $\simeq 2\%$ [UA5 86e]. This should affect only low multiplicities and might show up in the correlation function C_n at small values of n. There is arguably a further separate contribution from a double diffractive component, but this is likely to be small [UA5 86e].

It follows from equation 5.6 that for the correlation function C_n at fixed multiplicity the corresponding "long-range" or mixing term is obviously not present. This is not strictly true if C_n is calculated over a small but finite range of multiplicities. The "long-range" contribution, though, was found to be negligible for fairly small multiplicity intervals. For very low or high multiplicities, where the intervals had to be chosen larger for lack of statistics, the mixing-term contribution was subtracted.

Fig. V.7 shows the semi-inclusive correlation function $C_n(\eta_1^C, \eta_2)$ as a function of η_2 at various constant values of η_1^C for charged particle multiplicities $30 \leq n \leq 36$ at 900 GeV. C_n peaks at $\eta_2 = \eta_1^C$ and has the same shape as the inclusive short-range correlation function C_S. Moreover, one can see that at fixed multiplicity the value of C_n for $\eta_2 = \eta_1^C$ stays constant within errors for the central region, i.e. $|\eta_1, \eta_2| < 3.0$.

The multiplicity dependence of C_n for $\eta_1 = \eta_2$ is shown for 200, 546, and 900 GeV in

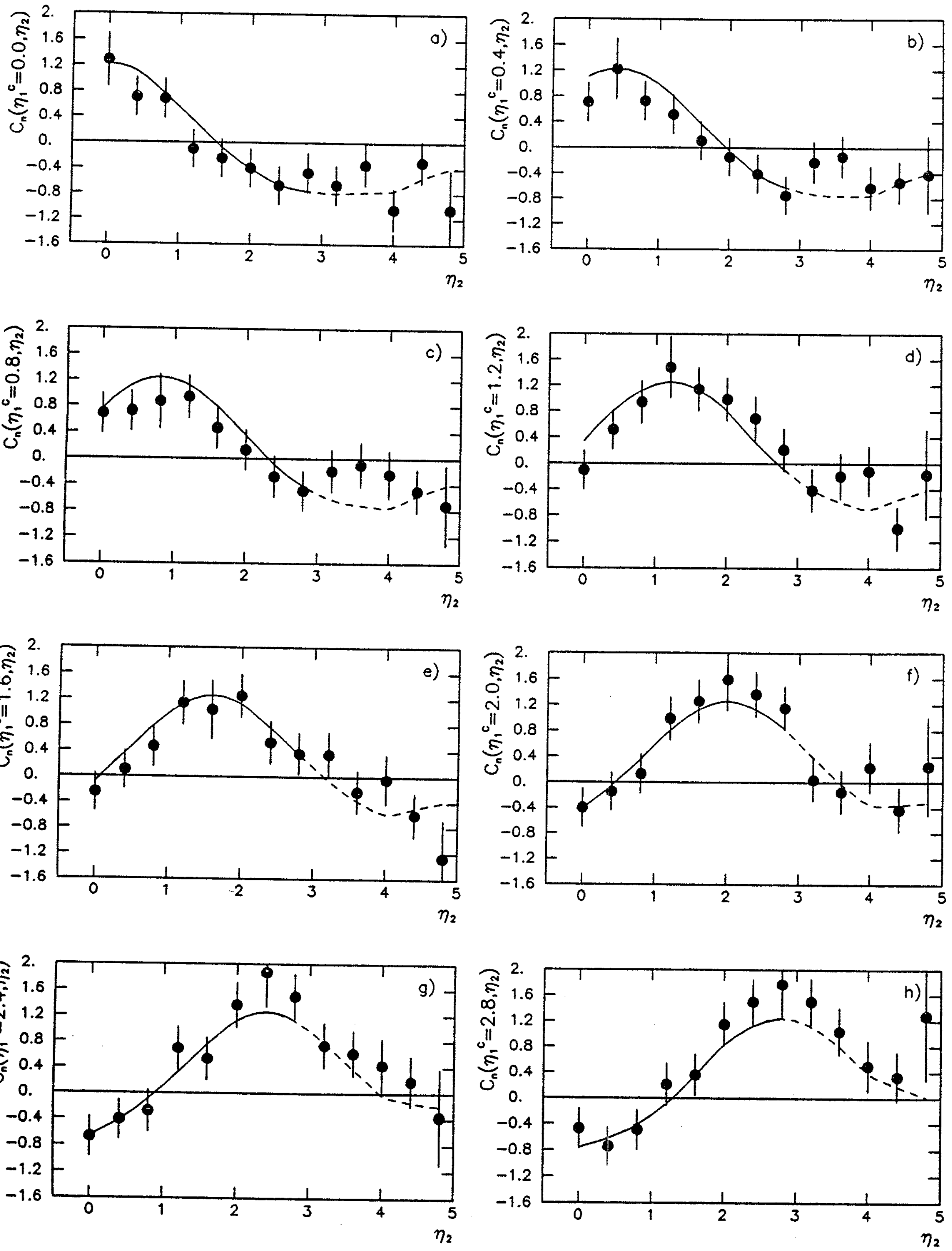

Figure V.7: The semi-inclusive correlation function $C_n(\eta_1^C, \eta_2)$ for charged multiplicities $30 \leq n \leq 36$ and fixed η_1^C at $\sqrt{s} = 900$ GeV for various ranges of η_2. The curves (full lines) indicate fits as explained in the text.

fig. V.8(a), where the quantity

$$\overline{C_n}(0) = \int_{-3.0}^{+3.0} C_n(\eta,\eta)\, d\eta \Big/ \int_{-3.0}^{+3.0} d\eta \tag{5.7}$$

is plotted versus the variable $z = n/\langle n\rangle$. It rises with increasing normalized multiplicity. This apparent increase, though, is caused by the different normalizations of the pseudorapidity densities (cf. equation 4.12). It turns out that the correlation function normalized such that it compares probability densities :

$$\overline{C_n\prime}(0) = \int_{-3.0}^{+3.0} \left(\frac{\rho_n^{II}(\eta,\eta)}{n(n-1)} - \frac{\rho_n^{I}(\eta)}{n} \cdot \frac{\rho_n^{I}(\eta)}{n} \right) d\eta \Big/ \int_{-3.0}^{+3.0} d\eta \tag{5.8}$$

is constant for multiplicities $n \gtrsim 0.5\langle n\rangle$ (fig. V.8(b)). This was also found at lower energies [KAF 77,EGG 75b]. Moreover, the data show no significant dependence on the c.m. energy within the range of Collider energies.

V.4 Cluster Model Interpretation

The most successful models in explaining and predicting the observed behavior of short-range correlations [COR] are cluster models ([MOD], see also appendix B of [UA5 87b]). They are simple models, that give an effective parametrization of the much more complicated underlying process. Many predictions of cluster models can be obtained analytically. The particles are produced in a two-step process :

- First, clusters are produced independently, assuming a flat cluster rapidity distribution in the central region.[1]
- Then, they decay isotropically in their rest frames to produce the final state particles;the decay parameters are taken to be independent of energy.

Under the assumption that clusters are low mass objects (up to a few GeV) the cluster decay distribution has the following form :

$$D(\eta, y_c) = \frac{0.5}{\cosh^2(\eta - y_c)} ,$$

where y_c is the rapidity of the cluster. It can be shown [BER 75a] that this distribution is well approximated by a Gaussian :

$$D(\eta, y_c) \approx \frac{1}{\sqrt{2\pi}\delta} \exp\left(-\frac{(\eta - y_c)^2}{2\delta^2} \right) ,$$

where δ is the decay width of the cluster in pseudorapidity.

The two-particle pseudorapidity distribution then splits into two terms according to whether both particles come from the decay of the same cluster or not, where the first term

[1] Taking a trapezoidal shape for this distribution does not alter the results but gives a better reproduction of the final state pseudorapidity distribution [HOL 87].

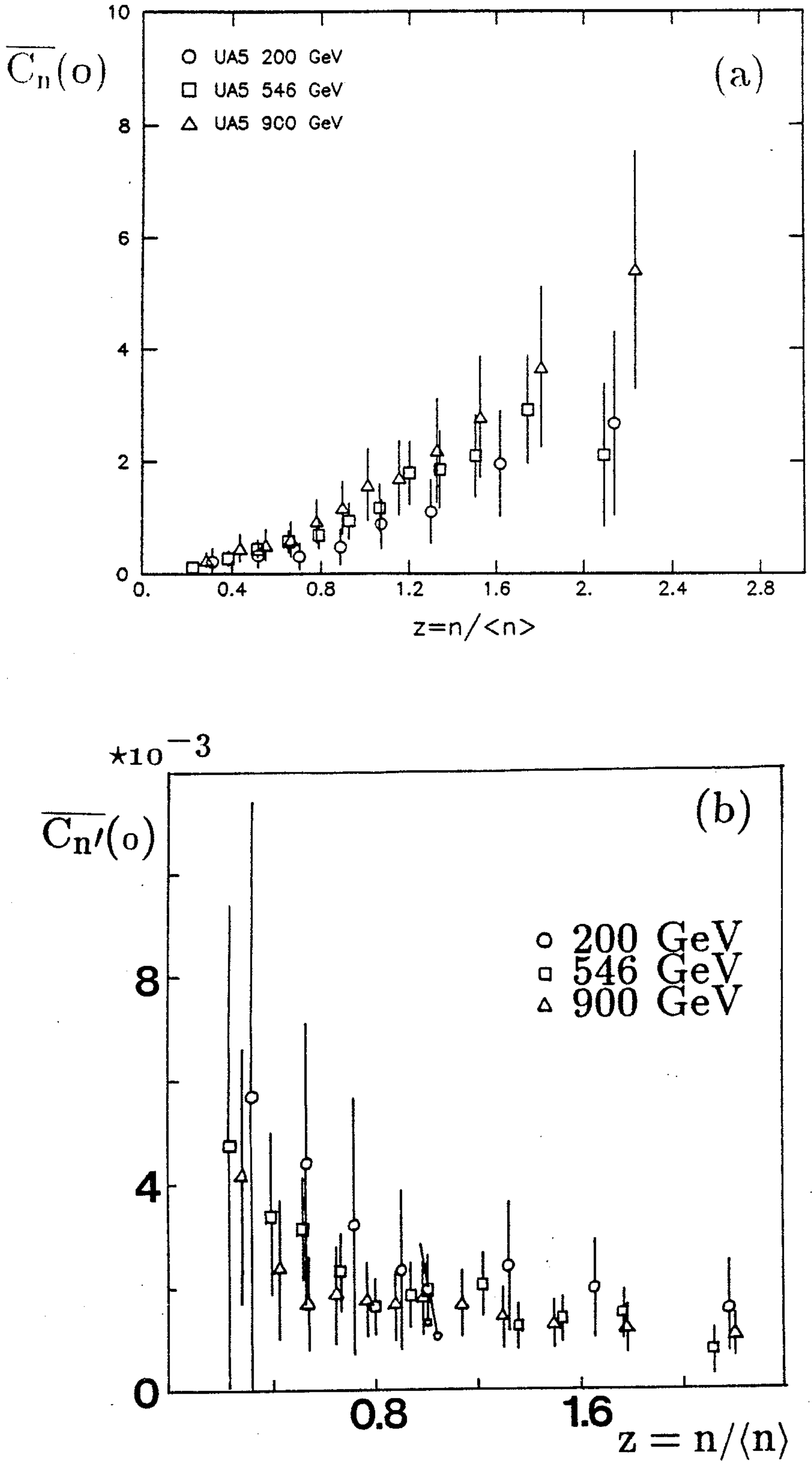

Figure V.8: The height of the semi-inclusive correlation function $\overline{C_n}(0)$ defined in equation 5.7 (a) and of the normalized correlation function $\overline{C_{n'}}(0)$ defined in equation 5.8 (b) as a function of $z = n/\langle n\rangle$ for 200, 546, and 900 GeV.

gives rise to the short-range correlations. The semi-inclusive correlation function is then predicted to be a Gaussian distribution plus a background term [UA5 87b] :

$$\begin{aligned} C_n(\eta_1,\eta_2) &= \left.\frac{\langle\kappa(\kappa-1)\rangle}{\langle\kappa\rangle}\right|_n \cdot \rho_n^I\left(\frac{\eta_1+\eta_2}{2}\right)\cdot\frac{1}{2\sqrt{\pi}\delta_n}\exp\left(-\frac{(\eta_1-\eta_2)^2}{4\delta_n^2}\right) \\ &\quad - \frac{\rho_n^I(\eta_1)\rho_n^I(\eta_2)}{n}\cdot\left(1+\left.\frac{\langle\kappa(\kappa-1)\rangle}{\langle\kappa\rangle}\right|_n\right), \end{aligned} \tag{5.9}$$

where κ is the multiplicity of charged particles in a cluster and δ_n the decay width in pseudorapidity space of the clusters produced in events with charged multiplicity n. No specific distribution for the cluster multiplicity has to be assumed for the derivation of equation 5.9.

Throughout this chapter the moments of κ, e.g. $\langle\kappa\rangle$, are usually calculated without considering clusters with $\kappa = 0$, e.g. clusters containing only neutral particles, since neutral particles can, in general, not be detected in this experiment. If clusters with $\kappa = 0$ are included, this is specifically indicated, e.g. $\langle\kappa\rangle_0$. The quantity $\left.\frac{\langle\kappa(\kappa-1)\rangle}{\langle\kappa\rangle}\right|_n$ is equal to $\left.\frac{\langle\kappa(\kappa-1)\rangle_0}{\langle\kappa\rangle_0}\right|_n$, since the exclusion of the neutral decay mode of clusters affects only the normalization of the moments.

Fig. V.7 shows the curves (full lines) obtained by fitting the correlation function $C_n(\eta_1,\eta_2)$ in the central region $|\eta_1,\eta_2| \leq 3$ to the cluster model predictions. The dashed lines are extrapolations using equation 5.9 and the fitted values of the cluster model parameters. The correlation functions are well described by the Gaussian fit.

Fig. V.9 gives the results for the two cluster model parameters $\left.\frac{\langle\kappa(\kappa-1)\rangle}{\langle\kappa\rangle}\right|_n$ and δ_n as a function of the variable $z = n/\langle n\rangle$ for 200, 546, and 900 GeV, compared to previously published results at lower energies [AME 76,BEL 84]. As is shown in fig. V.9(a) the quantity $\left.\frac{\langle\kappa(\kappa-1)\rangle}{\langle\kappa\rangle}\right|_n$ increases from ISR to Collider energies, though from 200 to 900 GeV no significant change is seen. However, the two ISR results show quite a different behavior as a function of z, i.e. the 44 GeV data decreases with increasing z whereas the 63 GeV data (obtained for a fixed value of $\delta_n = 0.6$) increases. This might show the systematic uncertainties in determining the cluster decay multiplicity moment for a small available range of pseudorapidity and/or small number of charged particles in the final state. For the cluster decay width δ_n (see fig. V.9(b)), our data show no significant multiplicity dependence, and are consistent, on the average, with the values obtained at the ISR.[2]

The cluster model parameters obtained, however, are subject to systematic uncertainties. The parameter values vary systematically with the size of the fit interval. This is due to the fact that the approximation of the cluster decay distribution as a function of pseudorapidity by a Gaussian is only good where the rapidity is well approximated by the pseudorapidity variable, i.e. in the central region, and causes the decay width δ to appear rapidity dependent. Therefore, Monte Carlo studies were used to determine the systematic errors caused by this effect. For too large an interval the parameters obtained from fits to the Monte Carlo data turned out to be too large with respect to the input parameters of the cluster model used to generate the Monte Carlo events. Too small a size for the fit interval ensued uncertainties in the fits due to lack of data points, and because the background

[2]For an isotropically decaying cluster one expects $\delta \approx 0.6 - 0.7$.

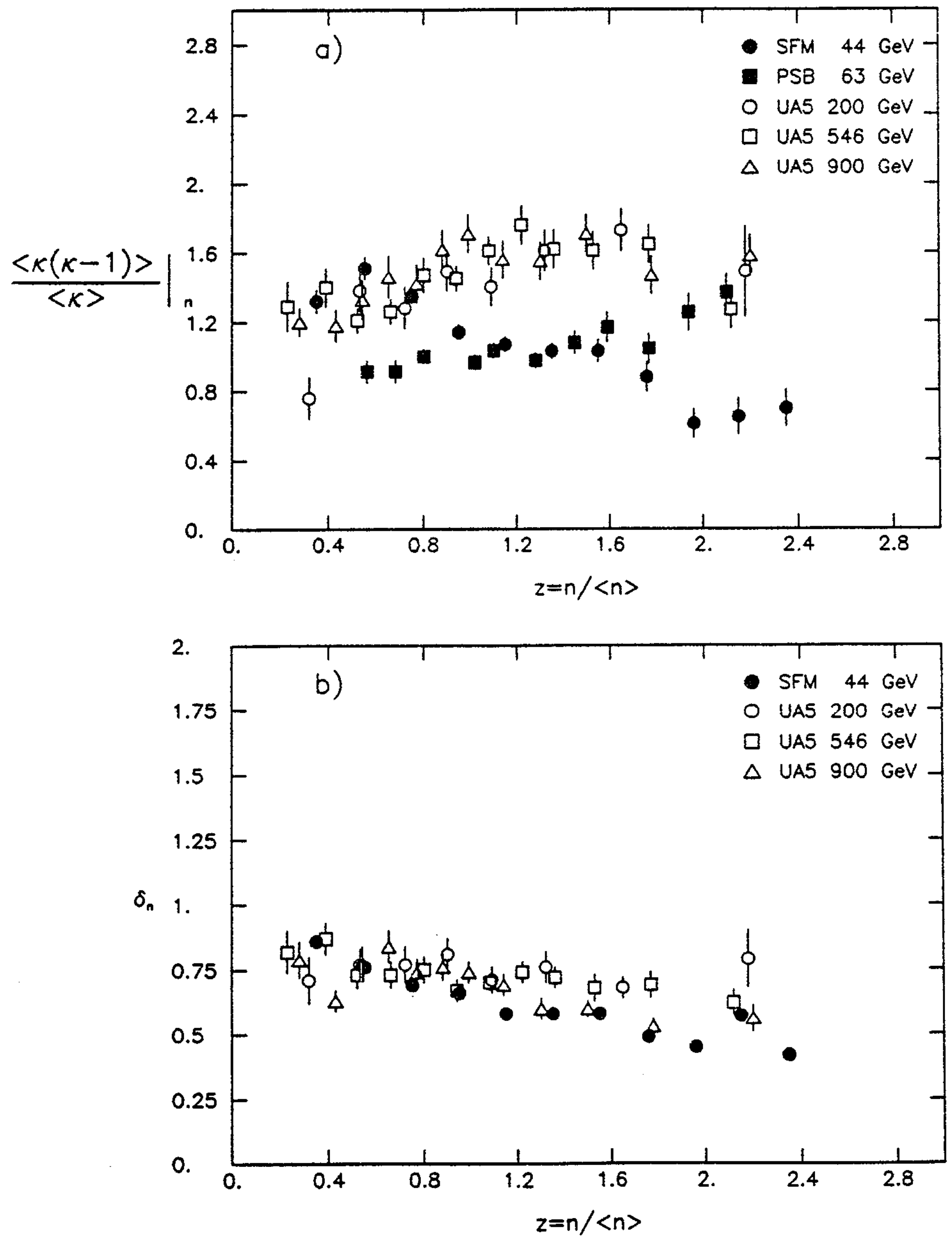

Figure V.9: In (a) the charged decay multiplicity moment $\left.\frac{\langle\kappa(\kappa-1)\rangle}{\langle\kappa\rangle}\right|_n$ is plotted versus the scaling variable $z = n/\langle n\rangle$ for the ISR energies 44 GeV [BEL 84] and 63 GeV [AME 76], and for 200, 546, and 900 GeV. (b) shows the cluster decay width as function of the scaling variable z for 44, 200, 546, and 900 GeV.

parameter	correlation function	63 GeV	200 GeV	546 GeV	900 GeV
$\frac{\langle\kappa(\kappa-1)\rangle}{\langle\kappa\rangle}$	inclusive	$1.24^{+0.20}_{-0.13}$	$1.55^{+0.11}_{-0.11}$	$1.63^{+0.10}_{-0.10}$	$1.67^{+0.10}_{-0.10}$
	semi-inclusive		$1.41^{+0.12}_{-0.12}$	$1.45^{+0.10}_{-0.10}$	$1.46^{+0.11}_{-0.11}$
δ	inclusive	$0.67^{+0.05}_{-0.05}$	$0.76^{+0.04}_{-0.04}$	$0.72^{+0.03}_{-0.03}$	$0.66^{+0.04}_{-0.04}$
	semi-inclusive		$0.75^{+0.06}_{-0.06}$	$0.73^{+0.05}_{-0.05}$	$0.65^{+0.05}_{-0.05}$

Table V.1: The two cluster model parameters for 63 GeV [DRI 79] and Collider energies. For the semi-inclusive correlation function the weighted average values of $\left.\frac{\langle\kappa(\kappa-1)\rangle}{\langle\kappa\rangle}\right|_n$ and δ_n are quoted.

beneath the correlation peak can no longer be reliably determined. The chosen interval $|\eta_1, \eta_2| \leq 3$ proved to give the best reproduction of the values of the cluster decay multiplicity moment $\left.\frac{\langle\kappa(\kappa-1)\rangle}{\langle\kappa\rangle}\right|_n$ and the decay width δ_n. The systematic errors are estimated to be about 5%.

The short-range correlation function, $C_S(\eta_1, \eta_2)$, obtained by the subtraction $C(\eta_1, \eta_2) - C_L(\eta_1, \eta_2)$, can also be fitted to the same cluster model predictions [BER 75] :

$$C_S(\eta_1, \eta_2) = \frac{\langle\kappa(\kappa-1)\rangle}{\langle\kappa\rangle} \cdot \rho^I\left(\frac{\eta_1+\eta_2}{2}\right) \cdot \frac{1}{2\sqrt{\pi}\delta} \exp\left(-\frac{(\eta_1-\eta_2)^2}{4\delta^2}\right) + \text{background} \ , \qquad (5.10)$$

where the shape of the background term depends on the cluster decay multiplicity chosen, e.g. for a Poisson distribution it is proportional to the product $\rho^I(\eta_1) \cdot \rho^I(\eta_2)$ [BER 75]. This was found to reproduce the background contribution in the data adequately. The results of these fits, compared in table V.1 with lower energy data [DRI 79], agree with the weighted average values obtained from the semi-inclusive distributions. There are small, systematic differences in the values for the cluster decay moments, $\frac{\langle\kappa(\kappa-1)\rangle}{\langle\kappa\rangle}$, obtained from the inclusive and the semi-inclusive measurement, caused by the difficulty of determining the "long-range" term C_L (equation 5.6). Since it consists of a sum with many contributions (multiplicities up to ≈ 100), small systematic deviations, e.g. caused by the difficulties in the acceptance correction for very small multiplicity intervals, can add up. The systematic errors on the cluster decay parameters obtained from fits to the inclusive data are about 10%.

V.5 Cluster Decay Multiplicity Distribution

For charged multiplicities ($n \gtrsim 10$) the cluster decay multiplicity moment, which indicates the width of the distribution, is independent of the overall multiplicity. Therefore, if the multiplicity is increased, the clusters do not become larger, but instead more clusters are produced.

Cluster models do not a priori assume a specific shape for the cluster decay multiplicity distribution. But if this is done ([BER 75], and also appendix B of [UA5 87b]), then they

c.m. energy	$\bar{n}$	k	$\langle\kappa\rangle_0$	χ^2/NDF
200 GeV	21.6	4.6	1.49 ± 0.05	8.7/7
546 GeV	28.3	3.7	1.51 ± 0.03	21.1/10
900 GeV	35.1	3.2	1.52 ± 0.02	11.6/11

Table V.2: The average charged cluster decay multiplicity for Collider energies obtained by fitting equation 5.12 with parameters $\bar{n}$ and k to the data.

can predict the dependence of $\left.\frac{\langle\kappa(\kappa-1)\rangle}{\langle\kappa\rangle}\right|_n$ on multiplicity n. A δ-function, for instance, where all clusters decay into a constant number of charged particles κ_C, yields a multiplicity independent behavior :

$$\left.\frac{\langle\kappa(\kappa-1)\rangle}{\langle\kappa\rangle}\right|_n = \kappa_C - 1 \; . \tag{5.11}$$

For a Poisson distribution with an average of $\langle\kappa\rangle_0$, however, one can derive a recursive relation depending on the average cluster decay size and the charged multiplicity distribution. The overall charged multiplicity distribution is well described by a negative binomial distribution [UA5 85d,UA5 86a] :

$$P_n = \frac{\sigma_n}{\sigma} = \binom{n+k-1}{n-1} \left(\frac{\bar{n}/k}{1+\bar{n}/k}\right)^n (1+\bar{n}/k)^{-k} \; ,$$

where k and $\bar{n}$ are the two parameters of the negative binomial distribution for the full phase space. One obtains for the charged cluster decay multiplicity moment :

$$\left.\frac{\langle\kappa(\kappa-1)\rangle}{\langle\kappa\rangle}\right|_n = \frac{n-1}{n+k-1} \cdot \frac{\bar{n}+k}{\bar{n}} \cdot \langle\kappa\rangle_0 \; . \tag{5.12}$$

The relation 5.12 has a free parameter $\langle\kappa\rangle_0$. Therefore, it was fitted to the 200, 546, and 900 GeV data using for the two parameters of the negative binomial the values quoted in [UA5 86a]. The results of the least squares fits are given in table V.2 and are also shown as curves in fig. V.10. It illustrates that equation 5.12 gives a satisfactory fit to the data. The value $\langle\kappa\rangle_0$ turns out to be energy independent for Collider energies.

At low multiplicities equation 5.12 seems to reproduce the data better than a fixed decay multiplicity. For multiplicities $n \gg k$ equation 5.12 does not differ significantly from a constant predicted by equation 5.11[3]. But, nevertheless, the data at high multiplicities are sufficiently far away from possible values $\kappa_C = 2$ or 3 (which have to be an integer) to exclude a constant decay multiplicity.

A Poisson distribution with an average of $\langle\kappa\rangle_0 = 1.5$ leads to an observed mean value after excluding decays into exclusively neutral particles $\langle\kappa\rangle \simeq 1.9$. This value is in good agreement with an ISR result [DRI 79,HOF 77] of $\langle\kappa\rangle \simeq 1.8$.

A fit to the inclusive data could, in principle, also be used to discriminate between different possibilities for the cluster decay multiplicity distribution, since the size of the

[3] If $n \gg k$ and $\bar{n} \gg k$ equation 5.12 tends to $\langle\kappa\rangle_0$; i.e. a constant as predicted by equation 5.11, but one unit larger.

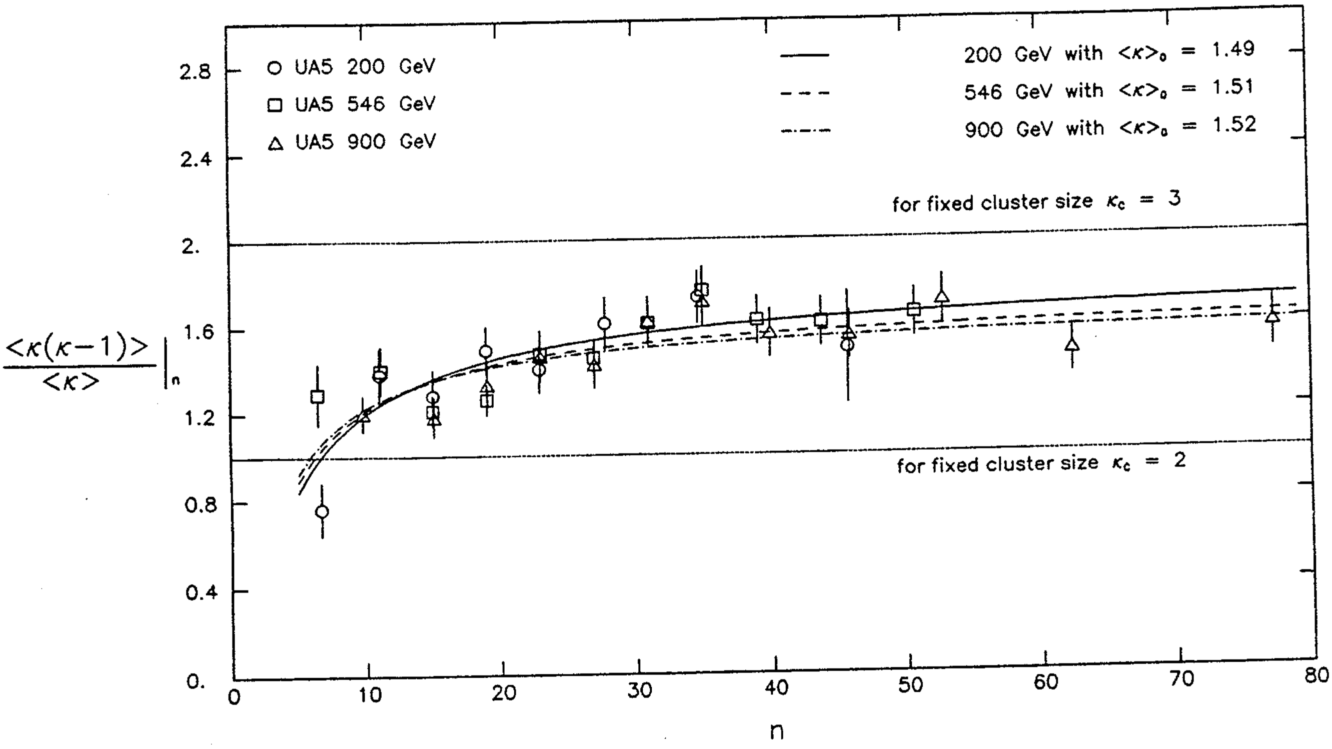

Figure V.10: The charged decay multiplicity moment $\left.\frac{\langle\kappa(\kappa-1)\rangle}{\langle\kappa\rangle}\right|_n$ is plotted versus n for 200, 546, and 900 GeV. The curves show the results of the least squares fit of equation 5.12 to the data. The horizontal lines represent two examples of this moment for fixed cluster sizes, i.e. $\kappa_C = 2$ and 3.

background term in equation 5.10 depends on the type of distribution chosen. Because of the systematic errors attached to the determination of $C_L(\eta_1, \eta_2)$, this is not feasible, though.

The previous section had shown that cluster models provide an adequate means of describing the data on correlations. The question remains, how these "objects" are to be interpreted. The obvious solution would be to identify clusters with low mass resonances (ρ, ω, K^*, ...), since a resonance decay clearly produces similar short-range correlations among its fragments. However, this poses problems, since the average charged decay multiplicity of resonances is expected to be lower. By extrapolation of the spectrum of resonances from lower energy data (see appendix A of [UA5 87b] and [MUE 83]) one obtains values of $\langle\kappa\rangle \simeq$ 1.4 to 1.5 and $\frac{\langle\kappa(\kappa-1)\rangle}{\langle\kappa\rangle} \approx 0.7$. These values are clearly lower than those obtained from the correlation analysis.

Thus additional short-range order effects are needed to explain the observed two-particle correlations in hadronic interactions. These could be caused by local quantum number conservation [WIL 63,KRZ 73,LEB 76] or by short chains fluctuating in their rapidity position as in the Dual Parton Model [CAP 85]. No detailed model calculations exist, however, based on either of the mentioned possibilities. A "cluster", therefore, cannot be directly identified with any physical object known sofar, but covers several different hadronic effects.

V.6 Comparisons with the UA5-Event Generator

The analysis of rapidity correlations is not the only means for providing information on the average cluster size. Investigations of the multiplicity correlations between forward ($\eta > 0$) and the backward ($\eta < 0$) hemispheres were also undertaken [UA5 83b,UA5 87b]. These studies are concerned with the following question : If one observes a certain number of particles in the forward hemisphere (or part of it), what can one expect to see in the backward hemisphere (or part of it). Evidently, these correlations are sensitive to long-range effects, concerning the event as a whole. But apart from the observation of long-range correlations it proved necessary to introduce the concept of "clusters", decaying on the average into 2 charged particles, in order to reproduce the data on multiplicity correlations.

The results on forward-backward multiplicity correlations prompted the introduction of a cluster model into the UA5 event generator. A very brief description has already been given in section III.7, the points relating to the simulation of particle correlations will be discussed in more detail below.

- Clusters of two different types are generated (disregarding the leading particles) :
  - Central baryons and strange particles are produced in clusters of fixed size 2, ensuring the local conservation of baryon and strangeness quantum numbers. The actual number of baryon and strange clusters is randomly generated from Poisson distributions whose averages reproduce the observed particle ratios. Since some of the decay particles are neutral, the charged cluster decay multiplicity distribution is very narrow with $\langle\kappa\rangle = 1.37$ and $\frac{\langle\kappa(\kappa-1)\rangle}{\langle\kappa\rangle} = 0.08$.

$\langle\kappa\rangle_0$	1.87
$\langle\kappa\rangle$	1.98
$\frac{\langle\kappa(\kappa-1)\rangle}{\langle\kappa\rangle}$	1.52

Table V.3: Moments of the charged cluster decay multiplicity distribution in the UA5-event generator for 900 GeV.

- Charged Pions are produced in clusters with a Poisson decay multiplicity distribution of average $\langle\kappa\rangle_0 = 1.8$, giving an average charged decay multiplicity $\langle\kappa\rangle = 2.16$ and $\frac{\langle\kappa(\kappa-1)\rangle}{\langle\kappa\rangle} = 1.8$. The Pion cluster multiplicity is determined by the overall charged multiplicity of the event, where care is taken not to introduce additional correlations through this constraint. The charge of each Pion is fixed to ensure overall charge conservation in the event. Each of the Pion clusters is given some number of neutral Pions (on the average 1.3 π^0 per cluster).

- The overall charged cluster decay multiplicity distribution (pairs + Pions) is not a Poisson distribution, but is reasonably close. The parameters are given in table V.3 for 900 GeV. The values at 200 GeV and 546 GeV differ only insignificantly (at 200 GeV they are $\approx 3\%$ higher) because the strange particle and baryon multiplicities increase with energy.

- All clusters made up of more than one particle are given some excitation energy in terms of additional mass according to an exponentially declining distribution, chosen to represent the mass spectrum of known resonances, with an average value of about 2 GeV. The clusters decay isotropically in their rest frame with an average decay width $\delta = 0.68$ independent of energy.

The moments of the cluster decay multiplicity distribution, as well as the decay width, reproduce the results obtained from the analysis of the correlation functions, given the systematic uncertainties in determining the decay width. Another cross-check is the direct comparison of the correlation functions in data and Monte Carlo. Fig. V.11 shows the semi-inclusive correlation function $C_n(\eta, 0)$ for charged multiplicities $30 \leq n \leq 36$, (a), and the overall average $C_S(\eta, 0)$, (b), compared to the distributions calculated from event generator data for different average charged cluster sizes. C_n and C_S were averaged over the central region to reduce the statistical fluctuations. The standard value of $\langle\kappa\rangle = 2$ reproduces the data well, whereas $\langle\kappa\rangle = 1.7$ and $\langle\kappa\rangle = 2.3$ are clearly excluded. The deviations in C_S at large η-values are caused by the difficulties in determining this quantity in the data, discussed in section V.4. Both data and eventgenerator are consistent. This justifies the corrections applied to the data (cf. chapter IV).

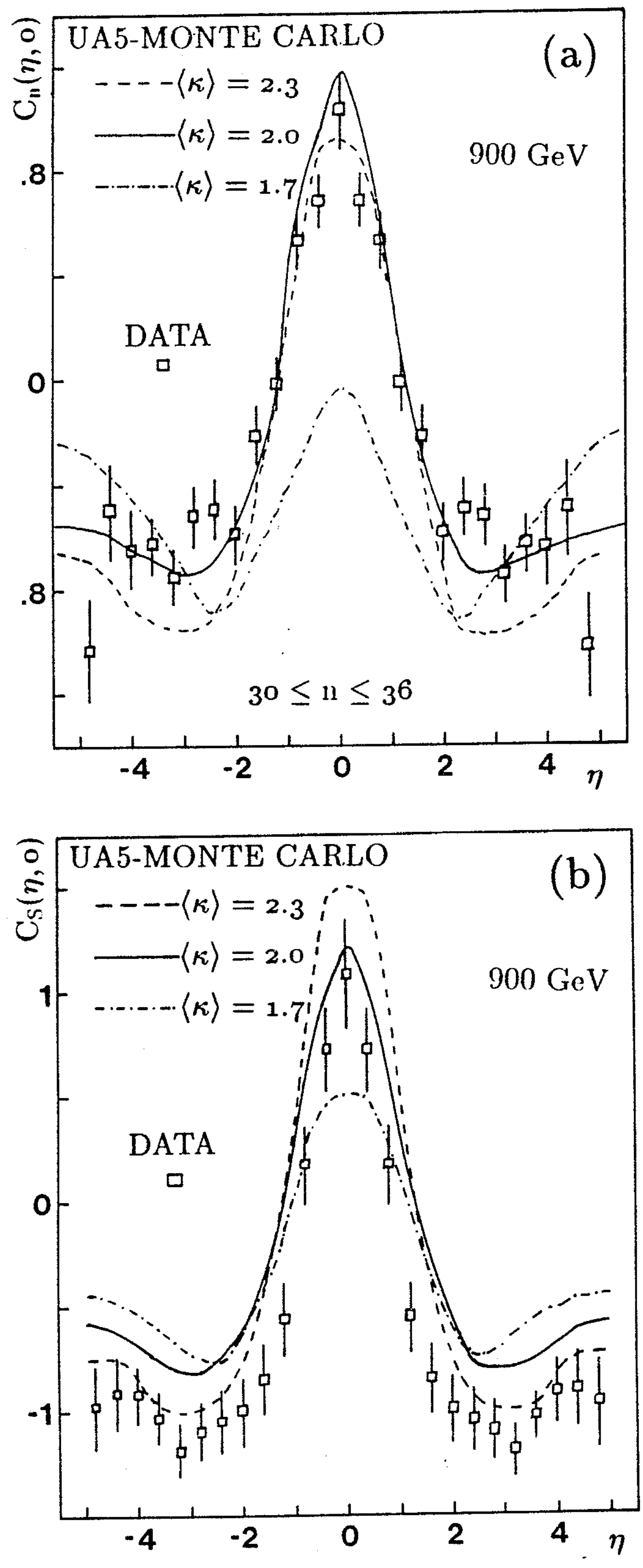

Figure V.11: Semi-inclusive correlation function $C_n(\eta, 0)$ for charged multiplicities $30 \leq n \leq 36$, (a), and the overall average $C_S(\eta, 0)$, (b), compared to the distributions calculated from event generator data for different average charged cluster sizes at 900 GeV.

Chapter VI

Local Fluctuations in Pseudorapidity Density

VI.1 Introduction

Events with a large local concentration of particles in a very small rapidity window have been studied in cosmic ray experiments for a long time [ALE 62]. The JACEE group, investigating high energy interactions with balloon-borne emulsion chambers [VER 84], have reported several unusually high multiplicity events with a large concentration of tracks in a small rapidity range, and consequently a very large energy density[1] ($\sim$ 4 GeV/fm^3) [BUR 83]. Recently, high density events have been observed in hadron collisions at accelerators [RUS 84,ADA 86].

These so-called "spikes" are found to be associated with a random azimuthal distribution; not showing any jet-like features. Various possibilities have been suggested as to their origin :

- A random superpositioning of particles and/or clusters of particles.
- Quarks traversing a quark-gluon medium could produce gluon radiation (Ĉerenkov-gluons) in a similar manner to Ĉerenkov radiation produced by electrons whose velocity exceeds the speed of light in the medium they traverse. Each of the radiated gluons produces hadrons which will be seen to be emitted in a cone around the incident particle direction. This coherent hadron production would show up as a large, narrow peak in the (pseudo-)rapidity distribution and have a uniform distribution in azimuth [DRE 81].
- It has been suggested that at high matter densities ($\sim 1-2$ GeV/fm^3) and/or sufficiently large temperatures (T$\gtrsim$150 MeV) a phase transition ("deconfinement transition") from the hadron gas (composed of well separated hadrons) to a quark-gluon plasma (quarks and gluons are no longer confined in hadrons) can take place [JAC 82]. Such a state of matter is assumed to have predominated in the early universe until $\sim 10^4$ sec after the big bang, and to be produced in heavy ion collisions. In p$\bar{\text{p}}$-collisions at c.m. energy of less than 1 TeV the energy density is normally insufficient to induce this phase transition, but the fluctuations in particle densities from event to event can be rather large, so that some (high multiplicity) events can have a large energy density.

  The quark-gluon plasma hadronizes in the cooling-off phase and can therefore, not be directly detected, but it is predicted to leave certain signatures. In p$\bar{\text{p}}$-interactions

[1] The number of particles per (pseudo-)rapidity interval is a measure of the energy density.

at the Collider it was found that the average transverse momentum as a function of multiplicity levels off instead of increasing steadily [ARN 82]. This has been interpreted as a possible indication of quark-gluon plasma formation [HAG 84]. In Oxygen-Uranium-collisions at the CERN-SPS a suppression of J/ψ-production has been found [GEI 87]. Another possible sign is an enhanced rapidity density fluctuation connected with azimuthal symmetry caused by the explosive hadronization of the quark-gluon plasma [GYU 83].

One source of local rapidity fluctuations found in the data is evidently of pure statistical nature, caused by the finite multiplicity values analyzed. Normally, one avoids these fluctuations by averaging quantities over many events. But this would reduce fluctuations of non-statistical nature as well. One has to do the analysis on an event by event basis. Several methods for analyzing and interpreting local density fluctuations have been proposed :

- A study of the behavior of factorial moments of the rapidity distribution in a region of size δy shows that the dependence on δy is different, if the fluctuations are of pure statistical nature or if they are of dynamical origin [BIA 86]. However, one requires very high multiplicities in order to have enough statistics in small δy intervals; so this method is only applicable in very high energy cosmic ray events, or nuclear collisions.
- Fluctuations have been interpreted [DRE 87] as being caused by a Gaussian random field [CLI 68] (e.g. the isotropic decay of a cluster).
- The concept of intermittency, familiar in turbulence theory, can be used to generate large fluctuations [DIA 87a]. In this picture partons, travelling through hadronic matter, emit either many particles in chaotic bursts or only few particles regularly, depending on the matter density. Predictions can then be made for fluctuations on an event by event basis [DIA 87b].

Analyses on the basis of a statistical theory have the drawback of requiring a large amount of data and/or sufficient particle numbers. This is clearly not the case in this experiment, if fluctuations in very small rapidity windows are analyzed. Therefore, local density fluctuations will in most cases be interpreted with respect to Monte Carlo data provided by the UA5-Monte Carlo program (cf. section III.7). This procedure also has the advantage that one can use uncorrected data.

Apart from possibly providing information on the properties and nature of density fluctuations, these comparisons serve as a test of the Monte Carlo program, that has not a priori been designed to reproduce the features of density fluctuations. Conversely, the distributions discussed in this chapter can provide a means for testing the predictions of other theoretical models.

VI.2 Spike Multiplicity Distribution

Large fluctuations in pseudorapidity are found by determining the maximum number of particles in each event inside a window of given size $\Delta\eta$. By sliding the window over the full η-range and counting the multiplicity inside, for each position, the largest multiplicity n_s ("spike" multiplicity) is determined for each event; this is illustrated in fig. VI.1. The spike multiplicity n_s is, of course, larger than the <u>average</u> multiplicity, determined by

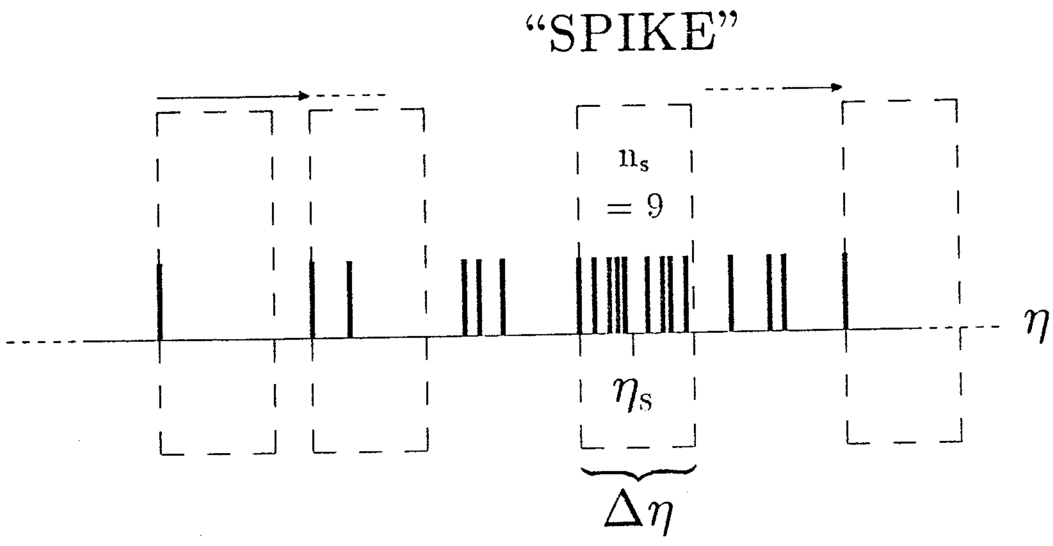

Figure VI.1: The algorithm for finding "spikes".

$\rho^I{}_{n_{obs}}(\eta_S) \cdot \Delta\eta$), at the spike position η_S, for an event of a given observed multiplicity n_{obs} and pseudorapidity density $\rho^I{}_{n_{obs}}$.[2] In fig. VI.2 plots of the azimuthal angle ϕ versus the pseudorapidity η and its projection onto the pseudorapidity axis for all charged tracks found in events with very large spike multiplicities are shown (the location of the spike is indicated). In these events about one third of all the particles are concentrated in a region of 1/2 unit in pseudorapidity. Events generated with the UA5-Monte Carlo program show similarly large fluctuations; one example is shown in the same figure (VI.2(d)).

It should be stressed that all values and figures shown in this chapter pertain to observed quantities only, unless otherwise stated. A correction of the data, analogous to that given in chapter IV, cannot be made for quantities calculated on an event by event basis. They are only possible for averages, such as rapidity densities. This should be kept in mind when comparing data at different energies with different detector acceptances, or data coming from completely different experiments. To judge the effect of a finite detector acceptance in some distributions Monte Carlo simulated data after tracking through the detector ("observed ") is compared to simulated event generator data ("true"). The data is restricted to events with observed multiplicity $n_{obs} > 1$.

In fig. VI.3 the spike multiplicity distribution for a window size $\Delta\eta = 0.5$ is shown separately for 200, 546, and 900 GeV. They are similar in shape to the charged multiplicity distribution and show an exponential fall-off at high multiplicities. The location of the maximum, though, appears to remain unchanged with energy. The width increases; this is to be expected, since the spike multiplicity should reflect the increase of the pseudorapidity density with energy. The Monte Carlo shows very good agreement for all energies. A comparison of Monte Carlo data and event generator data shows the effects of our finite detector acceptance to be small and very similar for all energies.

The largest values for the spike multiplicity were found in 2 events at 900 GeV with

[2]To destinguish between observed (uncorected) and corrected quantities, the index "obs" is introduced, whenever this could cause confusion.

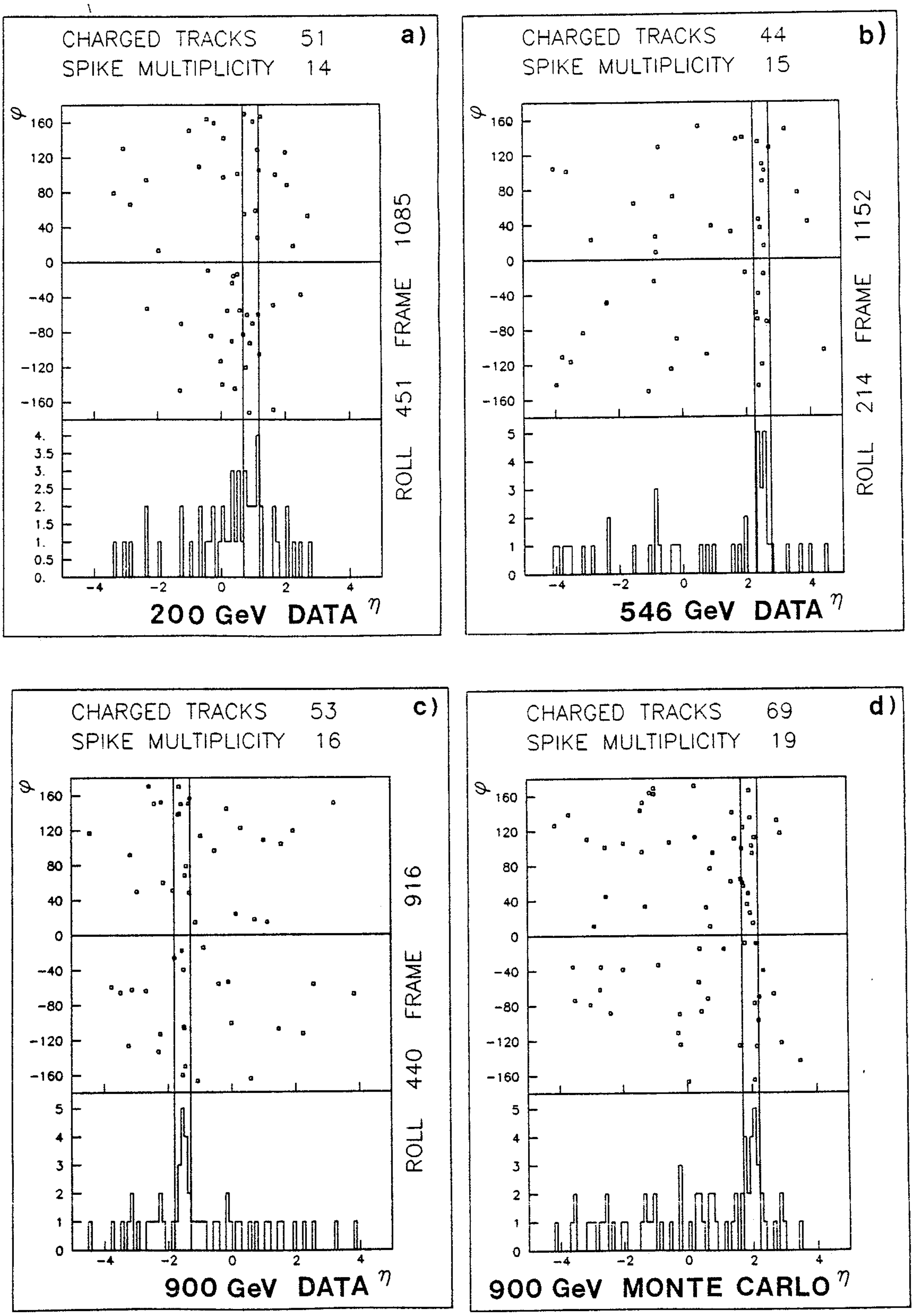

Figure VI.2: Examples of events with large fluctuations in pseudorapidity density at 200, 546, and 900 GeV and for a Monte Carlo event (lower right hand corner).

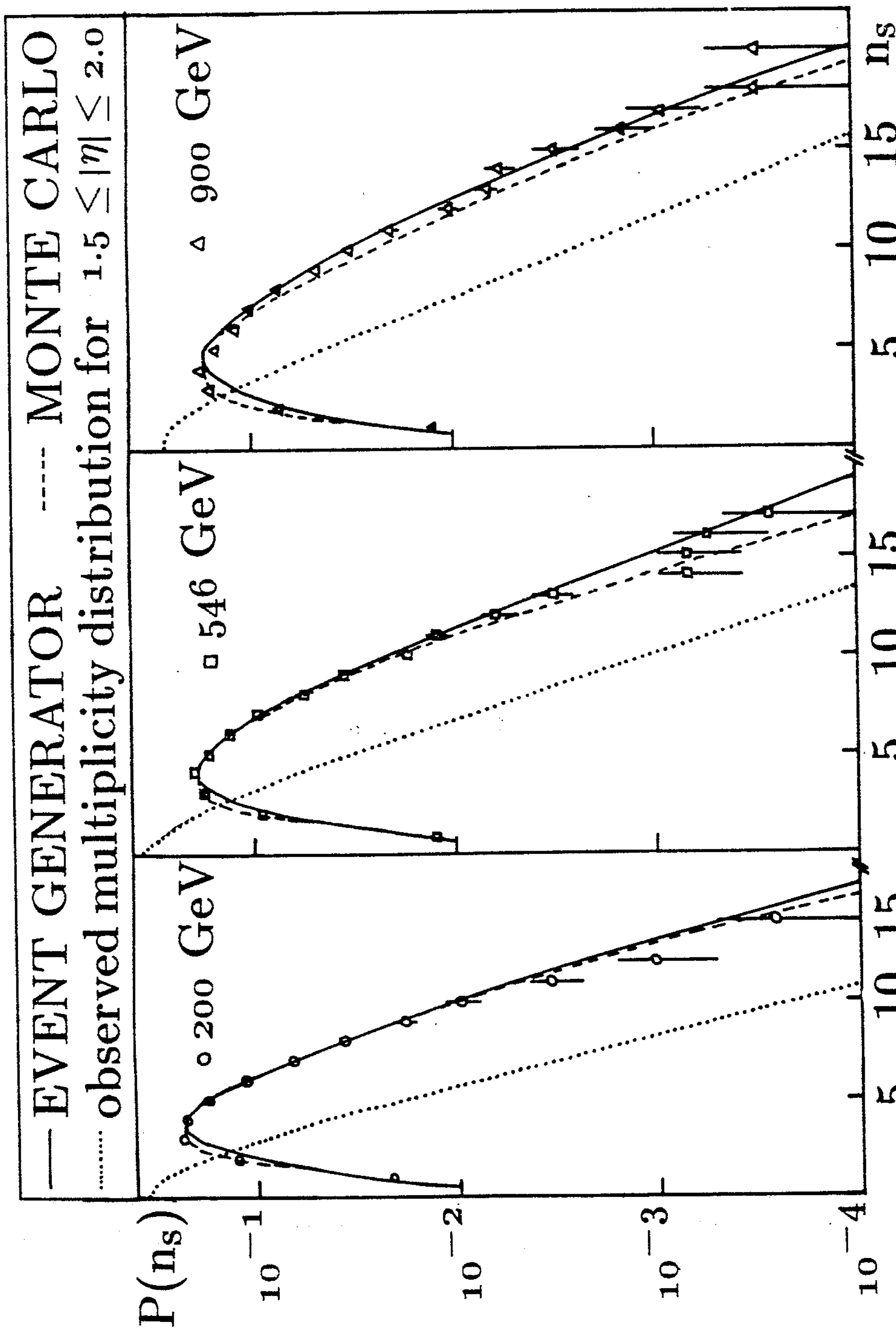

Figure VI.3: Spike multiplicity distribution for 200, 546, and 900 GeV compared to Monte Carlo data before (solid curve) and after (dashed curve) tracking through the detector. The dotted curve shows the observed multiplicity distribution in the range $1.5 < |\eta| < 2$.

$\Delta\eta$	200 GeV	546 GeV	900 GeV
		DATA	
0.1	2.36 ± 0.01	2.60 ± 0.01	2.80 ± 0.01
0.5	4.37 ± 0.03	5.01 ± 0.03	5.48 ± 0.03
1.0	6.16 ± 0.05	7.23 ± 0.04	8.00 ± 0.05
		MONTE CARLO	
0.1	2.39 ± 0.01	2.60 ± 0.01	2.72 ± 0.01
0.5	4.43 ± 0.02	4.97 ± 0.02	5.33 ± 0.02
1.0	6.35 ± 0.03	7.19 ± 0.04	7.78 ± 0.04

Table VI.1: The average spike multiplicity for different c.m. energies and window sizes.

$n_s = 20$ from a total of 6514 events at that energy.[3] The averages $\langle n_s \rangle$ of all distributions are given in table VI.1, as well as those for window sizes $\Delta\eta$ of 0.1 and 1.0. Again the agreement with Monte Carlo data is good. The data show the expected increase with energy and window size.

In the following studies the window size will be restricted to the interval $\Delta\eta = 0.5$, unless a comparison is made with data of other experiments. By studying the location of individual tracks inside the window, and the occurrence of multiple maxima of the same size in a given event, a window size of $\Delta\eta = 0.5$ was found to be the most adequate for analyzing local rapidity fluctuations. For smaller windows the average distance between particles is rather large compared to the window size, whereas with larger windows local structures tend to be smeared out.

In order to study the energy dependence of the spike multiplicity distribution, the variable $z_s = n_s/\langle n_s \rangle$ is introduced in analogy to the normalized charged multiplicity $z = n/\langle n \rangle$. The comparison in fig. VI.4(a) shows that the curves coincide, only at higher multiplicities do they broaden by a small amount as the energy is increased. The integral distribution in fig. VI.4(b), showing the sum

$$S(z_s) = \sum_{z=z_s}^{\infty} \langle n_s \rangle P(z) ,$$

gives more precise information on the tail of the normalized spike multiplicity distribution. It confirms the tendencies seen in fig. VI.4(a) and also the good agreement with the Monte Carlo data.

VI.3 Dependence of the spike multiplicity on the overall charged particle multiplicity

Since the height of the charged particle pseudorapidity distribution increases with multiplicity, the spike multiplicity n_s should show a similar dependence. This effect is illustrated in

[3] If the distribution of tracks along the pseudorapidity axis were completely random the total sample would be given by the number of windows examined, which is equal to the total number of particles observed, i.e. the number of events (6514) times the average observed multiplicity (26.4). Then the highest spike multiplicities come from a sample of 2 in 6514*26.4 or 1:86 000.

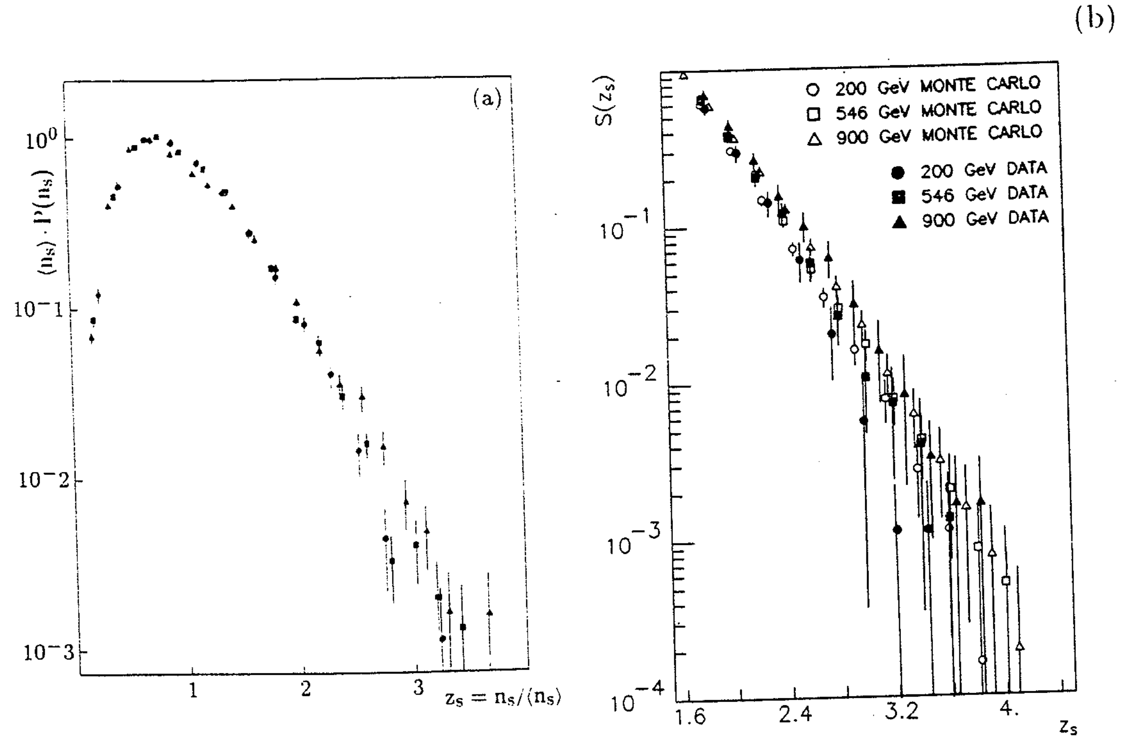

Figure VI.4: Normalized spike multiplicity distribution (a) and its integral (b). The closed symbols represent data, the open symbols Monte Carlo.

fig. VI.5 for the 900 GeV data, where the frequency of events with a given overall observed multiplicity n_{obs} and spike multiplicity n_s is plotted (the area of the circles is proportional to the number of events). For comparison the average observed multiplicity in the interval $\Delta\eta$ taken in the central region, for events of a given multiplicity n_{obs}, is indicated.

Not only does the average spike multiplicity increase with the overall multiplicity, but the width of the distribution as well.[4] In fig. VI.6 slices of fig. VI.5 are shown for three multiplicity intervals, normalized to the total number of events in the corresponding interval for c.m. energies 200 GeV 546 GeV, and 900 GeV. The shift to larger values of n_s with increasing n_{obs} is obvious, also the broadening of the distribution. No energy dependence is visible.

The average density in the spike is plotted in fig. VI.7 as a function of the observed overall multiplicity and shows an almost linear increase, though a linear fit to the data for $n_{obs} \gtrsim 10$ was found not to be able to adequately reproduce the data. A good description for all n_{obs} is obtained with the following function :

$$\langle n_s\rangle/\Delta\eta = (a + b\,n_{obs} + c\,n_{obs}{}^2)(1 - d^{n_{obs}}) \tag{6.1}$$

The last term (provided d $<$ 1) reproduces the bend at small multiplicities and quickly approaches the value 1 for larger n_{obs}. The quadratic term is necessary for the fit not to overestimate the data at larger multiplicities. The values of the fit parameters and the χ^2 values are shown in table VI.2 for all energies. Qualitatively, the quantity $\langle n_s\rangle/\Delta\eta$

[4] It should be noted that the fraction of events at high multiplicities n_{obs} is very small compared to that at low multiplicities.

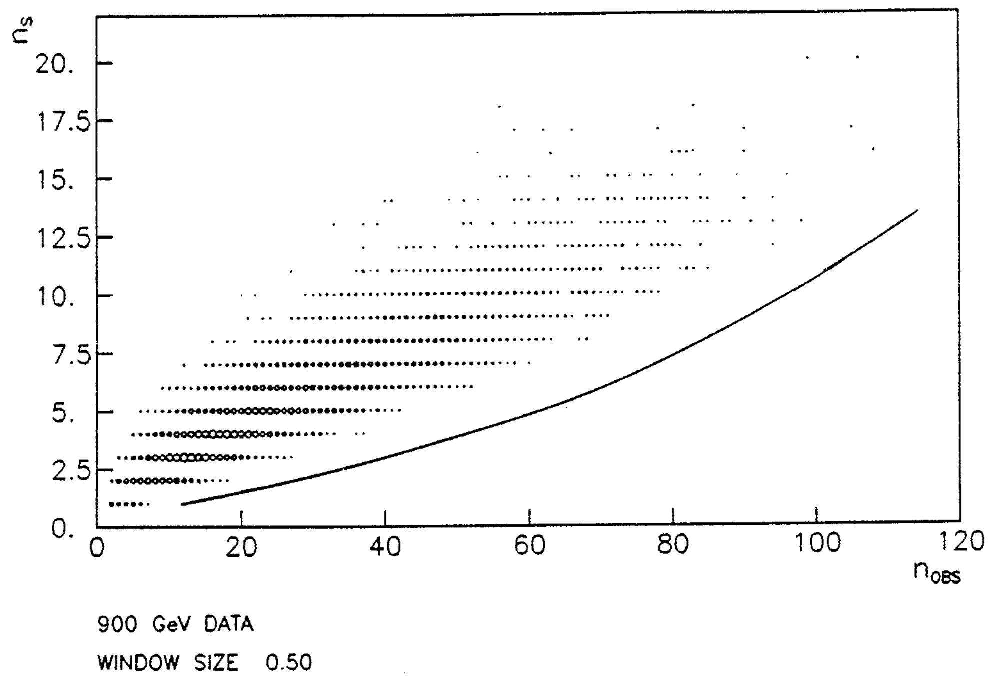

Figure VI.5: Spike multiplicity distribution versus the overall observed multiplicity shown for the 900 GeV data. The line shows the average observed multiplicity in the interval $\Delta\eta$ taken in the central region for events of a given multiplicity n_{obs}.

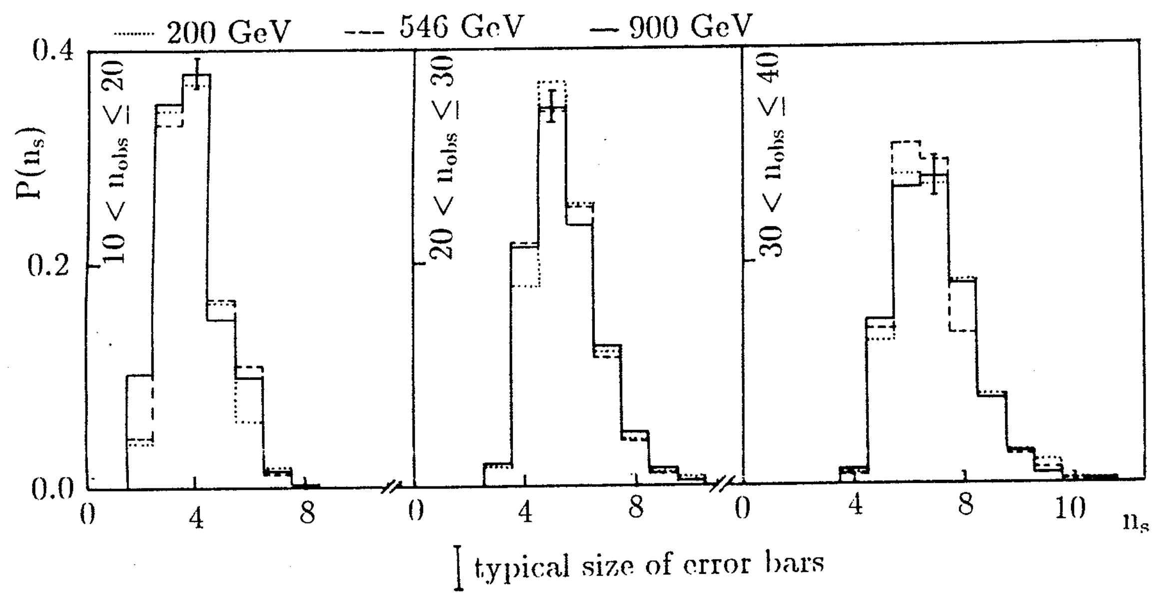

Figure VI.6: Spike multiplicity distribution for different intervals of charged multiplicity at 200, 546, and 900 GeV.

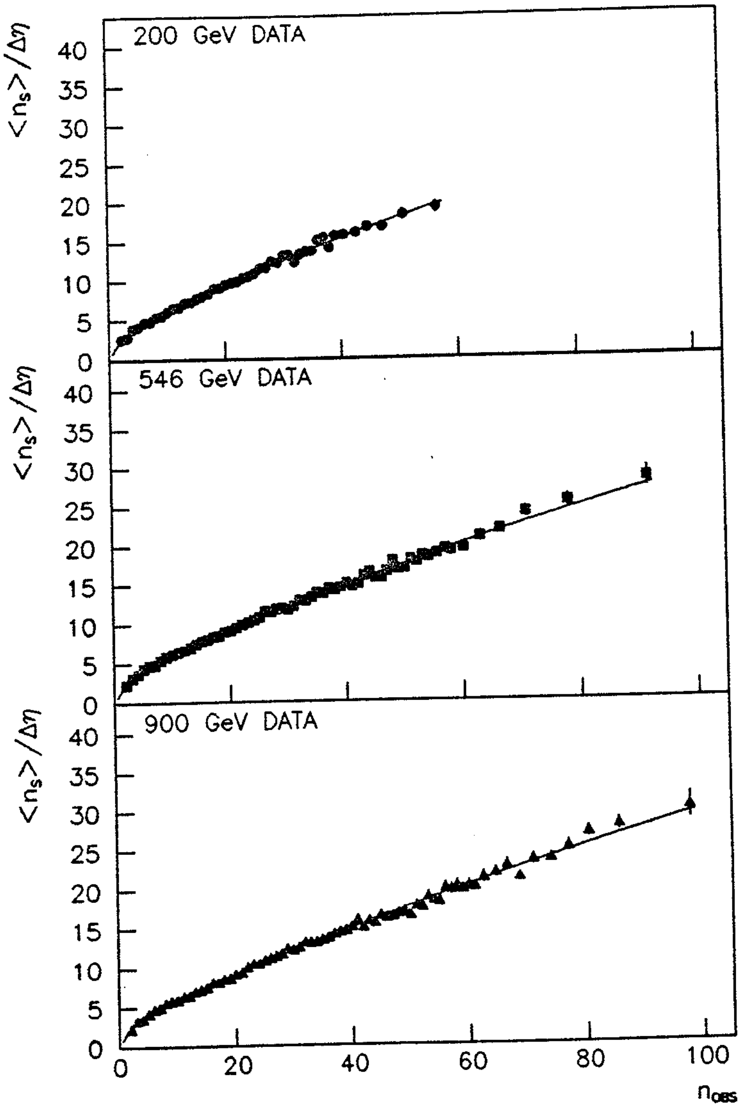

Figure VI.7: Fit to the multiplicity dependence of the average spike multiplicity.

	200 GeV	546 GeV	900 GeV
a	2.43 ± 0.06	2.93 ± 0.04	2.92 ± 0.10
b	0.377 ± 0.004	0.328 ± 0.002	0.326 ± 0.007
c	-0.0012 ± 0.0004	-0.0006 ± 0.0001	-0.0006 ± 0.0002
d	0.48 ± 0.04	0.59 ± 0.02	0.57 ± 0.03
χ^2/NDF	40.4/40	66.7/58	84.5/66

Table VI.2: Fit of the multiplicity dependence of average spike density to equation 6.1.

shows the same behavior at all energies, the fits for the 546 GeV and the 900 GeV data are identical within errors.

In fig. VI.8 all data are shown together; no difference is seen between 900 GeV and 546 GeV, though the 200 GeV points lie higher, if only by a small amount. This possible decrease of the average spike density with energy is also suggested by a comparison with low energy data [ADA 86] shown in the same figure. The significance of this energy dependence is enhanced, however, if the effect of corrections is treated in more detail :

Since the UA5-data shown in fig. VI.8 are uncorrected, one has to consider systematic effects caused by our finite detector acceptance. This is illustrated in fig. VI.9 for all three energies separately. Here the data points are plotted along with fits—of the same type as equation 6.1—to Monte Carlo simulated events and those obtained only with the event generator. Since the "observed" Monte Carlo follows the data quite well, the dashed curve should approximately represent the true location of the data points. With respect to the energy dependence (fig. VI.8 and table VI.2) one can conclude the following :

- The linear term is reduced to about 83%, 79%, and 76% for 200, 546, and 900 GeV, respectively. Therefore, the data points at the different energies are pushed further apart and should not coincide any longer. The overlap of the distributions from 200 to 900 GeV, seems to be rather accidental, caused by the influence of our finite detector acceptance.
- The quadratic term is no longer relevant, i.e. for $n_{obs} \gtrsim 10$ a linear fit should be sufficient. With respect to the data at 22 GeV one can say that all data start off at the same point, but the low energy data soon lies systematically above the higher energy data.

In reference [DIA 87b] a one-dimensional model of intermittency (cf. section VI.1) is used to predict a linear increase of the average density in the spike with the overall multiplicity. This model, though, implies an energy independent behavior, which is likely to be ruled out.

VI.4 Angular Distributions of Spikes

According to some models (cf. section VI.1), local density fluctuations should be enhanced in certain regions of pseudorapidity and show a uniform distribution of tracks in azimuthal angle Φ (as opposed to jet events). The examples of high density events shown in fig. VI.2 indeed show a uniform distribution of tracks in the spike.

In analogy to the sphericity variable introduced in jet-studies a "pseudosphericity" PS is introduced [GEI 85] (as momenta can not be measured here) :

$$1 - \mathrm{PS} = \frac{1}{n_s}\sqrt{\left(\sum_{i=1}^{n_s} \cos\Phi_i\right)^2 + \left(\sum_{i=1}^{n_s} \sin\Phi_i\right)^2}\,, \tag{6.2}$$

where Φ_i is the azimuth of each track in the spike. PS distinguishes between an isotropic distribution ($1 - \mathrm{PS} = 0$) and a single, collimated jet ($1 - \mathrm{PS} = 1$). Fig. VI.10 shows the pseudosphericity distribution versus the spike multiplicity. The curves show the average

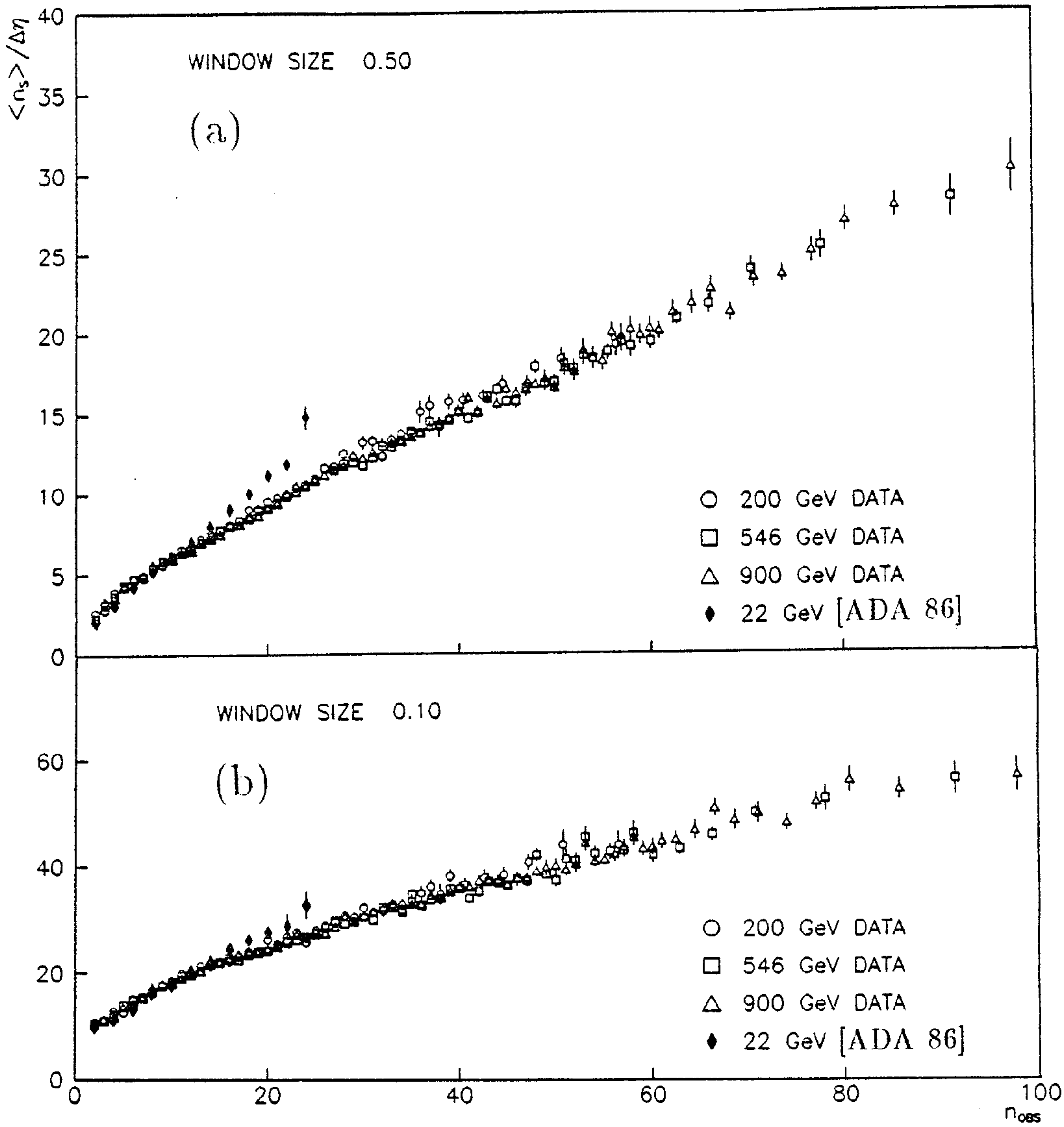

Figure VI.8: Energy dependence of the average spike multiplicity

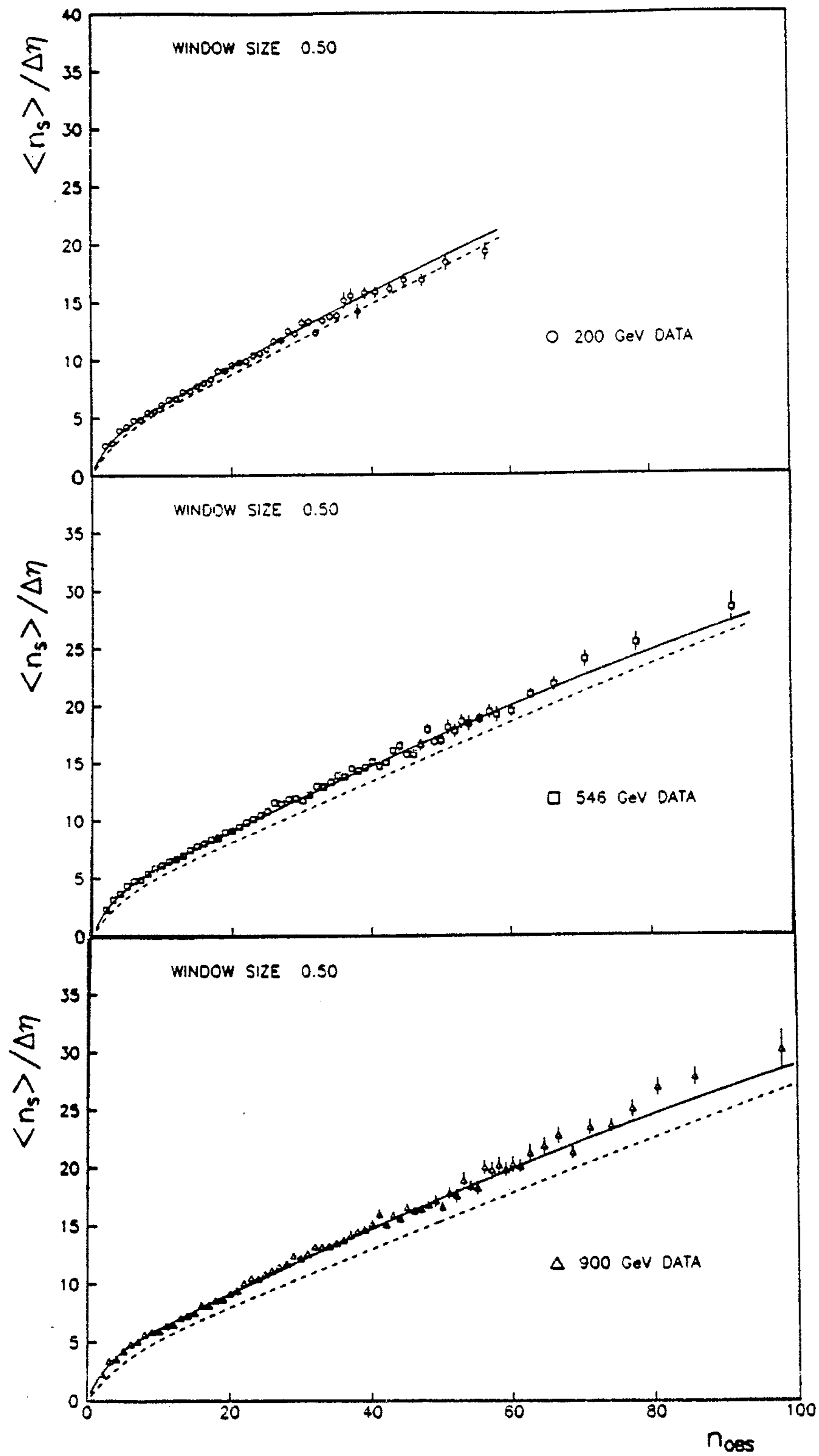

Figure VI.9: Influence of the detector acceptance on the average spike multiplicity. The solid curves show fits to the Monte Carlo data, the dashed curves fits to the event generator data.

values calculated from a random distribution of n_s tracks in azimuth (solid) curve and one standard deviation (broken curves). The data are seen to be consistent with a random distribution in azimuth and show no jet-like features.

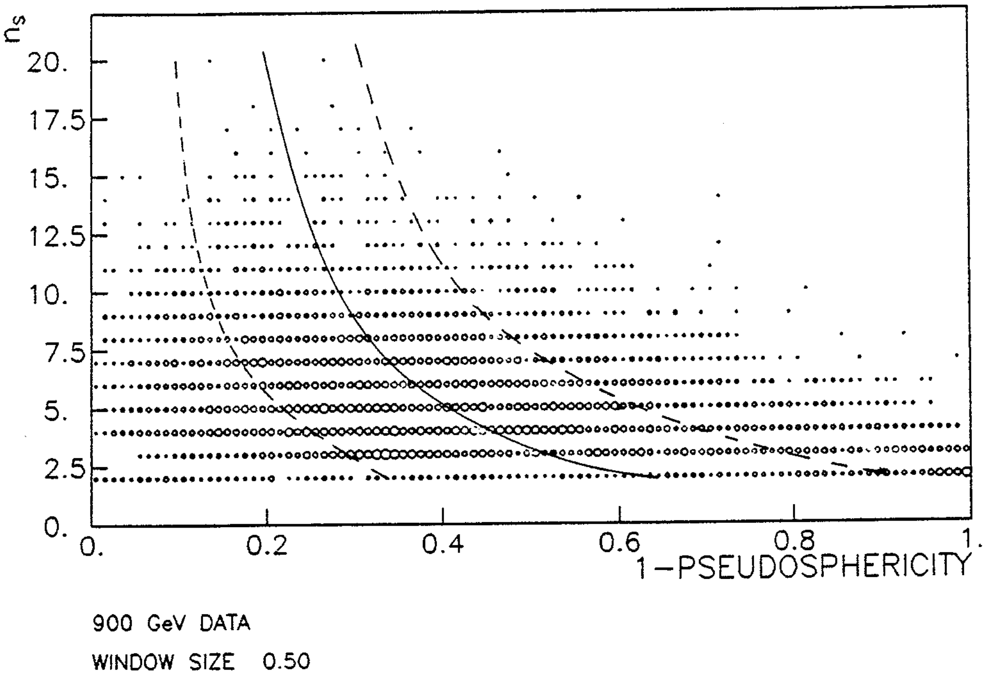

Figure VI.10: The distribution of pseudosphericity and spike multiplicity for events at 900 GeV. The curves show the average values calculated from a random distribution of n_s tracks in azimuth (solid) curve and one standard deviation (broken curves).

The location of the spike is taken to be the average of all pseudorapidity values of the tracks inside the spike

$$\eta_S = \frac{1}{n_s}\sum_{i=1}^{n_s} \eta_i \ .$$

The η_S distribution of events for a given spike multiplicity and its projection are shown in fig. VI.11 for 900 GeV. No preference of any pseudorapidity region is seen. The shape of the spike pseudorapidity distribution resembles the overall pseudorapidity distribution with a slight dip in the center, and a broadening at small (spike-)multiplicity values. In other words, spikes are, as expected, predominantly in those regions, where the pseudorapidity density is largest.

VI.5 Deviation of Density Fluctuations from Average Densities

The observation of a high density fluctuation raises the question of how much these fluctuations deviate from the expected average values. In particular, to what extent a large spike multiplicity is caused by the fact that the average density in an event is high.

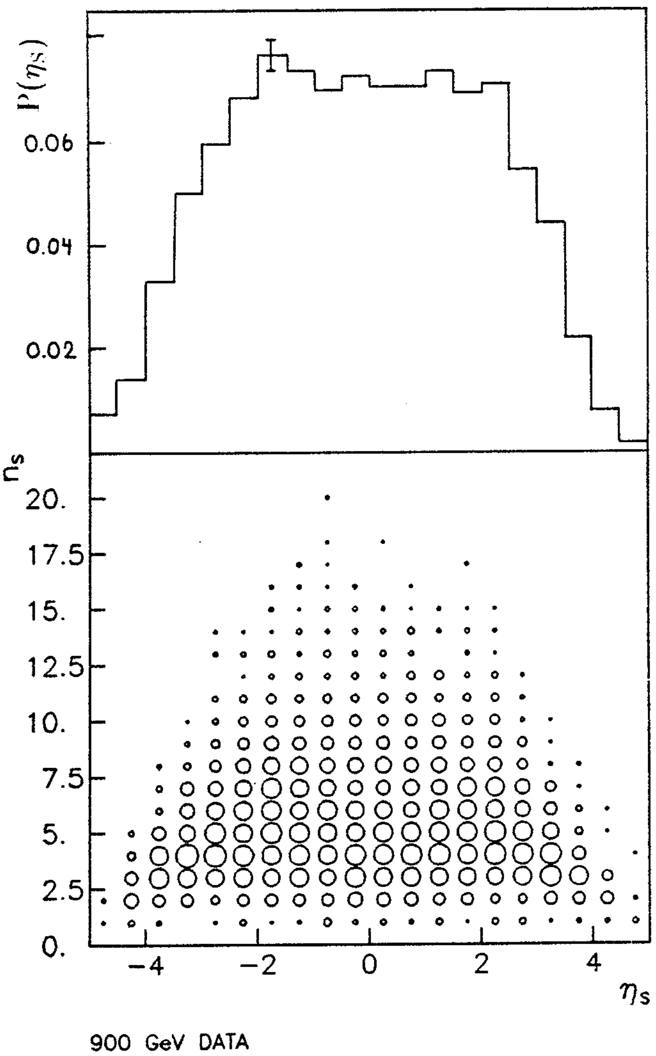

Figure VI.11: Pseudorapidity distribution of spike events (a) and the distribution of spike multiplicity versus spike location (b) for 900 GeV.

One possible measure of this is to determine the deviation of the spike density from the density in the region adjacent to the spike, i.e. the quantity $n_s - n_b$, where n_b is the multiplicity in the intervals of size $\Delta\eta$ on both sides of the spike, averaged, in the same event. The distribution of n_b plotted against n_s for 900 GeV is shown in fig. VI.12. One sees

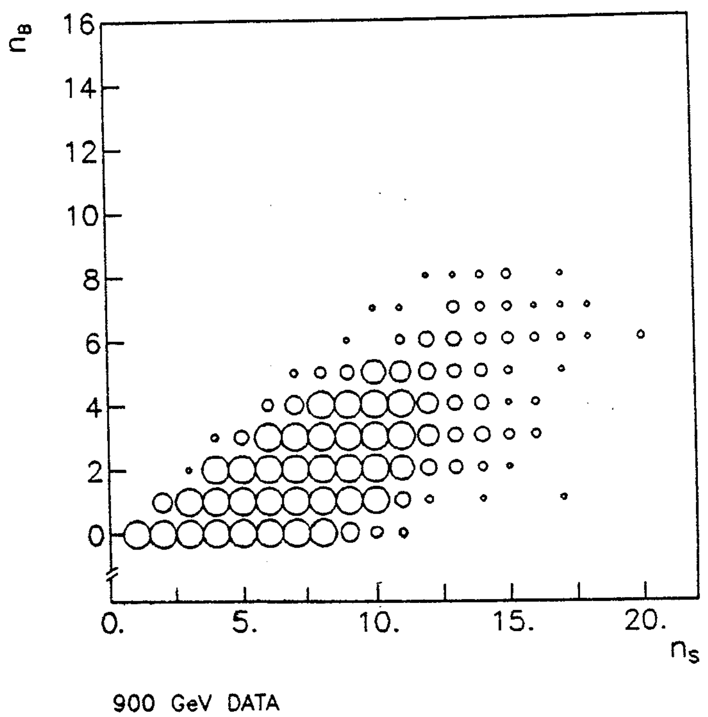

Figure VI.12: Background multiplicity plotted against spike multiplicity for 900 GeV.

that both quantities are correlated; many of the high density fluctuations also have a large number of neighboring tracks. This indicates that large spike multiplicities, in general, do not deviate much from their surroundings, and only show a high multiplicity because they are in a region where the track density is large anyway. No separate sample of events with a large denisity fluctuation and low background can be discerned in fig. VI.12.

Another possibility for defining the deviation of a local fluctuation from the expected value is to determine the average multiplicity in the interval $\Delta\eta$ for all events of a given observed multiplicity n_{obs} as a function of pseudorapidity η; given by the observed semi-inclusive pseudorapidity distributions :

$$\overline{n}(\eta, n_{obs}) = \int_{\eta}^{\eta+\Delta\eta} \rho^{I}_{n_{obs}}(\eta')d\eta' ,$$

where $[\eta, \eta + \Delta\eta]$ is chosen to be the window that contains the spike. The deviation of the spike multiplicity n_s from the average quantity $\overline{n}(\eta, n_{obs})$ can then be defined in terms of a test statistic, introduced in [EAD 71] :

$$t(n_{obs}) = \frac{n_s - \overline{n}(\eta, n_{obs})}{\sqrt{n_s + \overline{n}(\eta, n_{obs})}} . \tag{6.3}$$

The distribution of the deviation t is shown in fig. VI.13 against the observed multiplicity n_{obs} for 900 GeV. The line indicates the mean values of t, that are almost independent of multiplicity, as would be expected if the spike multiplicities are statistically distributed. There is no indication for a subset of events that show unusually lareg deviations. For very low multiplicities ($n_{obs} \lesssim 10$) the $\rho^I{}_{n_{obs}}$ densities cannot be reliably calculated, so the values of t are very uncertain. At the high multiplicity end there are too few events at a given multiplicity to determine a deviation from an average value.

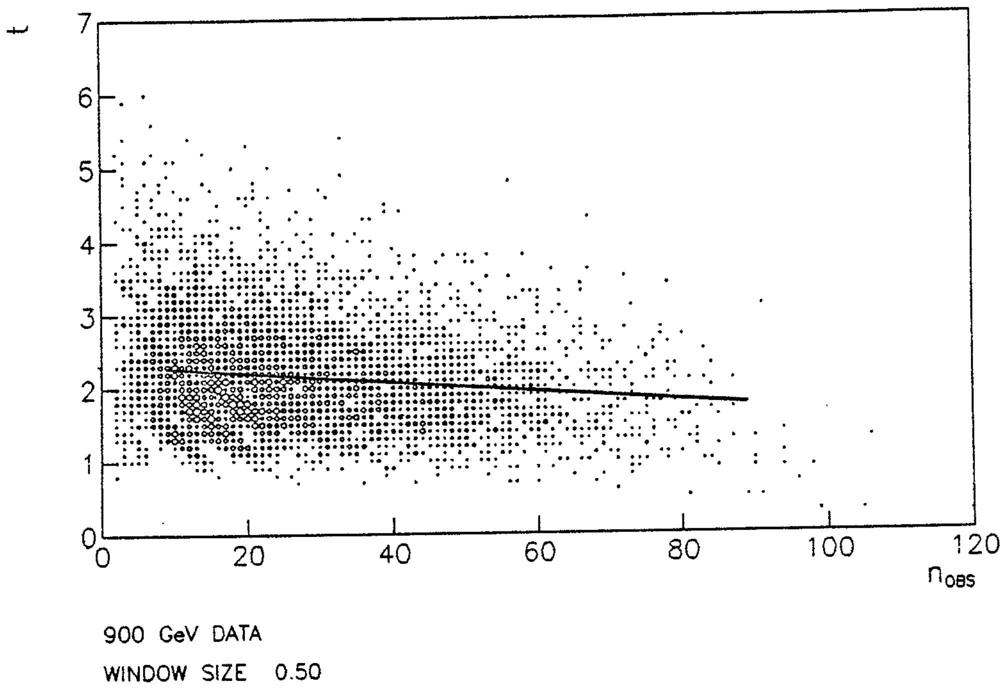

Figure VI.13: Deviation t of the spike multiplicity from the average pseudorapidity density according to equation 6.3 for 900 GeV. The line indicates the average values of t as a function of the observed multiplicity.

The variable t defined in equation 6.3 can be interpreted as a "standard deviation", ans one can, in general, determine the odds against exceeding t standard deviations, if the multiplicities n_s are large enough to be normally distributed around $\bar{n}$. Since one is dealing with rather small numbers ($n_s \leq 20$), this is not the case. Furthermore, the choice of region selected for analysis (i.e. the spike location) is not made <u>independently</u> of the data, but rather one is selecting the <u>largest</u> fluctuation in a given event and, therefore, introducing a bias. One can use this variable t, though, for comparisons with the Monte Carlo data. Shown in fig. VI.14 is the fraction of events in the region $t \geq 3$ as a function of the multiplicity n_{obs} for data (open symbols) and Monte Carlo (closed symbols). The event fraction decreases with multiplicity, but increases with energy, contrary to the behavior of the central pseudorapidity density (cf. section IV.4). The Monte Carlo agrees very well with the data.

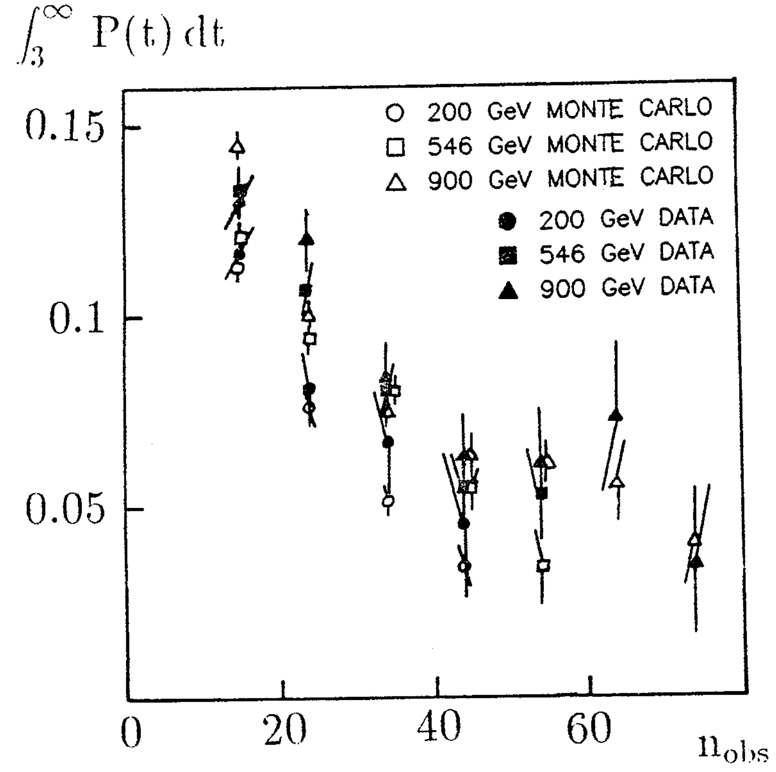

Figure VI.14: The fraction of events with $t \geq 3$, with t defined in equation 6.3 for data (open symbols) and Monte Carlo (closed symbols) at 200, 546, and 900 GeV.

VI.6 Correlations in Events with Large Local Density Fluctuations

The observation of high local densities in the data—as well as in the Monte Carlo—raises the question of how these fluctuations are produced; whether just by random superpositioning of tracks or clusters of tracks, or even an altogether different phenomena, such as the formation of a quark gluon plasma.

A possible signature of the formation of a quark gluon plasma could be a decrease of short-range correlations; the quarks and antiquarks in the plasma should recombine randomly [GEI 87], not allowing for any short-range order effects. The cluster sizes determined in the analysis of short-range correlations (e.g. fig. V.10) showed no decrease for high multiplicity events (where the possible formation of a quark gluon plasma is most likely to be expected). This does not exclude, though, that a very small sample of events (e.g. those with a large density fluctuation) shows a different behavior. Lack of statistics prevents an analysis in terms of correlation functions.

If a large spike were to be caused by one or several heavy clusters (decaying into many particles), then the occurrence of spike events should be sensitive to the cluster size used in the event generator (cf. section V.6). Fig. VI.15(a)-(b) shows the fraction of events with high spike multiplicity $n_s \geq 15$ (a) and the average spike multiplicity (b) as a function of the average charged cluster size for event generator data at 900 GeV.[5] The mean $\langle n_s \rangle$ clearly increases with $\langle \kappa \rangle$, though the effect is small; increasing $\langle \kappa \rangle$ by a factor of 2 changes $\langle n_s \rangle$ only by about 2%. No evidence for an increase in the high density events is seen. This implies that the cluster decay multiplicity influences <u>all</u> events in a similar proportion, and does not affect the large multiplicities to a higher degree. The average $\langle n_s \rangle$ is statistically better determined than the high multiplicity fraction and, therefore, shows the influence more easily. The standard value of $\langle \kappa \rangle = 2$ reproduces the data (table VI.1), if one takes the detector acceptance into account; whereas no clustering (i.e. $\langle \kappa \rangle = 1$) seems excluded. Figs. VI.15(c)-(d) show the same quantities for the spike multiplicity with the background subtracted (cf. section VI.4); here the same conclusions can be drawn.

The clustering mechanism,i.e. $\langle \kappa \rangle > 1$, is, therefore, not a dominant effect for the formation of high density fluctuations, but clustering does seem to be needed for a good representation of the data. The properties of cluster size and decay (predominantly small clusters of about 2 charged particles and a decay width $\delta \approx 0.7$ that is large compared to the size of local density fluctuations, cf. chapter V) are such, that no obvious clustering effect can be discerned in any given event.[6]

Long-range correlations deal with the question whether the fact that one observes a certain multiplicity in some rapidity region affects the multiplicity in any other region in a given event. Fig. VI.16 shows the distribution of the multiplicity n_s of the largest spike and the second largest spike n_{nex} in the same event.[7] Both multiplicities are correlated, there are only few events, where $n_{nex} \ll n_s$. This suggests, as was already seen in section VI.4, that a large spike multiplicity implies an overall large density. The distance in pseudorapidity between both spikes is plotted in fig. VI.17 for different intervals of n_s (the histograms are

[5]Note, that these figures cannot be directly compared with the data, because they do not contain acceptance effects.

[6]increasing the window size does not change the results.

[7]The second largest spike is determined by the same procedure described in section VI.2, excluding the region of the largest spike.

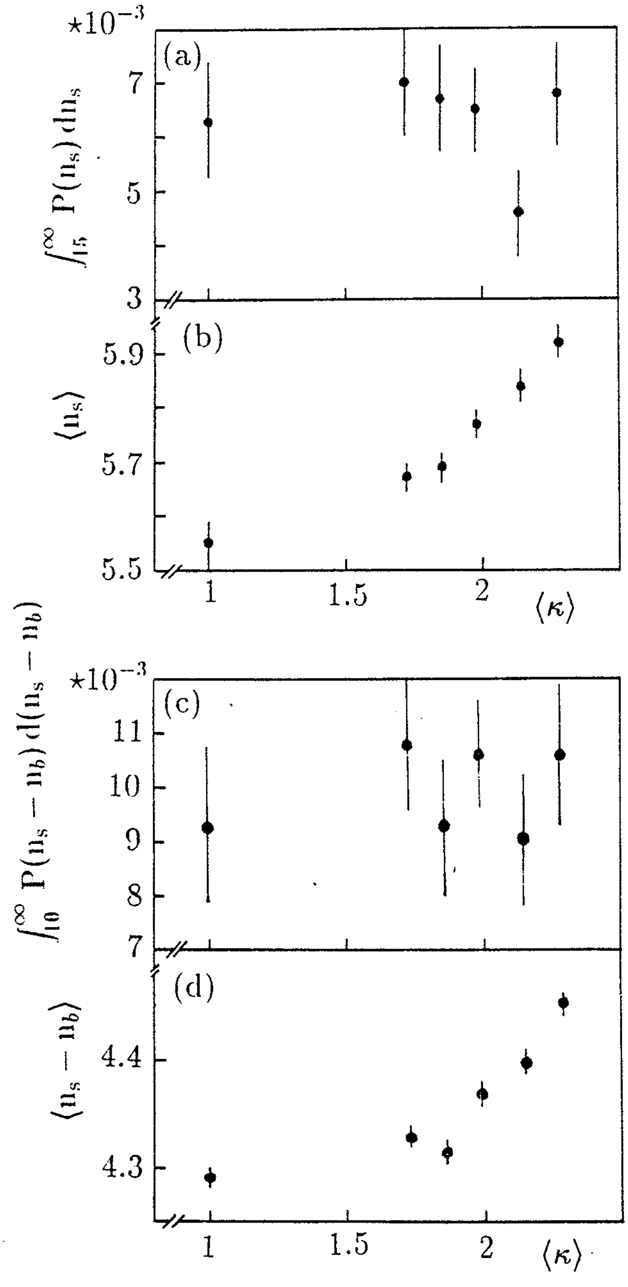

Figure VI.15: The fraction of events with $n_s \geq 15$ (a) and the average spike multiplicity $\langle n_s \rangle$ (b) as a function of the average charged cluster decay multiplicity in the event generator. (c) and (d) show the same quantities using the reduced spike multiplicity with the background subtracted.

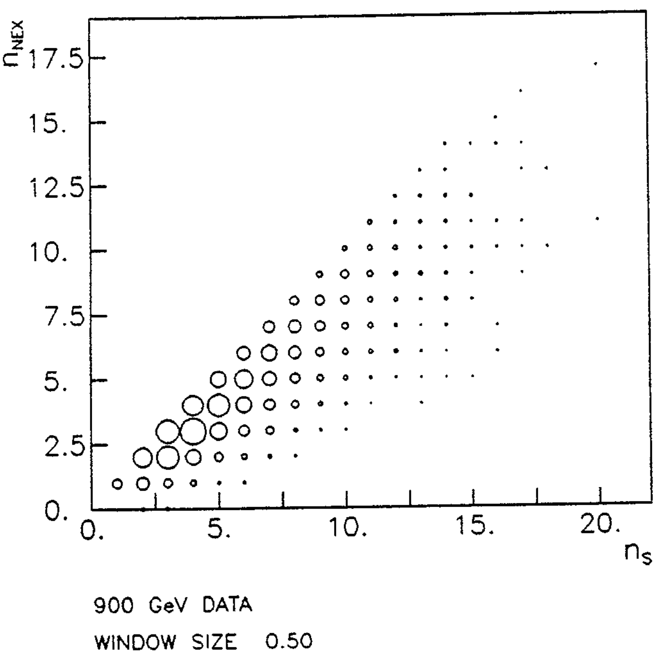

Figure VI.16: Multiplicity of second largest spike n_{nex} plotted against the multiplicity of the largest spike n_s in the same event for 900 GeV.

normalized to the same height). Most of the spikes are close together, only those with very low spike multiplicities can be found far apart. This is explained by the fact that large fluctuations are found preferentially in the central region (cf. fig. VI.11). Fig. VI.18 answers the question, if large spikes are produced with opposing η-values. Along the diagonal $\eta_S = -\eta_{nex}$ no enhancement of events is seen, the spikes uniformly populate the central region. This confirms the assumption that large fluctuations are caused rather by random effects, than any physical mechanism.

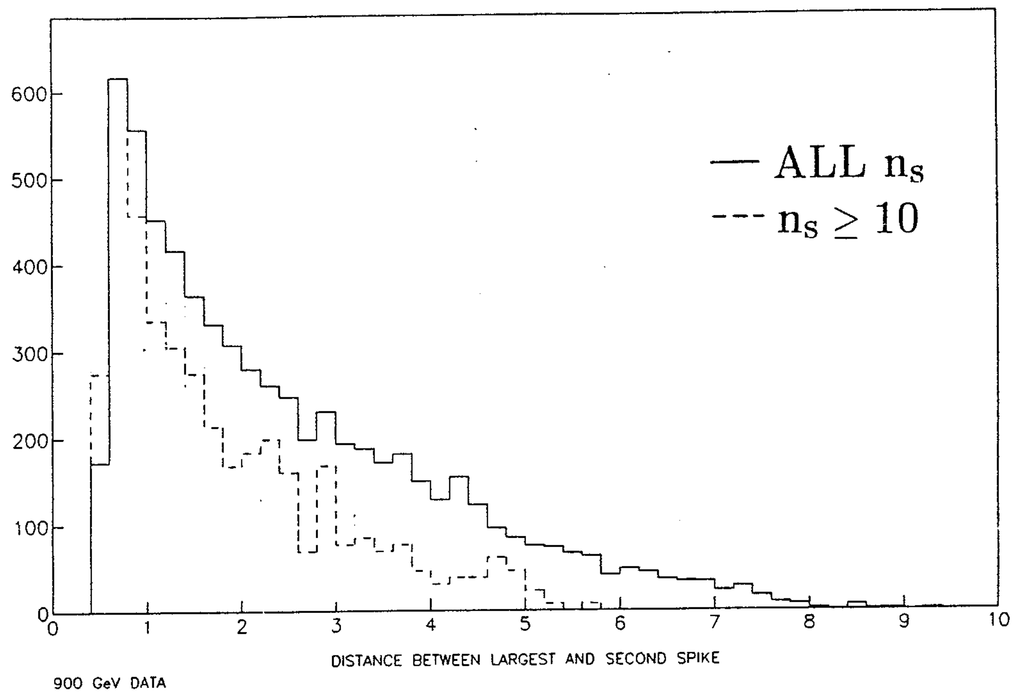

Figure VI.17: Distance between the largest and the second largest spike for different intervals of spike multiplicity. The histograms are normalized to the same height.

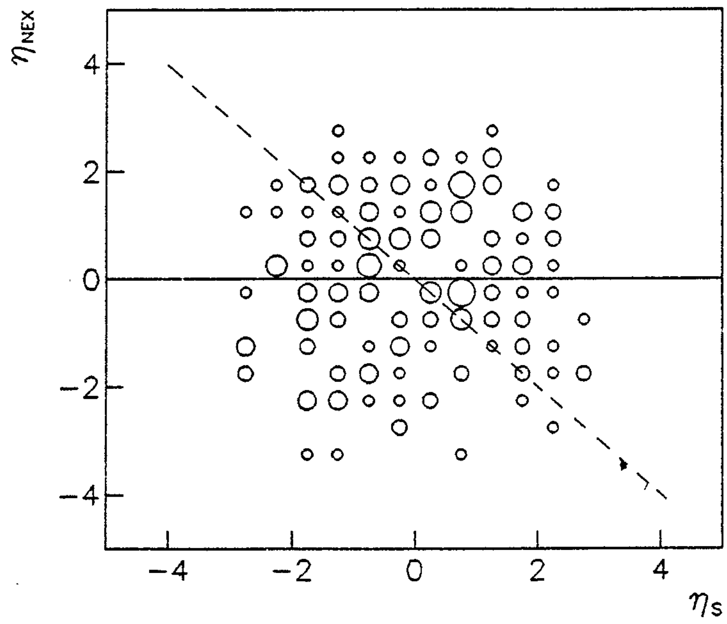

Figure VI.18: The location of the second largest spike plotted against the location of the largest spike for events with $n_s + n_{nex} > 20$. The diagonal with $\eta_S = -\eta_{nex}$ is indicated.

Chapter VII

Conclusion

The data from two successive UA5 runs at $\sqrt{s}$ =200 GeV, 546 GeV, and 900 GeV were analyzed in terms of pseudorapidity densities and compared to simulated data obtained with the UA5-Monte Carlo program, which incorporates a cluster model. The analysis falls into two parts, one on correlation functions, the other on local fluctuations in pseudorapidity density.

The determination of the two-body pseudorapidity correlation function has given the following results :

- The second Mueller moment of the multiplicity distribution, which is the integral of the inclusive correlation function, shows a significant increase from ISR to Collider energies, implying a corresponding increase in particle correlations.
- The inclusive correlation function itself has a similar shape to that observed at lower energies, but the height has increased enormously. The bulk of this energy dependence is due to the "long-range" term contained in the inclusive correlation function. The "short-range" part shows only a slight increase with c.m. energy. The (semi-inclusive) correlation functions at fixed multiplicity are similar in shape to the "short-range" part of the inclusive correlation function. Both the energy and multiplicity dependence of the semi-inclusive correlation functions disappear when appropriately normalized, i.e. by the overall multiplicity for those samples.
- Inclusive and semi-inclusive correlation functions have been successfully interpreted in terms of cluster models. A fit to the cluster model predictions yielded for the charged cluster decay multiplicity moment $\frac{\langle\kappa(\kappa-1)\rangle}{\langle\kappa\rangle}$ values around 1.45, fairly independent in the range of Collider energies. These values are slightly higher than those obtained in ISR experiments. The cluster decay width turned out to be consistent with expectations from an isotropic cluster decay and with measurements of this quantity at lower energies.
- Assumptions on the shape of the cluster decay distribution gave predictions of the multiplicity dependence of $\frac{\langle\kappa(\kappa-1)\rangle}{\langle\kappa\rangle}$. It was found that a Poisson distribution reproduces the data very well, with an average charged decay multiplicity of about 1.5 independent of c.m. energy. This gives for the charged cluster decay multiplicity, including clusters with no charged particles, a value of $\langle\kappa\rangle_0 \simeq 1.9$ in good agreement with other experiments.
- An interpretation of clusters as physical objects, such as resonances, cannot reproduce values of $\langle\kappa\rangle$ as high, as those measured. Therefore, clusters must be thought of as a

concept, comprising various hadronic effects, such as resonance decay, local quantum number conservation, or short fluctuating chains.

- The UA5-Monte Carlo program, which incorporates a cluster model, was seen to reproduce the data very well.

Summarizing, one can say that short-range correlations have not changed significantly from lower energies; and the concepts introduced to explain the properties of those correlations still provide a valid interpretation of the data at Collider energies.

Concerning fluctuations in pseudorapidity density the following properties have been observed :

- Several events have been found in the data, that show a very high particle density in a small region of pseudorapidity, but with a uniform azimuthal distribution, unlike jets.

- The average multiplicity in the spike increases with energy and with the size of the window. The spike multiplicity distribution shows a similar behavior as the charged multiplicity distribution. It falls off exponentially at high values and broadens if the energy is increased. The normalized spike multiplicity distribution shows very little change with energy. The multiplicity in the spike was found to be correlated with the overall charged multiplicity of an event. There are indications that, for high enough multiplicities, it rises linearly with the overall multiplicity and that the slope decreases with increasing energy.

- All events with a high density fluctuation are consistent with a random distribution in azimuth. The spikes are preferentially located in regions, where the average particle density is high anyway. The deviation of the spike density from the average pseudorapidity density was seen to be of a statistical nature only.

- It turns out, that the fluctuations are not extremely sensitive to clustering effects; the spike phenomena itself may be reproduced without introducing short-range correlations in terms of clusters, but for a quantitative correspondence they are necessary to reproduce the data adequately. No abnormal correlation is evident between the spike and other parts of the event (e.g. the second largest fluctuation); spikes appear in regions of high density independently of each other. All properties of density fluctuations could be well reproduced by the UA5-Monte Carlo program.

Consequently, one would summarize that high density fluctuations are produced by a random superposition of clusters, i.e. a concept found to be useful for the description of correlations, but need no other more exotic phenomenon for their explanation.

In final conclusion it turns out that two independent features of pseudorapidity distributions, namely correlations amongst the final state particles and density fluctuations, both, are in accordance with the same working concept, that of cluster production — to be contrasted to independent single particle emission.

References

[ADA 86] M.Adamus, et al., CERN/EP 86-218 (1986).

[ALE 62] K.I. Aleksejeva et al., J. Phys. Soc. Japan **17** (1962) 409.
N. Arata et al., Nuovo Cimento a **43** (1978) 455.
N.A. Marutyan et al., Sov. J. Nucl. Phys. **29** (1979) 804.
G.V. Apanasenko et al., JETP Lett. **30** (1979) 145.

[AME 74] S.R. Amendolia et al., Phys. Lett **48B** (1974) 359.

[AME 76] S.R. Amendolia et al., Nuovo Cimento **31A** (1976) 19.

[AND 84] P. Anderer, Diploma-Thesis, Bonn, BONN-IR-84-31 (1984).

[ARN 82] G. Arnison et al., Phys. Lett. **118B** (1982) 167.

[ASM 81] B. Åsman et al., Nucl. Instr. Meth. **187** (1981) 371.

[ASM 85] B. Åsman ,Thesis, Stockholm, USIP Report 85-17 (1985).

[BAI 87] J.L. Bailly et al., CERN/EP 87-113 (1987).

[BEL 72] G. Belletini, XVI. Int. Conf. on High Energy Physics, Chicago-Batavia (1972) 279.

[BEL 84] W. Bell et al., Z. Phys. **B86** (1975) 109.

[BEN 78] J. Benecke and J. Kühn, Nucl. Phys. **B140** (1978) 179.

[BER 75a] E.L. Berger, Phys. Lett. **43B** (1973) 132.

[BER 73b] E.L. Berger, Int. School of Subnuclear Physics, Erice, 1973 (1975) 557.

[BER 75] E.L. Berger, Nucl. Phys. **B85** (1975) 61.

[BIA 73] A. Białas, 4th International Symposium on Multiparticle Hadrodynamics, Pavia, 1973, p. 93.

[BIA 86] A. Białas and R. Peschanski, Nucl. Phys. **B273** (1986) 703.

[BRE 82] A. Breakstone et al., Phys. Lett. **114B** (1982) 383.

[BUR 83] T.H. Burnett et al., Phys. Rev. Lett. **50** (1983) 2062.

[BUR 82] L. Burow, Diploma-Thesis, Bonn, BONN-IR-82-4 (1982).

[BUR 87] L. Burow, Thesis, Bonn, BONN-IR-87-25 (1987).

[CAP 85] A. Capella and J. Tran Thanh Van, 5th Topical Workshop on Proton-Antiproton Collider Physics, St. Vincent, Italy (1985), p. 523.

[CAV 83] V. Cavasinni et al., Z. Phys. C21 (1984) 299.

[CHI 82] J. Chinellato et al., paper to the Paris Conference, July 1982 (1982).

[CLI 68] J.M. Cline et al., CALT-68-1388 (1968).

[COH 73] D. Cohen, 4th Symp. on Mult. Dynamics, Pavia, 1973 (1974) 172.

[COR] comprises : [AME 74],[SIN 74],[EGG 75b],[AME 76],[UHL 77],
[KAF 77],[DRI 79],[BRE 82],[CAV 83],[BEL 84],
[BAI 87],[GIA 79],[WHI 76],[FOA 75].

[DER 86] M. Derrick, 17th Symp. on Multiparticle Dynamics, Seewinkel (1986) 197.

[DRE 81] I.M. Dremin, Sov. J. Nucl. Phys. **33(5)** (1981) 726.

[DRE 87] I.M. Dremin, CERN-TH.4693 (1987).

[DIA 87a] J. Dias de Deus and A. Noronha da Costa, Phys. Lett. **A120** (1987) 19.

[DIA 87b] J. Dias de Deus, Phys. Lett. **B194** (1987) 297.

[DIB 73] H. Dibon et al., Phys. Lett. **44B** (1973) 313.

[DRI 79] D. Drijard et al., Nucl. Phys. **B155** (1979) 269.

[EAD 71] W.T. Eadie, D. Dryard, F.E. James, M. Roos, B. Sadoulet, "Statistical Methods in Experimental Physics", North Holland Publishing Company, Amsterdam and London (1971).

[EGG 75a] K. Eggert et al., Nucl. Instr. Meth. **126** (1975) 477.

[EGG 75b] K. Eggert et al., Nucl. Phys. **B86** (1975) 201.

[FIS 83] M. Fischer, Diploma-Thesis, Bonn, BONN-IR-83-26.

[FOA 75] L. Foa, Phys. Rep. **22** (1975) 1.

[FRO 85] L. Fröbel, Diploma-Thesis, Bonn, BONN-IR-85-23 (1985).

[GAU 84] J. Gaudaen, Thesis, Antwerpen (1984).

[GEI 85] Ch. Geich-Gimbel, Proceedings of "The Quark Structure of Matter", Strasbourg-Karlsruhe 1985, 465 (1986).

[GEI 87] W. Geist, Lecture on "Heavy Ion Collisions at High Energy", CERN (1987).

[GIA 79] G. Giacomelli and M. Jacob, Phys. Rep. **55** (1979) 1.

[GYU 83] M. Gyulassy et al., LBL-16277 (1983).

[HAG 84] R. Hagedorn, CERN-TH.3889 (1984).

[HAY 73] F. Hayot and A. Morel, Nucl. Phys. **B59** (1973) 493.

[HOF 77] W. Hofmann, Thesis, Karlsruhe, Report Kfk 2489 (1977).

[HOF 81] H. Hoffmann, Proc. Int. Symp. Lepton and Photon Interactions at High Energies, Bonn (1981).

[HOL 86] B. Holl, Diploma-Thesis, Bonn, BONN-IR-86-15 (1986).

[HOL 87] B. Holl, private communication (1987)

[HOS 82] R. Hospes, Diploma-Thesis, Bonn, BONN-IR-82-3 (1982).

[HOS 86] R. Hospes, Thesis, Bonn, BONN-IR-11 (1986).

[JAC 82] M.Jacob and J. Tran Thanh Van, editors, Phys. Rep. 88C (1982) 321.

[JAD 72] S. Jadach, Comp. Phys. **9** (1972) 297.

[KAF 77] T. Kafka et al., Phys. Rev. **D16** (1977) 126.

[KEN 73] M.G. Kendall and A. Stuart, "The Advanced Theory of Statistics", Charles Griffin and Co. Ltd., London (1973), Vol.1, 235.

[KO 72] W. Ko, Phys. Rev. Lett. (1972) 935.

[KOC 82] W. Koch, 13th Symp. on Multiparticle Dynamics, Volendam (1982) 535.

[KNO 74] W.J. Knox, Phys. Rev. **D10** (1974) 65.

[KOZ 79] H. Koziol, PS/AA/Note 79-2 (1979).

[KRZ 73] A. Krzywicki, Nucl. Phys. **B58** (1973) 633.

[LAT 80] C.M.G. Lattes et al., Phys. Rep. **C65** (1980) 151.

[LAU 85] R. Laukner, paper to Vancouver Accelerator Conference, June 1985 (1985).

[LEB 76] M. Le Bellac, CERN 76-14 (1976)

[MAG 82a] M.N. Maggs, CERN/EP/SCE-R703T-UA5/S 82-4 (1982).

[MAG 82b] M.N. Maggs, CERN/EP/SCE-R703T-UA5/P 82-12 (1982).

[MEE 72] S. van der Meer, CERN/ISR-PO 72-31 (1972).

[MEI 78] W. Meincke, Thesis, Bonn, BONN-IR-78-14 (1978).

[MEI 81] R. Meinke, Proc. 2nd Topical Conf. on Forward Collider Physics 1981, Madison.

[MOD] comprises : [BER 75],[BIA 73],[BEN 78],[RAN 73],[HAY 73]

[MOE 80] D. Möhl et al., Phys. Rep. **58,2** (1980) 73.

[MUE 71] A.H. Mueller, Phys. Rev. **D4** (1971) 150.

[MUE 83] Th. Müller, Thesis, Bonn, BONN-IR-83-21 (1983).

[OVE 86] J.E.V. Ovens, Thesis, Cambridge, RAL-T-026 (1986).

[PEL 85] W. Pelzer, Diploma-Thesis, Bonn, BONN-IR-39 (1985).

[PIR 73] P. Pirilä and S. Pokorski, Phys. Lett. **43B** (1973) 302.

[RAN 73] G. Ranft and J. Ranft, Nucl. Phys. **B53** (1973) 217.

[RUB 76] C. Rubbia et al., Proc. Int. Neutrino Conf., Aachen (1976).

[RUB 84] C. Rubbia, Nobel Lecture 1984, The Nobel Foundation (1985).

[RIC 74] P. Rice-Evans, "Spark, Streamer, Proportional and Drift Chambers", London, Richelieu Press (1974).

[RUS 79] J.G. Rushbrooke and S. Tavernier, CERN/EP/SCE-R703T-UA5/T 79-13.

[RUS 80] J.G. Rushbrooke, CERN/EP/SCE-R703T-UA5/M 80-10 (1980).

[RUS 82] J.G. Rushbrooke, CERN-EP/82-6 (1982). (1979).

[RUS 84] J.G. Rushbrooke, CERN/EP 84-34 (1984).

[RUS 85] J.G. Rushbrooke, CERN/EP/85-124 (1985) and proceedings of the XVI. Symp. Mult. Dynamics, Kiryat Anavim, June 1985 (1985) 289.

[SCH 86] H. Schmickler, Thesis, Bonn, BONN-IR-86-34 (1986).

[SIN 74] R. Singer et al., Phys. Lett. **49B** (1974) 481.

[THO 77] W. Thomé et al., Nucl. Phys. **B120** (1977) 365.

[UA1 78] UA1 Collaboration, CERN/SPSC/78-6,141,158 (1978).

[UA2 78] UA2 Collaboration, CERN/SPSC/78-8,54,126,133,162 (1978).

[UA4 78] UA4 Collaboration, CERN/SPSC/78-11,105 (1978).

[UA4 84] M. Bozzo et al., Phys. Lett. **147B** (1984) 385, and 392.

[UA4 87] D. Bernard et al., Phys. Lett. **186B** (1987) 227.

[UA5 78] UA5 Collaboration, CERN/SPSC/78-70,107,147 (1978).

[UA5 80] UA5 Collaboration, CERN/EP/SCE-R703T-UA5/P80-20 (1980).

[UA5 81a] UA5 Collaboration, Physica Scripta **23** (1981) 642.

[UA5 81b] K. Ålpgard et al., Phys. Lett. **107B** (1981) 310.

[UA5 81c] K. Ålpgard et al., Phys. Lett. **107B** (1981) 315.

[UA5 82a] UA5 Collaboration, CERN/SPSC/82-75/P184.

[UA582b] K. Ålpgard et al., Phys. Lett. **112B** (1982) 183.

[UA5 82c] K. Ålpgard et al., Phys. Lett. **115B** (1982) 65.

[UA5 82d] K. Ålpgard et al., Phys. Lett. **115B** (1982) 71.

[UA5 83a] K. Ålpgard et al., Phys. Lett. **121B** (1983) 209.

[UA5 83b] K. Ålpgard et al., Phys. Lett. **123B** (1983) 361.

[UA5 84] G.J. Alner et al., Phys. Lett. **138B** (1984) 304.

[UA5 85a] G.J. Alner et al., Phys. Lett. **151B** (1985) 309.

[UA5 85b] G.J. Alner et al., Nucl. Phys. **B258** (1985) 505.

[UA5 85c] G.J. Alner et al., Phys. Lett. **160B** (1985) 193.

[UA5 85d] G.J. Alner et al., Phys. Lett. **160B** (1985) 199.

[UA5 86a] G.J. Alner et al., Phys. Lett. **167B** (1986) 476.

[UA5 86b] G.J. Alner et al., Z. Phys. **C32** (1986) 153.

[UA5 86c] G.J. Alner et al., Phys. Lett. **180B** (1986) 415.

[UA5 86d] G.J. Alner et al., Z. Phys. **C33** (1986) 1.

[UA5 86e] R.E. Ansorge et al., Z. Phys. **C33** (1986) 175.

[UA5 87a] G.J. Alner et al., Nucl. Phys. **B291** (1987) 445.

[UA5 87b] G.J. Alner et al., Z. Phys. **C37** (1987) 191.

[UA5 87c] G.J. Alner et al., Phys. Rep. **154** (1987) 247.

[UA5 87d] R.E. Ansorge et al., Phys. Lett. **199B** (1987) 311.

[UA5 88a] UA5-Collaboration,"Hyperon Production at 200 and 900 GeV c.m. Energy", in preparation.

[UA5 88b] UA5-Collaboration,"Photon Production at 200 and 900 GeV c.m. Energy",in preparation.

[UHL 78] S. Uhlig et al., Nucl. Phys. **B132** (1978) 15.

[VER 84] W. Vernon Jones, Nucl. Phys. **A418** (1984) 139c.

[WAR 83a] D.R. Ward, CERN/EP/SCE-R703T-UA5/P83-1.

[WAR 83b] D.R. Ward, Proc. 3rd Topical Workshop on $p\bar{p}$ Collider Physics 1983, Rome.

[WAR 80] D.R. Ward, CERN/EP/SCE-R703T-UA5/S80-21.

[WAR 84] D.R. Ward, private communication (1984).

[WAR 85a] D.R. Ward, Proceedings of the 5th Int. Conf. on Physics in Collision, Autun, July 1985 (1986) 67.

[WEI 82] A.R. Weidberg, Thesis, Cambridge, HEP T 102 (1982).

[WHI 76] J. Whitmore, Phys. Rep. **10** (1974) 273. and Phys. Rep. **27** (1976) 187.

[WIL 63] K. Wilson, Acta. Phys. Austriaca 17 (1963) 37.

[WIL 70] K.G. Wilson, CLNS-131, Cornell University (1970).

List of Figures

List of Tables

Danksagung

Diese Arbeit entstand unter der Anleitung von Herrn Prof. Dr. K. Böckmann, dem ich über seinen Tod am 17. Oktober 1985 hinaus zu tiefer Dankbarkeit verpflichtet bin. Ohne sein fortwährendes kritisches Interesse und seine vielen motivierenden Gespräche wäre ein Zustandekommen dieser Arbeit nicht möglich gewesen.

Den Herren Prof. Dr. G. Knop und Dr. C. Geich-Gimbel, die nach dem Tode von Herrn Prof. Dr. K. Böckmann die fachliche Betreuung übernahmen, möchte ich herzlich danken für ihre wissenschaftlichen Anregungen und ihr Engagement, um die Fertigstellung dieser Arbeit zu ermöglichen.

Allen Mitgliedern der UA5-Kollaboration gilt mein Dank für die kooperative Zusammenarbeit und die gute Arbeitsatmosphäre, die viele fruchtbare Diskussionen stimulierte. Besonders hervorheben möchte ich die Zusammenarbeit mit Herrn Dipl. Phys. B. Holl, die zu vielen anregenden Gesprächen führte.

Allen Angestellten des Physikalischen Instituts und der an der UA5-Kollaboration beteiligten Institute danke ich für ihre Beiträge zur Durchführung und Auswertung des Experimentes, sowie zur Fertigstellung dieser Arbeit.

Mein besonderer Dank gilt meiner Familie, die mir während der Promotionszeit mit großer Geduld und ständiger Ermutigung beigestanden hat.